Proximity labelling reveals the compartmental proteome of murine sensory neurons

Julia R Sondermann[1]*, Allison M Barry[1]*, Feng Xian[1], Thomas Haberl[1], David Gomez-Varela[1], Fritz Benseler[2], Dietmar Schreiner[3], Nils Brose[2], Noa Lipstein[2,4], Manuela Schmidt[1λ]

1. Systems Biology of Pain, Division of Pharmacology & Toxicology, Department of Pharmaceutical Sciences, University of Vienna, Austria
2. Department of Molecular Neurobiology, Max Planck Institute for Multidisciplinary Sciences, 37075 Göttingen, Germany
3. Biozentrum, University of Basel, Basel, Switzerland
4. Leibniz-Forschungsinstitut für Molekulare Pharmakologie (FMP), 13125 Berlin, Germany

** these authors contributed equally*

[λ] corresponding author: Manuela Schmidt; manuela_schmidt@univie.ac.at

Keywords

sensory neuron; proximity labelling; TurboID; DIA-MS; CIPN; DRG; bulk proteomics

Abstract

Introduction. Understanding the molecular architecture of peripheral sensory neurons is critical as we pursue novel drug targets against pain and neuropathy. Sensory neurons in the dorsal root ganglion (DRG) show extensive compartmentalization, thus understanding each compartment – from the peripheral to central terminals – is key to this effort.

Methods. To systematically profile this spatial complexity, we generated a TurboID$^{fl/fl}$ transgenic mouse line (ROSA26$^{em1(TurboID)Bros}$), enabling targeted proximity labelling and deep proteomic profiling of DRG neuron compartments via Tg(Advillin-Cre)$^{+}$.

Results. Our data reveal distinct proteomic signatures across neuronal compartments that reflect specialized neuronal functions. We provide proteomic insights into previously inaccessible nerve terminals both in the periphery (innervating the skin) and in the spinal cord. Further, using a DRG explant model of chemotherapy-induced peripheral neuropathy, we uncover novel and discrete proteome changes, highlighting neuronal vulnerability.

Conclusion. Together, our findings provide a unique proteome atlas of the sensory neuron proteome across anatomical domains and demonstrate the utility of proximity labelling proteomics for detecting compartment-specific molecular alterations in a disease model.

Introduction

Dorsal root ganglia (DRG) serve as critical hubs in the peripheral nervous system (PNS), housing the somata of sensory neurons that transmit information from the periphery (Middleton et al., 2021). DRG comprise sensory neurons as well as other cells, including glial and immune cells. Consequently, the interpretation of bulk proteomics data from DRG is inherently complex.

Adding to this complexity, DRG neurons exhibit spatial compartmentalization via axons to peripheral and central nerve terminals. Understanding their spatial proteome is therefore critical for elucidating the molecular mechanisms underlying sensory processing, neuronal maintenance, and pathological conditions such as chronic pain. However, obtaining a comprehensive and spatially-resolved molecular profile of DRG neurons remains a significant technical challenge. Methods like fluorescence-activated cell sorting (FACS) can isolate specific cell types and have been used for synaptosome isolation (Biesemann et al., 2014), but FACS predominately prioritizes somata and/or nuclei. Isolating intact spatial compartments, particularly the nerve terminals, remains a major hurdle.

In recent years, proximity-dependent proteomic techniques like TurboID and APEX, have emerged as powerful tools for mapping subcellular proteomes and interactomes (Gingras et al., 2019; Qin et al., 2021). TurboID is an engineered, promiscuous biotin ligase that enables rapid and efficient labelling of proteins within a close proximity in living cells (Branon et al., 2018). To date, most applications of TurboID and its predecessor BioID have involved fusion proteins with compartment-specific targeting sequences, enabling selective biotinylation of proximal interactomes for downstream affinity purification and identification via mass spectrometry (MS) (Dingar et al., 2015; May et al., 2020; Roux et al., 2012). Unlike TurboID fusion proteins, the use of soluble TurboID variants enables unbiased labelling of the entire accessible proteome within a cell. Sunna et al. demonstrated that TurboID-mediated biotinylation covers approximately 59–65% of the proteome across cell lines expressing a cytosolic TurboID variant (Sunna et al., 2023). Proximity labelling has also been successfully used to probe central nervous system compartments. For example, Rayaprolu et al. developed a mouse model to explore brain region-specific proteomic differences using TurboID *in vivo* (Rayaprolu et al., 2022). In another study, Hobson et al. employed APEX2 proximity labelling to map proteomic differences between somatodendritic and axonal compartments in acute brain slices, demonstrating correlates with respective neuronal function (Hobson et al., 2022).

Here, we generated a conditional mouse line expressing TurboID from the Rosa26 locus, enabling cell-type-specific proximity labelling *in vivo* using a Cre-lox system. Paired to a Tg(Advillin-Cre)$^{+}$ driver line (Zurborg et al., 2011), TurboID expression is prominent in DRG sensory neurons. Consequently, we were able to systematically pro-

file the proteomes of DRG neuron compartments, providing a spatially resolved proteomic atlas. We then harnessed this technique to explore proteome changes after oxaliplatin treatment in an *in vitro* DRG explant model of chemotherapy-induced peripheral neuropathy (CIPN). CIPN is a common side effect of chemotherapy, with agents damaging sensory neurons and leading to painful neuropathy often preventing adequate cancer therapy (Sisignano et al., 2014). Indeed, we observed aberrant neuronal proteome dysregulation after oxaliplatin treatment, including changes not detected with bulk proteomics.

Together, our findings reveal novel insights into the compartment-specific protein distributions underlying key aspects of sensory neuron function and disease-related alterations.

Methodology

Generation of TurboID mice (ROSA26$^{em1(TurboID)Bros}$) using CRISPR/Cas9

The conditional TurboID knock-in (cKI) mouse line was generated by site-directed CRISPR/Cas9 mutagenesis in the ROSA26 locus. Superovulated C57Bl6/J females were mated with C57Bl6/J males and fertilized eggs collected. In-house produced CRISPR reagents (hCas9_mRNA, sgRNAs, preformed Cas9_sgRNA-RNP complexes and the homology-directed repair fragment (HDR fragment)) were microinjected into the pronucleus and the cytoplasm of pronuclear-stage zygotes using an Eppendorf Femtojet (Eppendorf SE, Germany). Importantly, all nucleotide-based CRISPR/Cas9 reagents (sgRNAs and hCAS9_mRNA) were used as RNA molecules and were not plasmid-encoded, reducing the probability of off-target effects due to the short lifetime of RNA-based reagents (Doench et al., 2016; Tycko et al., 2019). The TurboID-containing HDR fragment was generated by subcloning a V5-tag-TurboID sequence into the Ai14-ROSA26-based plasmid backbone (Madisen et al., 2010) and isolated as a linear DNA fragment by SacI/AgeI restriction enzyme double digestion. Two sgRNAs targeting the ROSA26 Locus were selected using the guide RNA selection tool CRISPOR (Concordet & Haeussler, 2018; Haeussler et al., 2016). The correct locus-specific insertion of the HDR fragment was confirmed by localization PCRs with primers upstream and downstream of the HDR sequence. Extended details, including full sequences and genotyping strategy, are available in the Supplemental Methods.

Animal husbandry, breeding, and biotin supplementation

Adult male and female TurboID$^{fl/fl}$ control and Adv^{Cre};TurboID$^{fl/fl}$ mice (12.5-26 weeks old for compartmental proteome, 57-71 weeks old for oxaliplatin part) and in-house bred wild type C57Bl6/J male mice (60-66 weeks old) were kept in a 12/12h day/night cycle with *ad libitum* access to food and water in an open-cage environment. The animal experiments were conducted in accordance with ethical guidelines and were approved by the Institutional Animal Care and Use Committee (IACUC) at the University of Vienna

and the Austrian Ministry for Education, Science, and Research (BMBWF; license number 2021-0.138.925 amended by 2024-0.896.105). All procedures complied with the international ARRIVE guidelines and adhered to the European Union Directive 2010/63/EU on the protection of animals used for scientific purposes. No mice were removed from the study before their expected endpoint.

Breeding strategy: Male mice of the Tg(Advillin-Cre) driver line (referred to here as Adv^{Cre}) (Barry et al., 2023; Lopes et al., 2017; Zheng et al., 2019; Zurborg et al., 2011) were crossed with here generated $ROSA26^{em1(TurboID)Bros}$ ($TurboID^{fl/fl}$) females to ultimately obtain mice heterozygous for Adv^{Cre} ($Adv^{Cre/+}$) and homozygous for TurboID (referred to here as Adv^{Cre};$TurboID^{fl/fl}$), along with their littermate controls ($TurboID^{fl/fl}$). Full details are provided in the Supplemental Methods.

Biotin supplementation: $TurboID^{fl/fl}$ control and Adv^{Cre};$TurboID^{fl/fl}$ mice received biotin-enriched drinking water (0.22 mg/mL, prepared fresh every day) for 7 consecutive days to enhance biotinylation (Branon et al., 2018). On day 8, the mice were sacrificed. This dosing mirrored dosing of BioID mice, and can likely be reduced for TurboID, as reported for the C57Bl6/J -*Gt(ROSA)26Sor*$^{tm1(birA)Srgj}$/J line (Rayaprolu et al., 2022).

Mouse numbers: The compartmental proteome was generated from pooled samples (3-6 animals per sample) from the following mice: $TurboID^{fl/fl}$ control = 29M + 29F and Adv^{Cre};$TurboID^{fl/fl}$ = 19M + 27F. Sample pools were stratified by sex.

Unilateral mouse DRG were used for explant cultures stimulated with Oxaliplatin, the DRG of the other side for the Vehicle condition in parallel. For the enrichment of biotinylated proteins in Adv^{Cre};$TurboID^{fl/fl}$, 4 samples (3M, 1F) were prepared for each condition, with multiple mice pooled for each samples. In total, 10 males and 4 females were used per condition (3-4 mice per sample).

Tissue dissection

Mice were sacrificed via CO_2-inhalation and rapidly decapitated. The vertebral spine was removed for subsequent isolation of the dorsal part of the lumbar 3-5 spinal cord (SC) and lumbar 3-5 dorsal root ganglia (DRG). In parallel the sciatic nerves (SCN) of both sides were dissected. The plantar paw skin (dermis and epidermis, without muscle tissue) was removed by a 4 mm skin punch. Skin samples were immediately snap-frozen in liquid N_2. All other tissues were washed in ice-cold 1× PBS to remove blood residuals before snap-freezing in liquid N_2. All tissues remained at -80°C until further use.

Protein extraction

All steps are done at room temperature (RT) except otherwise mentioned.

DRG: Tissue homogenisation was done in lysis buffer (LB; 2% SDS, 0.1 M tris, 5% glycerol, 0.01M DTT, 1× complete protease inhibitor cocktail) with 3x 10 strokes of a pestle/potter. To facilitate lysis the homogenate was sonicated using a Bioruptor Pico (10x 30 s ON/30 s OFF, 4°C, low frequency). All sonification steps mentioned below are done

155 with the same settings (only cycle number varies). Samples were further incubated at
156 70°C, for 15' min with 1500 rpm (Thermomixer C, Eppendorf). The remaining cell debris
157 was pelleted by centrifugation (10', 10000 ×g) and the supernatant was saved. All repli-
158 cates of one condition were pooled and the concentration determined at 280 nm with a
159 NanoPhotometer N60 (Implen, München, Deutschland).

160 SCN: Protocol was performed as above, except the centrifugation was followed by an-
161 other 5 min-long centrifugation (RT, 10000×g) to further clear the lysate of lipid clouds.
162 Before pooling and concentration measurement an acetone precipitation was done (see
163 below).

164 SC: The DRG protocol was modified in that the pestle/potter step was omitted, instead
165 the SC was cut into 3 smaller pieces and transferred to 2 mL LoBind tubes (prefilled with
166 500 µL of LB) for sonification Pico for 15 cycles. Other steps as for DRG, but before pool-
167 ing and concentration measurement an acetone precipitation was done (see below).

168 Paw skin: the skin punches were cut into 4 smaller pieces, transferred into a potter pre-
169 filled with LB and homogenized with help of 3× 10 strokes of a pestle/potter. Lysis of tis-
170 sue was facilitated by incubation for 20 min, at 70°C and 1500 rpm, followed by sonifi-
171 cation for 15 cycles. The lysate was cleared of cell debris and excessive lipids by 2× cen-
172 trifugation 10 min, 10000×g) and the supernatant was saved. Before pooling and con-
173 centration measurement an acetone precipitation was done (see below).

174 For the SCN, SC and paw skin an acetone precipitation was done to reduce the amount
175 of lipids in the samples: 5× sample volume of pre-cooled (-20°C) 100% acetone was
176 added to each sample and the tube was shortly inverted to ensure thorough mixing. If
177 needed, samples were split into 2× 2 mL tubes to allow for 5× addition of sample vol-
178 ume. Precipitation of proteins was allowed for 3-3.5 h at -20°C. Next the precipitates
179 were pelleted by centrifugation for 30 min and 14000×g. Pellets were washed with 1.5
180 mL pre-chilled (4°C) 80% ethanol and the centrifugation repeated as above. After re-
181 moval of the ethanol, pellets were air-dried for 20-30 min. Proteins were reconstituted in
182 LB by incubation for 15 min, 70°C, 1500 rpm. If were not fully solubilized, the incubation
183 was repeated and LB volume increased until fully solubilized. Total protein concentra-
184 tion of pooled samples was determined with a NanoPhotometer at 280 nm.

185 *Streptavidin-mediated enrichment of biotinylated proteins*

186 Streptavidin-affinity purification protocol is based on the high stringency protocol de-
187 scribed in Go et al., 2021 with modifications. The required amount of streptavidin beads
188 (Sera-Mag SpeedBead Blocked Streptavidin Particles, Cytiva, 83 µL bead slurry/ 1000 µg
189 input) was transferred into LoBind protein tubes, washed twice with 500 µL LB without
190 SDS, and resuspended in the same buffer. Protein lysates (input amount: DRG 1000 µg,
191 SCN 600 µg, SC 800 µg, skin 2000 µg) were prepared to a final SDS concentration of
192 0.5%, final volume of 1500 µL. Lysates were incubated with the beads at 4°C for 3.5 h on

193 an overhead shaker. Unless otherwise stated, all subsequent steps were performed at
194 RT.

195 Following incubation, samples were placed on a magnetic rack for 2 min. Beads were
196 then subjected to a series of washes, each performed with 1 mL of buffer, followed by
197 overhead shaking for 1 min each (Grant-Bio PTR-35 Multi-Rotator) and incubation on the
198 magnetic rack for 2 min until the solution cleared. The washes included one step with
199 2% SDS Wash Buffer (2% SDS, 25 mM Tris), two washes (three for skin samples) with
200 modified RIPA buffer (50 mM Tris, 150 mM NaCl, 1.5 mM $MgCl_2$, 1% Triton X-100, 1 mM
201 EDTA), and three washes with 50 mM ammonium bicarbonate (ABC, pH 8). After the first
202 ABC wash, the beads were transferred to a new 1.5 mL LoBind tube in 500 µL ABC
203 buffer, followed by the addition of another 500 µL ABC before finalizing the washes.

204 For protein reduction, 135 µL of 5 mM dithiothreitol (DTT) in 50 mM ABC containing 0.8
205 mM biotin was added to each sample and incubated at 60°C for 30 min at 1000 rpm.
206 Samples were then cooled to RT by briefly placing them on ice. Alkylation was per-
207 formed by adding iodoacetamide (IAA) to a final concentration of 20 mM (15 µL of 200
208 mM IAA), followed by incubation for 30 min in the dark under constant agitation. The re-
209 action was quenched by adding 1M DTT to a final concentration of 5 mM and incubating
210 for 15 min with 3× 5 s vortexing steps in between. Proteins were digested for 17 h at 37°C
211 and 950 rpm using 1.5 µg Trypsin/LysC per 1000 µg input. After the digest, peptides were
212 eluted by placing the tubes on a magnetic rack for 2 min and transferring the superna-
213 tant to fresh 2 mL LoBind tubes. The beads were further washed with 20 µL MS-grade
214 water (5 min, 500 rpm), and the wash was pooled with the initial eluate. Peptide concen-
215 trations were measured at 205 nm to calculate the required amount of SP3-beads (1:1
216 mix of Sera-Mag SpeedBead beads, 10-15 µL bead slurry to 40-50 µg peptides). To
217 clean-up the peptides, peptide solution was split into two 2 mL tubes, the required bead
218 amount and 100% ACN was added to reach 95% ACN. Samples were incubated for 8
219 min and 500 rpm, followed by a 2-min incubation on a magnetic rack. The ACN was dis-
220 carded, and beads were rinsed with 400 µL 100% ACN, incubated for 2 min on a mag-
221 netic rack, and the ACN was discarded again. Peptides were reconstituted in 20-25 µL
222 MS-grade water, incubated for 5 min with shaking at 500 rpm, followed by another 2-min
223 incubation on a magnetic rack. The supernatants of previously split samples were
224 pooled, centrifuged at 17000×g for 2 min, placed on a magnetic rack, and the final su-
225 pernatant was transferred to a glass vial. Peptide concentrations were measured at 205
226 nm with a NanoPhotometer, and samples were acidified to a final concentration of 0.1%
227 formic acid (FA). The samples were stored at -20°C until LC-MS measurement.

228 *DRG explants preparation*

229 From both Adv^{Cre};$TurboID^{fl/fl}$ and $TurboID^{fl/fl}$ mice (fed with biotin-enriched water for 7
230 days, see above) 20 DRG per side were isolated and collected separately by side in two
231 tubes containing DMEM/F-12 at RT for explant culturing (Fornaro et al., 2018). The DRG
232 of one side were plated in 50 µL volume in to a well of a 24-well plate and incubated for

233 10 min at 37°C, 5% CO_2. In the meantime, the oxaliplatin (100 µM) and/or vehicle (H_2O,
234 Veh) was mixed with DMEM +10% horse serum (HS) +100 ng/mL nerve growth factor
235 (NGF) + 50 µM biotin and 500 µL/well were carefully added. The drug/Veh was incubated
236 for 48 h at 37°C, 5% CO_2.

237 To find an effective oxaliplatin concentration in line with previous reports (Livni et al.,
238 2019), DRG explant cultures were prepared in a similar way from wild type mice. DRG
239 from one mouse were separated into 4 wells for 4 conditions Veh, 25 µM, 50 µM and 100
240 µM oxaliplatin in DMEM+HS+NGF. The drug/Veh was incubated for 48 h at 37°C, 5%
241 CO_2.

242 *Sample preparation of DRG explants*

243 The protein extraction was done similarly for both WT and TurboID DRG explants. All
244 DRG of one well were transferred to an Eppendorf tube and washed twice with ice-cold
245 1× PBS by inverting the tube 10×. After discarding all PBS, 300 µL LB was added and
246 DRG explants were sonicated for 10 cycles and further incubated at 70°C, for 15 min
247 and 1500 rpm. Remaining cell debris was pelleted by centrifugation (5', 10000×g) and
248 the supernatant was saved. The total protein concentration was determined at 280nm
249 with a NanoPhotometer N60. The TurboID samples underwent the above described
250 streptavidin-affinity purification to enrich for biotinylated proteins and preparation of
251 peptides (input 725 µg).

252 For the WT samples a modified version of the single-pot, solid-phase-enhanced sample
253 preparation (SP3) method(Hughes et al., 2019) was employed to digest proteins and
254 clean the peptides. In brief, 10 µL of pre-mixed Sera-Mag SpeedBead beads were added
255 to 50 µg of protein. To facilitate protein binding to the beads, an equal volume of abso-
256 lute ethanol was added, followed by incubation for 5 min at 24°C and 1000 rpm. Beads
257 were collected on a magnetic rack for 2 min, the supernatant was discarded, and the
258 beads were washed thrice with 500 µL of 80% ethanol. Subsequently, the beads were
259 resuspended in 50 µL of 50 mM ABC, pH 8 containing 2 µg of Trypsin/Lys-C and incu-
260 bated overnight at 37°C and at 950 rpm. Following protein digestion, ACN was added to
261 each sample to reach a final concentration of 95%. After an 8-min incubation, beads
262 were collected on a magnetic rack for 2 min. The supernatant was discarded, and the
263 beads were washed with 900 µL of ACN. For peptide elution, the remaining ACN was al-
264 lowed to evaporate for 2-3 min and the beads were resuspended in 40 µL of LC-MS
265 grade water. Peptide concentrations were measured at 205nm using a NanoPhotometer
266 N60. Finally, the peptide samples were acidified with FA to a concentration of 0.1% and
267 stored at -20°C until LC-MS/MS analysis.

268 *Gel-electrophoresis & Western blot*

269 All lysates from TurboID tissue that were going to be used as input samples for the
270 streptavidin-affinity enrichment were checked by WB for the biotinylation success. The
271 samples were prepared by dissolving them in 4× LDS Sample Buffer supplemented with

272 4× Reducing Agent to reach final 1×concentrations followed by heating to 70°C for 10
273 min. For protein separation, samples were loaded onto pre-cast NuPAGE® Bis-Tris 4–
274 12% gradient gels, the NuPAGE® (Life Technologies) electrophoresis chambers filled
275 with 1× NuPAGE® MOPS buffer and the gels run for 40-50 min at 200 V.

276 Following electrophoresis, proteins were transferred onto PVDF membranes using the
277 iBlot2® Gel Transfer Device (Life Technologies, program #0, 7 min). To block non-spe-
278 cific binding sites, membranes were incubated with 5% milk in PBS for 45 min at RT.
279 Subsequently, membranes were incubated with primary antibodies (diluted in 1%
280 milk/PBS; Stable 1) for 1.5 h, followed by an overnight incubation at 4°C with an addi-
281 tional 1:4 dilution. Membranes were washed with PBS (three short washes followed by
282 three 5-min washes) before incubation with the respective secondary antibodies (di-
283 luted in 1% milk/PBS; see Stable 1) for 1 h. After washing with PBS as described before,
284 immunolabeled proteins were detected using near-infrared fluorescence imaging (Bio-
285 RAD ChemiDoc MP).

286 *LC MS acquisition*

287 Nanoflow reversed-phase liquid chromatography (Nano-RPLC) was performed using
288 NanoElute2 systems (Bruker Daltonik, Bremen, Germany) and coupled to a timsTOF HT
289 mass spectrometer (Bruker Daltonik, Bremen, Germany) via a CaptiveSpray ion source.
290 The mobile phase consisted of solvent A (100% water, 0.1% formic acid) and solvent B
291 (100% acetonitrile, 0.1% formic acid).

292 500 ng peptides were loaded onto a C18 trap column (1 mm × 5 mm, ThermoFisher) be-
293 fore being separated on an Aurora™ ULTIMATE analytical column (25 cm × 75 µm)
294 packed with 1.6 µm C18 particles (IonOpticks, Fitzroy, Australia) over a 60-minute gradi-
295 ent. The flow rate was maintained at 250 nL/min, except for the final 7 minutes, where it
296 was increased to 400 nL/min. The gradient of mobile phase B was adjusted as follows:
297 an initial linear increase from 2% to 15% over 30 minutes, followed by a rise to 35% over
298 22 minutes, and a sharp increase to 85% within 0.5 minutes. The flow rate was then ad-
299 justed to 400 nL/min in 0.5 minutes and held for 7 minutes to ensure complete elution of
300 hydrophobic peptides.

301 Data acquisition was performed in data-independent acquisition (DIA) mode using par-
302 allel accumulation serial fragmentation (PASEF). Precursors with an m/z range of 350–
303 1100 were analysed across 12 MS/MS ramps in a cycle, with either two or three quadru-
304 pole switches per ramp. Each cycle contained 30 MS/MS windows within a 0.65–1.30
305 (1/k0) ion mobility range, using a fixed isolation window of 25 Da per step. The acquisi-
306 tion time per DIA-PASEF ramp was set to 100 ms, resulting in a total cycle time of ap-
307 proximately 1.38 seconds. Collision energy was ramped linearly from 65 eV at 1/k0 = 1.6
308 to 20 eV at 1/k0 = 0.6.

309 *Spectral deconvolution with DIA-NN*

DIA-NN 1.8.2 was used to process DIA-PASEF data in library-free mode (Demichev et al., 2020). For the TurboID and WT samples, each tissue and, in case of Adv^{Cre};TurboID$^{fl/fl}$ and TurboID$^{fl/fl}$ genotypes were processed in a separate analysis step using the same spectral library. The spectral library was predicted from a Mus musculus proteome database from UniProt containing 17,070 protein entries (downloaded on 2021-07-08), in case of the TurboID samples it included in addition streptavidin (P22629|SAV_STRAV) and TurboID sequence. *In silico* digestion was performed using Trypsin/P, allowing up to two missed cleavages. A maximum of three variable modifications was allowed per peptide including methionine oxidation, and N-terminal acetylation, while Cysteine carbamidomethylation was set as a fixed modification. Peptide length for the search ranged from 5 to 52 amino acids. Precursor charge was set to 2-4. In accordance with the DIA-PASEF acquisition method, the m/z ranges were set to 350–1100 for precursor ions and 100–1700 for fragment ions. Mass accuracy was chosen automatically using the first run in the experiment. Protein inference was performed using unique genes. The single-pass mode was chosen. Quantification was carried out using RT-dependent cross-run normalization and the Quant UMS (high precision) option. The main DIA-NN output was processed using the R package DiaNN to extract MaxLFQ intensities (Cox et al., 2014; Demichev et al., 2020) for all identified protein groups, applying a q-value threshold of <0.01 at both the precursor and gene group levels. Matrices were merged by protein group were applicable for downstream analyses.

Neuronal protein enrichments

Protein enrichments were calculated within each tissue/neuronal component prior to merging. First, proteins were filtered for distinct gene symbols, keeping the first instance where matches exist. Any protein detected in ≥75% of Adv^{Cre};TurboID$^{fl/fl}$ samples for a given tissue, and no control sample was considered enriched (type “A”). This comprised the majority of enrichments. For proteins in ≥75% of Adv^{Cre};TurboID$^{fl/fl}$ samples from any tissue, and any amount of control underwent differential expression testing using a standard limma framework (`lmFit` + `eBayes`) (Ritchie et al., 2015). Proteins were modelling by a grouped factor for Tissue and TurboID Status, and contrasted within tissue between TurboID and Control samples (ie. Paw.Turbo – Paw.Control). Proteins were considered enriched when FDR < 0.05, and LFC > 1 (“DEP”).

For explant analyses, we used the cross-tissue enrichments described above as a reference for neuronal enrichment, instead of setting a 75% threshold (ie. explant data were first filtered for neuronal enrichments using this reference list). Any proteins detected in the turbo samples and not control (type “not in TurboID$^{fl/fl}$”), as well as any proteins that then hit a threshold of FDR < 0.05, and LFC > 1 (type “DEP”) were considered enriched in explant neurons.

Pathway analyses

GO enrichments were performed on enriched proteins and differentially expressed proteins using the `enrichGO` function from the ClusterProfiler and org.Mm.eg.db libraries

in R (Wu et al., 2021). Both cellular component (CC) and biological pathways (BP) were extracted, with an adjusted p-value cutoff of 0.01 (Benjamini-Hochberg corrected). To account for redundancy in the GO terms, outputs were slimmed using default settings: `clusterProfiler::simplify(ego, cutoff=0.7, by="p.adjust", select_fun=min, measure = 'Wang')`.

For pathway analyses of TurboID-enriched proteins, a background of all proteins detected across the four tissue wildtype whole cell lysates + proteins detected with TurboID samples – this represents the entire universe of proteins which could have been enriched in neurons using the TurboID approach. For pathway analyses of differentially expressed proteins, a background of all proteins tested within the comparison was used. For pathway analyses of co-expression modules (below), module genes were compared to the universe of neuronal-enriched proteins.

Synaptosome comparisons

Published DIA-MS synaptosome data from the skin/paw (Rawat et al., 2025) and spinal cord (Casañas & Montesinos, 2022) were compared to peripheral and central terminal proteomes respectively. Overlapping proteins were subject to pathway analyses via `ClusterProfiler` as described above, against “CC” (cellular component). Human gene names were mapped to mouse using `biomaRt` in R. Where > 10 pathways were significant, terms were filtered for "synap|signal|signalling|signaling|junction|membrane" for plotting, will all significant hits available in STable 3.

Subtype enrichment

Neuronal subtype enrichment was calculated using an Overrepresentation Analysis (ORA) on previously published custom-made gene lists from the mouse DRG transcriptomics (Barry et al., 2023; Zheng et al., 2019). Briefly, custom gene enrichment lists for DRG neuronal subtypes were calculated from Zheng et al. (2019) using DESeq2 (Love et al., 2014; Zheng et al., 2019). ORA was then performed on TurboID-enriched proteins from each tissue using `Clusterprofiler ::enricher` (Wu et al., 2021). For each tissue, the background was defined as any protein detected in whole cell lysate or TurboID samples, and the custom enrichment lists were filtered for proteins in the pre-defined background prior to ORA. `Clusterprofiler ::enricher` does not allow the definition of both a custom background universe and custom gene set list (instead using only proteins defined in the custom gene sets as a background). To overcome this, the background proteins were defined as an additional gene set, and the gene set size was capped at 2000 to exclude this set from a direct enrichment analysis while maintaining them in the background. An FDR < 0.05 was considered significantly enriched, with an FDR =1 set for plotting.

Immune cell enrichment

The depletion of immune cells was determined by the “infiltration score” from the `ImmuCellAI` package (0.1.0), a GSEA-based approach to query immune signatures (Miao

et al., 2022). Protein names were converted to human gene symbols using the biomaRt package, and the expression of each tissue/compartment was presented against a background of all proteins detected in bulk and/or turbo samples, mirroring the pathway analysis (above). Missing values were imputed as zeros, and ImmuCellAI was run with default settings. The “infiltration score” was extracted from the resulting abundance matrix for plotting via ggplot2.

Sexual dimorphism

Male/Female differences were tested using a standard limma framework for the neuronal proteome of each tissue (Ritchie et al., 2015). Proteins were modelled using a grouped factor for Tissue and Sex and contrasted within Tissue as M – F. Proteins were considered enriched when FDR < 0.05, and abs(LFC > 1). Phenotype permutations (eg. randomizing M/F labelling) was also employed via limma through `camera()` as a more conservative test of pathway dysregulation. Pathways were considered enriched for an FDR < 0.05.

Weighted co-expression network analysis

A weighted protein co-expression network was built using the WGCNA package in R (version 1.72-5) (Langfelder & Horvath, 2008). Turbo samples were filtered for the entire universe of enriched proteins (ie., enriched in any component). Proteins expressed only in a single component and proteins with a variance of 0 were then removed, resulting in a matrix of 3142 proteins across 39 samples.

Soft power was established for a signed network using `pickSoftThreshold(type = "signed")` , with a model fit of 0.8. The scale-free topology fit index failed for reasonable powers (< 30), suggesting a strong correlation among large gene groups, thus violating the assumption of the scale-free topology approximation. As noted in the WGCNA package documentation, this is commonly seen with datasets containing multiple tissue types, and a lack of scale-free topology fit does not inherently invalidate the data(Langfelder & Horvath, 2008). Consequently, we selected the recommended soft power of 14 for signed networks with 30-40 samples.

Network adjacency was calculated with `adjacency(type = "signed")` and the topological overlap matrix was calculated with `TOMsimilarity(TOMtype = "signed")` , both using default settings. Modules were established through adaptive branch pruning `dynamicMods <- cutreeDynamic(dendro = geneTree, distM = dissTOM, deepSplit = 2, pamRespectsDendro = FALSE, minClusterSize = 30)` . Module eigengenes were then extracted for downstream analyses.

Terminal protein-protein interaction networks

Neuronally enriched proteins (the “neuronal proteome”) for each terminal compartment were used to generate large-scale protein-protein interaction networks in Cyto-

426 scape, via the stringApp (Doncheva et al., 2023; Shannon et al., 2003). For the periph-
427 eral terminals, a core cluster of 433 proteins were highly connected through high confi-
428 dence (0.7) protein-protein interactions (Szklarczyk et al., 2023). For the central termi-
429 nals, 2271 proteins formed the core cluster. For each compartment, these networks
430 were then clustered further. Here, community clustering was performed on the resulting
431 STRING network in Cytoscape, where the Girvan-Newman fast greedy algorithm was im-
432 plemented through ClusterMaker2 via GLay (Su et al., 2010; Utriainen & Morris, 2023).
433 Functional attributes within each cluster where then calculated via the stringApp,
434 against a background of the entire peripheral/central terminal proteome respectively.
435 Cluster numbers are somewhat arbitrary but correspond to the supplemental table out-
436 puts with full enrichment details.

437 *Oxaliplatin effects*

438 The effects of the chemotherapy agent oxaliplatin on explant cultures was tested using
439 limma. For DRG explants dissected from wildtype mice, oxaliplatin was administered at
440 25 µM, 50 µM and 100 µM concentrations (or vehicle). Proteins here were modelled as
441 Concentration.Condition, and contrasted within each concentration. For TurboID mice,
442 data were first filtered for Turbo samples and TurboID-enriched proteins prior to model-
443 ling by Condition. In each case, limma was used to contrast by treatment condition (ox-
444 aliplatin – vehicle). Proteins were considered differentially expressed with FDR < 0.05,
445 and abs(LFC) > 0.5. Downstream processing is described in the `*Pathway anal-*
446 *yses*` section.

447 Comparisons against LFC and overall expression were compared to previously pub-
448 lished, DIA-MS from *in vivo* oxaliplatin dosing (Yang et al., 2022)

449 *Rank-Rank Hypergeometric Overlap*

450 Rank-Rank Hypergeometric Overlap (RRHO) testing was performed on limma outputs.
451 Here, concordant and discordant gene profiles were calculated via the Stratified
452 method using ranked `-$\log_{10}$(p-values) * sign(effect size)`, implemented through the
453 RRHO2 library in R in line with their published recommendations (Cahill et al., 2018)

454 *STRING analysis*

455 STRING protein-protein interaction analyses were performed through Cytoscape 3.10.3
456 using the stringApp (Doncheva et al., 2023; Shannon et al., 2003) A list of DEPs for each
457 significant biological pathway were extracted from the ClusterProfiler output (see: *Path-*
458 *way analyses*) and loaded into the stringApp with default settings. Proteins were col-
459 oured based on differential expression in either TurboID only, or TurboID + bulk explant
460 datasets. Drug targets were determined via https://dgidb.org/, filtered for "regulatory
461 approval == Approved" (Cannon et al., 2024).

462 *Immunohistochemistry (IHC)*

For IHC the tissue was dissected as above with modifications: instead of the dorsal part of the SC, the whole L3-5 SC was taken out. The plantar paw punch contained not only the epidermis and dermis but all layers below the bones. The dissected tissue was fixed in 4% formalin/PBS for 3 h at 4°C, followed by overnight cryoprotection in 30% (w/v) sucrose at 4°C. For sectioning, the tissue was embedded in Tissue-Tek O.C.T. compound and frozen. Serial sections (SCN, DRG: 10 µm, SC: 30 µm, skin: 20-40 µm) were obtained using a cryostat and mounted on SuperFrost Plus slides. Sections were stored at -80°C until further processing.

Frozen sections were thawed at RT for 30 min before permeabilization and blocking in 0.4% Triton X-100/PBS containing 5% donkey serum for 30 min. Primary antibodies, diluted in 0.1% Triton X-100/PBS with 1% donkey serum, were applied overnight at 4°C. Following three washes in PBS, sections were incubated at RT for 2 h with Alexa Fluor-conjugated secondary antibodies in PBS containing 1% donkey serum and 0.1% Triton X-100. Unbound antibodies were removed by washing with PBS, and sections were mounted using SlowFade™ Glass Soft-set Antifade Mountant Medium containing 4',6-Diamidino-2-phenylindole (DAPI). Antibodies used are listed in STable 1.

Graphics

R base functions and the following libraries were used to compile plots unless otherwise described: ggplot2, ggbiplot, ComplexHeatmap, cowplot, gridExtra. Figures and schematics were designed in Inkscape.

Use of generative AI

Generative AI tools (OpenAI ChatGPT) were used solely to improve phrasing, clarity, and formatting. All scientific concepts, experimental designs, hypotheses, and project goals were developed by the research team. No synthetic or AI-generated data were included.

490 **Results**

491 We profiled the compartmental proteome of murine sensory neurons of DRG using the
492 well characterized Tg(Advillin-Cre) driver line (referred to here as Adv^{Cre}) (Barry et al.,
493 2023; Lopes et al., 2017; Zheng et al., 2019; Zurborg et al., 2011) crossed with the here
494 generated ROSA26$^{em1(TurboID)Bros}$ (TurboID$^{fl/fl}$) mouse line (Figure 1; please see Methods for
495 details on line generation, breeding, and husbandry). In Adv^{Cre+};TurboID$^{fl/fl}$ mice (referred
496 to here as Adv^{Cre};TurboID$^{fl/fl}$), TurboID is expressed in the cytoplasm of Advillin -positive
497 cells, resulting in promiscuous biotinylation of intracellular proteins, largely within sen-
498 sory neurons (Fig 1A). Respective control tissue was derived from littermates lacking
499 Adv^{Cre} (Adv^{Cre-};TurboID$^{fl/fl}$, referred to as TurboID$^{fl/fl}$). TurboID$^{fl/fl}$ samples do not express
500 TurboID and therefore serve as controls to account for endogenous biotinylation (Fig
501 1A). Tissue from wildtype mice were also collected for downstream comparisons (Fig
502 1B).

503 DRG neurons are pseudounipolar, with peripheral branching to target organs and cen-
504 tral branching to the spinal cord. To cover this spatial complexity, we isolated tissue
505 from the spinal cord (SC), dorsal root ganglia (DRG), sciatic nerve (SCN) and paw skin
506 after providing biotin in drinking water for 7 days (Branon et al., 2018; Rayaprolu et al.,
507 2022). Biotinylated proteins were enriched after tissue lysis followed by analysis using
508 liquid chromatography-coupled mass spectrometry (LC-MS/MS). Biotinylation in each
509 tissue of Adv^{Cre};TurboID$^{fl/fl}$ mice was confirmed by immunohistochemistry (Fig 1C, SFig
510 1A) and validated via Western blotting (SFig 1B). As expected, we see a clear enrichment
511 of biotin labelling (visualised via biotin-streptavidin) across all compartments (Fig 1C).
512 Using Western blotting, biotin signal was readily detected in tissue lysates but was less
513 prominent in skin (SFig 1). The latter may be due to low protein quantity after lysis, while
514 TurboID-positive afferents were evident by immunohistochemistry (Fig 1C, “skin”).

515 To generate a comprehensive and quantitative compartmental proteome atlas of DRG
516 neurons, we employed data-independent acquisition combined with parallel accumula-
517 tion–serial fragmentation (DIA-PASEF) mass spectrometry on Adv^{Cre};TurboID$^{fl/fl}$ and
518 Adv^{Cre} -negative control tissue (TurboID$^{fl/fl}$) (Fig 2, SFig 2-5, STable 1). Both overlapping
519 and distinct proteins were detected across DRG compartments (Fig 2A). A comparison
520 of Adv^{Cre};TurboID$^{fl/fl}$ with TurboID$^{fl/fl}$ controls shows more protein (SFig 2A) and more pro-
521 tein groups (SFig 2B) in Adv^{Cre};TurboID$^{fl/fl}$ samples. Samples also clustered by Adv^{Cre};Tur-
522 boID$^{fl/fl}$ compartment (Fig 2B) and across genotype (Fig 2C; SFig 2C). A full expression
523 matrix is available in STable 1.

524 *TurboID-mediated enrichment of proteins across compartments*

525 In Adv^{Cre};TurboID$^{fl/fl}$, proteins were considered enriched based on two criteria: A; pro-
526 teins detected in Adv^{Cre};TurboID$^{fl/fl}$ samples, but not in TurboID$^{fl/fl}$ samples, or B; proteins
527 significantly upregulated in Adv^{Cre};TurboID$^{fl/fl}$ samples compared to TurboID$^{fl/fl}$ ($\log_2$ fold
528 change (LFC) > 1, FDR < 0.05,see Methods) (Fig 2D-F, STable 2). These upregulated pro-
529 teins are referred to as differentially expressed proteins (DEPs). In addition, there are

530 few downregulated proteins, likely reflecting endogenous biotinylation such as in the
531 case of Acaca, Acacb, Mccc1, and Pcca (Fig 2D), which are routinely reported in proxim-
532 ity labelling studies (Dumrongprechachan et al., 2021; Sun et al., 2022).

533 All enriched proteins (based on criteria A and B above) were then combined, compared
534 across compartments (Fig 2E-F), and treated equally for all downstream analyses. We
535 identified the highest number of enriched proteins in the somata (DRG), followed by the
536 central terminals (terminals$_c$, SC), axons (SCN), and finally the peripheral terminals (ter-
537 minals$_p$, skin), with overlapping and distinct proteins (Fig 2E-F). Across the dynamic
538 range, we see an enrichment of neuronal cell type markers (e.g. Calca, Osmr, Piezo2)
539 and key nociceptor ion channels (e.g. Scn8a-10a, Trpv1) in Adv^{Cre};TurboID$^{fl/fl}$ samples
540 over TurboID$^{fl/fl}$ (Fig 2G, SFig 2D; full list of proteins in STable2).

541 Of note, in the skin, Adv^{Cre} is known to be expressed in both primary afferents and, to a
542 lesser extent, Merkel cells (Hunter et al., 2018). Because of this, we also detect Merkel
543 cell markers (e.g. Krt20) in our TurboID-enriched proteome of the skin but not in other
544 compartments (STable 2).

545 Taken together, our results yield a curated, enriched, and compartmental proteome of
546 murine primary sensory neurons ranging from hundreds to thousands of proteins per
547 compartment.

548 *Enrichment of proteins in neuronal terminals*

549 A complementary method to isolate neuronal compartments from the skin or spinal
550 cord is synaptosome isolation. Synaptosome preparations allow for the co-isolation of
551 pre- and post-synaptic machinery, enriched against other components in the tissue.
552 Recently, synaptosomes were profiled from both mouse and human skin without tailor-
553 ing for a specific cell type (Rawat et al., 2025). While the methods diverge in the exact
554 tissue extracted, both our proximity labelling approach and synaptosome profiling from
555 either species should extract the synaptic compartment of sensory terminals. To test
556 this, we assessed overlapping proteins in both enriched datasets and compared cellular
557 compartment pathways on this overlap (Fig 3A, mouse; Fig 3B, human). Indeed, we see
558 a significant enrichment for synapse-related pathway terms across mouse datasets
559 when comparing overlapping proteins (Fig 3A). There is also a trending enrichment when
560 comparing our mouse TurboID data from peripheral terminals with human skin synapto-
561 somes (Fig 3B, FDR ~ 0.07-0.09). The latter likely reflects reported similarities in identi-
562 fied proteins despite known species differences (Segelcke et al., 2023). Overall, this
563 comparison strengthens and validates our TurboID data in terminal endings and, at the
564 same time, complements the published synaptosome data. While both TurboID and
565 synaptosome profiling extracted synapse-related proteins (Fig. 3A), in our TurboID da-
566 taset we detect hundreds of proteins associated with synaptic compartments that were
567 not reported in the paw synaptosome fraction (Rawat et al., 2025), such as Syn1, Syn2,
568 and Synj1 (Fig. 3C, STable 3).

569 Next, we tested the overlap with a murine spinal cord synaptosome dataset (Casañas &
570 Montesinos, 2022), which reports both first- and higher-order synapses from a diverse
571 population of cell types (Fig 3D). Again, we see a positive enrichment of synapse terms
572 across datasets further validating that our TurboID approach successfully extracts rele-
573 vant synaptic compartments.

574 The use of Adv^{Cre} allows targeting the majority sensory neurons in the PNS (Zurborg et
575 al., 2011). To evaluate the representation of neuronal subpopulations within our da-
576 taset, we performed gene set enrichment analysis using a curated list of neuronal sub-
577 type markers from published deep RNA-seq data (Barry et al., 2023). As expected, the
578 strongest subtype enrichment was observed in the DRG, with significantly enriched sig-
579 natures for non-peptidergic (NP) and peptidergic nociceptors (PEP), as well as a mix of
580 low-threshold mechanoreceptors (LTMRs; including A-field-LTMR, C-LTMR, and AB-
581 LTMR) (Fig 3E). Across all compartments a positive trend for neuronal subtypes
582 emerged. Significant enrichments were particularly notable for NP nociceptors, A-field-
583 LTMR, and C-LTMR (Fig 3E, STable 3). These findings indicate that our proximity labelling
584 approach preserves the molecular diversity of sensory neuron subtypes across their an-
585 atomical domains.

586 *Compartmental sexual dimorphism*

587 To explore sex-specific molecular differences, we analysed differential protein expres-
588 sion between male and female mice across all compartments (SFig 3). With an FDR <
589 0.05, the TurboID-enriched proteome appeared largely conserved between sexes, with a
590 few exceptions in abs(LFC) > 1, such as Lgi1 and Sprr1a in central terminals and Brd4
591 and Palm2 in the peripheral terminals (SFig 3A, STable 4).

592 To gain broader biological insights, we also conducted gene set enrichment analysis us-
593 ing ranked LFC. This analysis revealed sexually dimorphic regulation of few pathways
594 (SFig 3B). In the peripheral terminals, we see differences in circulatory and vascular
595 pathways, whereas peptide biosynthesis and macromolecule biosynthesis show differ-
596 ences in the somata. We further explored potential sexual dimorphism through pheno-
597 type permutations as a more conservative approach and did not find any regulated
598 pathways in any compartment. Taken together, our data support a narrative of minimal
599 sexual dimorphism in TurboID-enriched proteomes.

600 *Functional signatures show separation by neuronal compartment*

601 To extract the corresponding functional signature, Gene Ontology (GO) pathway anal-
602 yses were performed against a background of all proteins expressed in the correspond-
603 ing tissues (Fig 4). While neuronal signatures were detected in each compartment, they
604 also exhibited functional specificity(Fig 4, STable 5). Primary afferents synapse on sec-
605 ondary order neurons in the dorsal horn of the spinal cord. This corresponds to the en-
606 richment of proteins involved in presynaptic function and synaptic signalling between
607 neurons, as well as vesicle-mediated transport, exocytosis, and other synapse-related

terms in the SC. The DRG contain neuronal somata, and, thus, corresponding functional enrichment matches expectations. Here, we observed the enrichment of proteins involved in mRNA processing, post-translational modification, and nuclear structures, in line with the biosynthetic activity expected in neuronal cell bodies.

The sciatic nerve consists of neuronal axons, as well as Schwann cells, fibroblasts, endothelial cells, and immune cells. Its neuronal proteome is enriched for myelination, cytoskeletal organization, and vesicle-mediated transport (STable 5). The “myelination” terms included nodal and paranodal proteins such as Cntn1 (Contactin-1) and Cntnap1 (Caspr1), as well as more generally expressed neuronal proteins like Ncam1, Nefl, Nefm, and Nefh. In addition, we found proteins more classically associated with myelin itself, such as Plp1, MBP, and MPZ , which also show expression in neuronal subtypes (Bhuiyan et al., 2024).

To explore functional organization across neuronal compartments, a signed weighted protein co-expression network was constructed on the neuronal proteome (Fig 5). The co-expression network was built using the WGCNA package in R with a soft power threshold of 14. Ten protein co-expression modules were identified (excluding the unassigned “grey” module), each comprising a minimum of 30 proteins (Fig 5A). Of these, 9 modules showed significant correlation with anatomical compartment (FDR < 0.05), while none were associated with sex (Fig 5B). The latter is in line with our pathway analysis (SFig 3) and consistent with earlier findings reporting a mild sexual dimorphism in DRG neurons (Barry et al., 2023; Tavares-Ferreira et al., 2022).

Specific modules showed clear compartmental specificity. For example, the brown module correlated strongly with the DRG (somata), while the blue module was associated with central terminals in the spinal cord. Conversely, several modules -including black, yellow, and green - were negatively associated with peripheral terminals, likely indicating a relative depletion of these proteins in distal axonal endings (Fig 5C–D). As expected, most modules exhibited strong alignment with one or more anatomical compartments, reinforcing the functional specialization of the sensory neuron proteome across space (Fig 5D).

Biological pathway analyses of these modules (against a background of all proteins used to build the co-expression network) was then performed (Fig 5E-H, STable 6). The `brown` module, which is positively correlated with the soma, reflects a group of proteins implicated in `translation`, `peptide metabolic process`, and `RNA processing` (Fig 5E). The blue module, which correlated with central terminals in the spinal cord, showed associated with `trans-synaptic signalling`, `regulation of neurotransmitter levels`, and `neurotransmitter transport`, reflecting synaptic functions in the dorsal horn (Fig 5F). The yellow module, which was positively correlated with soma and central terminals, relates to `protein polymerization`, `supramolecular fibre organization` and the `regulation of cellular component size` (Fig 5G).

No modules were positively correlated with the peripheral terminals - possibly due to the lower number of enriched proteins in peripheral terminals - but the most negative correlation is the black module. Although no biological pathways reached statistical significance in this module, cellular components related to `neuronal projection`, `somatodendritic compartment`, `postsynaptic density`, and `neuronal cell body` were among the annotations (Fig 5H).

TurboID proteomics provides a unique look at terminal endings

To explore protein interaction and functional organization in peripheral and central terminals, large-scale protein–protein interaction (PPI) networks were constructed using STRING (Fig 6, SFig 4) (Szklarczyk et al., 2023). A Girvan-Newman fast greedy algorithm was then used to generate community clusters (Su et al., 2010; Utriainen & Morris, 2023), and the functional enrichment of each cluster was calculated.

In the peripheral terminals (skin), the proteome revealed a diverse and functionally rich landscape, spanning protein transport, metabolic pathways, and signal transduction (Fig 6). A wide array of protein classes was detected, including SNARE complex components such as Syntaxin-7 and Snap25, as well as chaperones and ubiquitin-related proteins, such as Usp7 and heat shock proteins. Notably, even pain-associated ion channels (Trpv1, Scn10a, and Scn11a) were detected in clusters annotated for membrane trafficking and exocytosis. A full breakdown of each cluster enrichment is available in STable 7.

A similar pattern was observed in the central terminals of the spinal cord (SC), where clustering revealed extensive functional heterogeneity (SFig 4, STable 8). Enriched clusters included pathways involved in signal transduction, endosomal processing, and membrane trafficking—hallmark processes of synaptic signalling and neurotransmission (see Stable 8 for a functional breakdown).

Together, these analyses demonstrate that proximity labelling via TurboID enables unprecedented insights to the proteomic architecture of otherwise inaccessible neuronal compartments. This approach holds considerable promise for extracting functional, spatially resolved proteomes in defined cell types.

TurboID proteomics enables deeper insights than bulk tissue proteomes

To contextualize the advantages of TurboID-based proximity labelling, we compared our compartment-resolved proteomes to conventional bulk tissue proteomics. We harvested the skin, SCN, DRG and SC and determined the proteome using the same mass spectrometry-based workflow as applied to the TurboID samples above (SFig 5, STable 9). As expected (Barry et al., 2018; Xian et al., 2022), we detect several thousands (7000-9000) protein groups per tissue (SFig 5A), with samples clustering by tissue (SFig 5B). Consistent with earlier studies (Barry et al., 2018; Xian et al., 2022), we identified many neuronal proteins in bulk datasets. While these bulk tissue proteomes exhibited a large

685 overlap with TurboID-enriched proteomes, the latter identified dozens of additional pro-
686 teins in each compartment (STable 10; example for bulk skin versus TurboID-enriched
687 peripheral terminals, SFig 5D).

688 To additionally assess the enrichment achieved by TurboID proteomes, we compared
689 the extent of immune cell subtypes present in TurboID proteomes versus bulk tissue
690 proteomes. (SFig 5E). ImmuCellAI (Miao et al., 2022) was used to calculate an "immune
691 infiltration score", which reflects a composite GSEA enrichment across immune cell
692 subtypes. Indeed, compared to bulk tissue samples, we obtained a reduced immune
693 signature in TurboID-enriched proteomes, further validating our approach (SFig 5E).

694 This highlights two key advantages of TurboID-based proteomics: First, it facilitates the
695 enrichment of proteins in a Cre-dependent manner within the same tissue. Second, Tur-
696 boID enhanced detection sensitivity in tissues with sparse cellular content, such as pe-
697 ripheral terminals in the skin. In these regions, the detection of sensory neuron-specific
698 proteins — particularly ion channels — has been challenging and largely unsuccessful
699 using bulk proteomics (Dyring-Andersen et al., 2020; Xian et al., 2022). In contrast, Tur-
700 boID-based profiling recovered functionally important signatures in peripheral termi-
701 nals, including prominent drug targets such as Scn10a, Scn11a, and Trpv1, providing
702 molecular access to previously inaccessible compartments (Fig 6, SFig 5D).

703 Together, these data underscore the power of TurboID-based proteomics to resolve cell
704 type-specific proteomes within complex tissues. Importantly, this strategy opens a path
705 to study the proteome dynamics of afferent terminals in disease models and in re-
706 sponse to pharmacological interventions.

707 *TurboID proteomics reveals neuron-enriched changes in response to oxaliplatin treat-*
708 *ment*

709 Next, we tested the utility of our TurboID workflow in a pharmacological context. For
710 this, we turned to oxaliplatin, a chemotherapeutic agent. Chemotherapy-induced pe-
711 ripheral neuropathy (CIPN) is a common and often painful condition affecting the pe-
712 ripheral nervous system, known to impact neuronal and non-neuronal cells in the DRG
713 (Sisignano et al., 2014). In adherence to the 3Rs of animal research, we employed a
714 DRG explant model to explore oxaliplatin-induced changes in neuronal somata (Fig 7,
715 SFig 6-7, STables 11-16). Mirroring the compartmental proteomes above, we deter-
716 mined the bulk proteome of DRG explants from wildtype mice and, thereafter, com-
717 pared these data with TurboID-enriched proteomes obtained from Adv^{Cre};$TurboID^{fl/fl}$
718 mice (versus $TurboID^{fl/fl}$ controls).

719 In the bulk proteome of wildtype mice we identified ~7200 protein groups (SFig 6A, STa-
720 ble 11), with clustering driven by oxaliplatin concentration (SFig 6B-C). Consistent with
721 earlier studies, oxaliplatin exposure led to widespread proteome changes, including al-
722 terations in known neuronal proteins (SFig 6D-E, STable 12). When comparing DEPs
723 from our DRG explant data to previous work *in vivo* (Yang et al., 2022), we see a strong

correlation of protein expression (SFig 6F). We next employed a rank-rank hypergeometric overlap test and observed good concordance for DEPs across both datasets (SFig 6G). These comparisons suggest similar oxaliplatin-induced proteome changes validating our explant model.

Next, we treated DRG explants from Adv^{Cre};TurboID$^{fl/fl}$ mice and TurboID$^{fl/fl}$ controls with oxaliplatin or its vehicle (Fig 7, SFig 7, STable 13). As expected, Adv^{Cre};TurboID$^{fl/fl}$ explants exhibited prominent protein enrichment compared to TurboID$^{fl/fl}$ controls (SFig 7A). Samples clustered by genetics in the first principal component (PC), with slight separation by drug treatment in the second PC (SFig 7B). In both oxaliplatin-treated (SFig 7C, left) and vehicle-treated (SFig 7C, right) explants, Adv^{Cre};TurboID$^{fl/fl}$ samples (vs TurboID$^{fl/fl}$) showed robust TurboID-mediated enrichment with ~ 2500 protein groups per condition (SFig 7D, STable 14).

Within this TurboID-enriched proteome, we detected a substantial number of DEPs after oxaliplatin treatment compared to vehicle-treated controls (Fig 7A, STable 15). Notably, these differences were only partially reflected in the bulk explant proteome (Fig 7B). Even so, we saw a high rank-rank hypergeometric overlap between the bulk explant and TurboID-enriched proteomes after oxaliplatin treatment (Fig 7C), and a high semantic similarity across DEPs (Fig 7D).

Next, we assessed DEP-associated functions in DRG explant proteomes. After oxaliplatin treatment, pathways related to amino acid transport and cell adhesion were downregulated in the TurboID-enriched proteome (Fig 7E, STable 16). To further dissect these pathways, we constructed a corresponding PPI network based on pathway-associated DEPs (Fig 7F). This revealed prominent downregulation across multiple functional modules (Fig 7Fi). While some of these DEPs were regulated in both bulk and TurboID-enriched explant proteomes, others were only detected in the TurboID-enriched proteome (Fig 7Fii). The latter included Trpv1, Scn11a, and Calca, as well as the central module with Itgb1, Lama2, and Rock2 – all of which are targets of approved drugs (https://dgidb.org/). For example, capsaicin patches (target: Trpv1) for pain, and the kinase inhibitor Vandetanib (target: Rock2), which is prescribed against a subset of thyroid cancers (Viola et al., 2016) (https://dgidb.org/).

These findings illustrate the enhanced resolution of TurboID-mediated proteomics, uncovering molecular changes that may be masked in bulk tissue analyses. Thus, our TurboID workflow offers a powerful tool to dissect disease mechanisms and treatment effects in complex tissues.

Discussion

As a generalized proof-of-concept, we demonstrate how our TurboID (TurboID$^{fl/fl}$) mouse line enables cell-type-specific proteomic labelling across anatomically distinct compartments. We paired it with Adv^{Cre} to target TurboID expression to primary sensory neurons of DRG, resulting in robust biotinylation across neuronal compartments. Using DIA-PASEF mass spectrometry, we provide unprecedented insights into compartment-specific DRG neuron proteomes from peripheral to central terminals.

This spatial resolution is particularly significant in the peripheral terminals of DRG neurons in the skin. Peripheral nerve endings are typically characterized by immunohistochemistry and have remained largely inaccessible to unbiased omics approaches. Neither our bulk proteomic data nor previous high-coverage DIA-MS datasets from mouse skin or human skin were able to profile key sensory neuron markers (Dyring-Andersen et al., 2020; Rawat et al., 2025; Xian et al., 2022). Sparse molecular signatures are often masked by dominant cell types, likely restricting the detection of neuronal signatures in the skin. Similar considerations apply to transcriptome profiling. While single-cell and single-nucleus RNA sequencing are valuable for cell-type-resolved transcriptomes, they are typically limited to somata within the DRG, lack proteomic resolution, and do not capture distal compartments (Grindberg et al., 2013; Matzinger et al., 2023). The expansion of spatial sequencing helps address many of these issues, although recent spatial transcriptomics of the sciatic nerve have not resolved neuron-specific clusters (Ferreira et al., 2024), and to our knowledge, a high resolution spatial-seq dataset including peripheral terminals in the skin is still missing. Here, we used TurboID-based proteomics and were able to profile neuronal markers and prominent drug targets such as Trpv1, Scn10a, and Scn11a in the peripheral terminals. Consequently, at present, our TurboID-based proteomic atlas offers a unique spatial profile spanning the extent of murine DRG sensory neuron compartments. We expect that our data will provide a valuable protein-level stepping stone for ongoing efforts to expand spatial -omics to previously inaccessible cell types and compartments.

A strength of the TurboID approach is the ability to probe proteins enriched in one compartment over others. Many of the proteins enriched in central terminals relate to synapse function and vesicle trafficking as expected. Alongside, we also detected several proteins relevant to pain and somatosensation such as Lgi1, Stoml3, and Cacng2 (stargazin) (Bortsov et al., 2019; Farah et al., 2024; Lafrenière & Rouleau, 2011; Wetzel et al., 2017). In the axon, we a number of functionally relevant proteins were enriched, including Arhgap32, Atp1a2, and Kcnab3. Arhgap32 (aka Grit, Rics, or p250GAP) is a GTPase regulator that interacts with Ntrk1 to regulate neurite outgrowth (Kannan et al., 2012; Nakamura et al., 2002). Atp1a2 encodes an ATPase Na+/K+ transporting subunit with a role in migraine (Murata et al., 2020), and Kcnab3 is a shaker-type potassium axillary unit, likely expressed in the paranodal and juxtaparanodal region (Rasband & Trimmer, 2001). Shaker-type channels are general involved in regulating excitability (Rasband et al., 2001), but the implications of Kcnab3 expression remains unclear and follow-up

work for all candidates is warranted for a better understanding of DRG sensory neuron functions.

While not a main focus of this study, we were also able to probe neuronal sex differences across compartments, expanding on previously reported sexual dimorphism in mouse and humans (Barry et al., 2023; North et al., 2019; Tavares-Ferreira et al., 2022; Xian et al., 2022). Mirroring these data across sensory neuron subtypes, we see marginal differences between male and female neurons under naïve conditions.

To highlight how TurboID proximity labelling could be exploited to study functional changes in a clinically-relevant disease context, we investigated proteome dynamics in a DRG explant model of CIPN. Exposure to oxaliplatin resulted in widespread proteomic alterations in both bulk and TurboID-enriched proteomes, as expected. While DEP sets varied between bulk and TurboID enrichments, semantic similarity of enriched pathways was high, indicating shared biological responses. A major benefit of our TurboID approach in explants is the neuronal enrichment, highlighting disruption to organic anion and amino acid transport pathways. This contrasts the more generalized effect of oxaliplatin seen in the whole DRG proteome composed of diverse cell types and highlights the practicality of the DRG explant model for rapid *in vitro* screening of neurotoxic effects.

Transporter disruptions have widely been reported in the context of CIPN (Filipski et al., 2009; Huang et al., 2020; Litke et al., 2022; Schulte & Ho, 2019; Sisignano et al., 2014; Sprowl et al., 2013). Organic cation transporters, such as Oct2, have been implicated in oxaliplatin uptake by sensory neurons, and their activity contributes to neurotoxicity (Sisignano et al., 2014; Sprowl et al., 2013). Similarly, organic anion-transporting polypeptides (OATPs) affect CIPN pathophysiology (Leskelä et al., 2011; Li et al., 2023; Schulte & Ho, 2019). Impaired transporter function can lead to drug accumulation in DRG, contributing to mitochondrial dysfunction, oxidative stress, and neuroinflammation, all of which underlie CIPN pathogenesis (Sisignano et al., 2014). In our study, several transporters were downregulated in response to oxaliplatin treatment. Some changes are evident across neuronal and bulk proteomes (e.g. Slc7a14, Slc2a3), while the dysregulation of others (e.g. Slc1a4, Slc3a2, Slc33a1) could only be detected when studying the neuronal proteome. Pursuing these transport pathways may provide novel strategies to mitigate CIPN while preserving the anticancer efficacy of chemotherapy, with promising attempts to target transporters already in development (Li et al., 2023).

When paired with conventional bulk analyses, our approach offers a multi-layered view of the proteomic landscape in response to drug treatment and in disease models, complementing and extending *in vivo* work.

Limitations

This study provides a quantitative, compartmental proteomic atlas of DRG sensory neurons and serves as a valuable reference for the field. However, it is not exhaustive, and

839 reports a neuronal-enriched proteome (opposed to neuronal-specific). Particularly, the
840 detection of low-abundance transmembrane proteins is known to be challenging. It may
841 be further improved through advances in mass spectrometry sensitivity, biotinylation
842 efficiency, and sample preparation protocols. Fewer protein identifications were ob-
843 tained in peripheral terminals and axons - a likely reflection of heterogenous tissue
844 composition and sparse neuronal content - resulting in a relative bias toward somata
845 and central terminals, where neuronal protein density is higher. While our results repre-
846 sent a robust starting point, future studies with deeper coverage and within-compart-
847 ment comparisons under various biological conditions will be critical for advancing our
848 knowledge about the molecular features of terminal regions. Likewise, deeper coverage
849 and higher sensitivity will enable future work on differentiating sensory neuron subtypes
850 and their sparse peripheral terminals.

851 *Future directions*

852 A key advantage of using TurboID transgenic mice is the opportunity to interrogate oth-
853 erwise inaccessible cellular compartments. Prior work in both mice and humans has
854 shown alterations in intraepidermal nerve fibre density across painful conditions
855 (Middleton et al., 2021; Schmidt et al., 2022). Pairing our compartmental proteome with
856 *in vivo* functional testing will provide a rich understanding of the underlying molecular
857 changes and their correlation with behavioural outcomes in future studies.

858 Another major benefit lies in the flexibility of Cre-based recombination. Pseudobulk
859 analyses are frequently used in scRNA-seq (and spatial) transcriptomics to compare
860 within cell-type changes across conditions. Paired to adequate transgenic drivers and
861 downstream DIA-MS, TurboID$^{fl/fl}$ can be used to generate a corresponding proteome for
862 multi-omic analyses within cell types. In the context of sensory neurons, this can be
863 subtype targeting (e.g. Mrgprd^{Cre} or Th^{Cre}) or injury-specific targeting (e.g. Atf3^{Cre}) (Cooper
864 et al., 2024; Zheng et al., 2019). More broadly, our approach could be extended to di-
865 verse cell types, such as fibroblasts in the skin, satellite glia in the DRG, or interneurons
866 in the dorsal horn (to name a few).

867 **Conclusions**

868 In this study, we generated a TurboID$^{fl/fl}$ transgenic mouse, using it to systematically pro-
869 file the proteomes of DRG sensory neuron compartments. Spanning from peripheral to
870 central terminals, we provide a proteomic atlas across DRG sensory neuron compart-
871 ments. Our findings reveal compartment-specific protein distributions that reflect spe-
872 cialized neuronal functions. Furthermore, we report previously unknown changes in an
873 explant model of chemotherapy-induced peripheral neuropathy. Taken together, our
874 methodological workflow and obtained data serve as a highly valuable resource for
875 studying neuronal specialization and proteome dynamics in the peripheral nervous sys-
876 tem.

877

Code Availability

All code is available at https://github.com/aliibarry/turboID.

Data Availability

The mass spectrometry proteomics data, including metadata, fasta, and gene group matrices for each dataset have been deposited to the ProteomeXchange Consortium via the PRIDE(Perez-Riverol et al., 2022) partner repository with the dataset identifier PXD062198. Processed data are also available on github (https://github.com/aliibarry/turboID/data/).

For queries regarding the TurboID mouse line please contact Nils Brose (brose@MPI-NAT.mpg.de) or Noa Lipstein (lipstein@FMP-berlin.de).

Acknowledgements

The authors would like to thank Christiane Harenberg, Dayana Warnecke and Mia Wzietek from the AGCTLab (Department of Molecular Neurobiology, Max Planck Institute, MPI, for Multidisciplinary Sciences, Goettingen) for expert technical assistance and genotyping, as well as Nicole Kanta and Sabrina Grundtner (University of Vienna) for their excellent assistance. We are grateful to the staff of the animal house of the MPI and of the mouse house at the Division of Pharmacy (University of Vienna) for expert mouse husbandry and support. We further thank Dr. Kimmina, Dr. Schraepler, Dr. Fuenfschilling and Dr. Papadopoulos (all at MPI) for their support in all mouse-related issues, as well as Elham Barkhordar and Dr. Dominic Winter (University of Bonn, Germany) for initial discussions about the BioID approach. We thank all members of the Schmidt laboratory for fruitful discussions.

This work was funded in part by the Austrian Science Fund (FWF) [10.55776/P36554] (to MS), the University of Vienna (to MS), the Max Planck Society, the German Research Foundation, Excellence Strategy EXC-2049–390688087 (to NL), and CRC 1286 "Quantitative Synaptology", project A11 (to NL) and A09 (to NB).

Author Contributions

Method optimization, sample preparation and data collection were performed by JRS with input from FX, DVG, and MS. Analyses were performed by AMB, with input from JRS, FX, and MS. Mass spectrometry was performed by FX with input from JRS and DGV. Conceptualization and funding acquisition by MS with input from DGV. Oxaliplatin experiments were performed by JRS and TH. TurboID$^{fl/fl}$ mice were conceived, designed, generated and validated by NB, FB, DS, and NL. Manuscript was written by AMB, JRS, and MS with input from all authors. All authors approved the submitted version.

Declaration of interests

The authors declare no conflicts of interest related to this work. NL is a scientific advisory board member of TRACE Neuroscience inc. MS and DGV maintain an ongoing scientific collaboration with Bruker, but this collaboration had no influence on the content of the manuscript.

920 **Figure Legends**

921 **Figure 1.** Adv^{Cre};TurboID$^{fl/fl}$ mice were used to target the DRG neuron proteome. A. Schema over-
922 view for biotinylation of DRG proteins. Adv^{Cre};TurboID$^{fl/fl}$ and TurboID$^{fl/fl}$ mice were provided bio-
923 tin-enriched water; in Adv^{Cre};TurboID$^{fl/fl}$, this promotes the biotinylation of proteins within Ad-
924 villin-expressing (+) cells. Advillin-negative (-) cells and tissues from TurboID$^{fl/fl}$ mice only con-
925 tain endogenously biotinylated proteins. Tissues were lysed and biotinylated proteins were puri-
926 fied followed by downstream LC-MS/MS on a timsTOF HT in DIA-PASEF mode. B. Bulk proteo-
927 mes were isolated from wildtype (WT) mice for each corresponding tissue in A. C. Representa-
928 tive immunohistochemistry from TurboID$^{fl/fl}$ (control) and Adv^{Cre};TurboID$^{fl/fl}$ mice across tissues.
929 Cyan, DAPI. Magenta, Streptavidin-555 (labelling biotin). Scale bar = 50 µm.

930 **Figure 2**. Protein enrichment by TurboID. A. Protein counts by sample, with "overlap" represent-
931 ing proteins detected in both Adv^{Cre};TurboID$^{fl/fl}$ and TurboID$^{fl/fl}$ control tissue. B-C. PCA for
932 Adv^{Cre};TurboID$^{fl/fl}$ (B) and both Adv^{Cre};TurboID$^{fl/fl}$ and TurboID$^{fl/fl}$ (C). D. Volcano plots highlight
933 DEPs based on their LFC in Adv^{Cre};TurboID$^{fl/fl}$ versus TurboID$^{fl/fl}$. E. Numbers of enriched proteins,
934 including both DEPs from D (Adv^{Cre};TurboID$^{fl/fl}$ vs TurboID$^{fl/fl}$), as well as proteins detected in
935 Adv^{Cre};TurboID$^{fl/fl}$ but not TurboID$^{fl/fl}$ controls ("not in TurboID$^{fl/fl}$"). F. Comparison of protein en-
936 richment across tissues. G. Dynamic range plot for previously published neuronal and subtype
937 markers in the DRG (LaCroix-Fralish et al., 2007; Tavares-Ferreira et al., 2022; Zheng et al.,
938 2019), plotted as the median expression across all compartments.

939 **Figure 3.** Validation against published datasets. A-C. Comparison of our TurboID proteome in
940 peripheral terminals with Rawat et al., (2025) skin synaptosome proteomics, via overenrichment
941 analysis for cellular compartment terms. A. Overlapping pathways with the murine synapto-
942 some dataset. B. Overlapping pathways with the human skin synaptosome dataset. C. Proteins
943 enriched in our TurboID peripheral terminal data but not detected in the murine synaptosome
944 dataset. D. Comparison of our TurboID proteome in central terminals to spinal cord (SC) synap-
945 tosome data from Casañas & Montesinos (2022). E. Gene set enrichment analysis against cus-
946 tom DRG subtype gene lists. GS = gene set. NP = non-peptidergic. PEP = peptidergic. PROP =
947 proprioceptor. LTMR = low threshold mechanoreceptor. LFC = $\log_2$ fold change. terminals$_p$ = pe-
948 ripheral terminals (skin); terminals$_c$ = central terminals (SC). Count = the number of proteins de-
949 tected within each gene list, per compartment. Extended data in STable 3.

950 **Figure 4**. Pathway and neuronal subpopulation enrichment across compartments. Schematic
951 highlights the GO over-enrichment analysis per tissue. BP = biological pathway; CC = cellular
952 compartment. (X) term rank by adjusted p-value. % represents the GO term/neuronal enrich-
953 ment. Please see STable 5 for corresponding data.

954 **Figure 5**. Weighted co-expression network of the TurboID-enriched proteome. A. Dendrogram
955 with minimum 30 proteins per module. B. Correlation between modules and traits (compart-
956 ment or sex). C. ME (module eigengene) value per sample. D. Module eigengene (ME) separation
957 by component and module for modules significantly correlated to tissue (FDR < 0.05, BH correc-
958 tion). E-H. Biological pathway (E-G) and cellular compartment (H) analysis for modules of inter-
959 est. E. brown, F. blue, G. yellow, H. black. No biological pathways or cellular components were
960 significant for the green module. p.adjust = adjusted p-value. qscore = $-\log_{10}$(p.adjust). termi-
961 nals$_p$ = peripheral terminals (skin); terminals$_c$ = central terminals (SC).

Figure 6. Community clustering of the peripheral terminal proteome, with edges denoting high confidence protein-protein interactions. Protein nodes are coloured by cluster, and clusters are described by functional summaries with proteins of interest highlighted. Full functional enrichments are available in STable 7.

Figure 7. Oxaliplatin-treated Adv^{Cre};TurboID$^{fl/fl}$ explants highlight neuronal dysregulation. A. Volcano plot of the TurboID proteome (Adv^{Cre};TurboID$^{fl/fl}$) for oxaliplatin vs vehicle,. B. DEP overlap (oxaliplatin vs vehicle) between bulk (WT, grey) and TurboID (orange) explant proteomes. C. Correlation between LFC for overlapping DEPs in B. D. Semantic similarity between TurboID and bulk DEPs. E. Neuronal biological pathway downregulation after oxaliplatin treatment, highlighting protein counts which overlap across pathways. F. STRING protein-protein interaction network for DEPs in regulated pathways from E. i, LFC in the TurboID-enriched proteome. ii, Approved drug targets from dgidb.org are highlighted with dashed circles. DEPs detected only in the TurboID-enriched proteome are in orange, those overlapping with the bulk analysis are in grey. LFC, log2-fold change.

Supplemental Figures

Supplemental Figure 1. A. Immunohistochemistry of Adv^{Cre};TurboID$^{fl/fl}$ with sensory neuron markers peripherin and NF200. Scale bar = 50 um. B. Western Blot analyses for TurboID (left) and B-actin loading controls (right). Adv^{Cre};TurboID$^{fl/fl}$ (T) and TurboID$^{fl/fl}$ (TC) samples for each tissue were loaded. DRG, dorsal root ganglia; SCN, sciatic nerve; SC, lumbar spinal cord.

Supplemental Figure 2. DIA-PASEF mass spectrometry of Adv^{Cre};TurboID$^{fl/fl}$ and TurboID$^{fl/fl}$ control samples across sensory neuron compartments. A-B. Summed expression (A), and Protein Group counts (B) by tissue and TurboID status. C. Heatmap of ion channel expression across all samples. D. Dynamic range for proteins of interest in Adv^{Cre};TurboID$^{fl/fl}$ samples plotted as expression (log_2 Intensity) per component. terminals$_p$ = peripheral terminals (skin); terminals$_c$ = central terminals (SC). Relates to Figure 2.

Supplemental Figure 3. Sexual dimorphism across neuronal compartments. A. Differential protein expression by compartment, comparing male vs female mice within TurboID-enriched proteomes. Significant proteins are in pink. LFC = log_2 fold change B. Biological Pathway analysis for peripheral terminals and DRG on ranked fold changes between male and female samples. Counts reflect the number of proteins in each respective term. terminals$_p$ = peripheral terminals; terminals$_c$ = central terminals.

Supplemental Figure 4. Community clustering of the TurboID-enriched central terminal proteome, with edges denoting high confidence protein-protein interactions. Protein nodes are coloured by cluster, and clusters are described by functional summaries with proteins of interest highlighted. Full functional enrichments are available in Stable 8.

Supplemental Figure 5. Bulk proteomes of the four analysed tissues from wildtype mice. A. Protein Group (PG) counts per tissue. B. PCA by tissue. C. Heatmap of the scaled expression of selected key neuronal genes. D. Comparison of key neuronal proteins between peripheral terminals of Adv^{Cre};TurboID$^{fl/fl}$, those of TurboID$^{fl/fl}$, and bulk proteomes obtained from skin samples. E. Depletion of ImmuCellAI immune cell signatures is evident in Adv^{Cre};Turbo$^{fl/fl}$ samples compared to corresponding bulk samples from wildtype tissues.

Supplemental Figure 6. Bulk Proteomics of DRG explants exposed to oxaliplatin (25, 50 or 100 uM) or vehicle (Veh). A. Protein counts. B. PCA across sample conditions shows clear separation of oxaliplatin-treated samples versus Veh-treatment. C. Correlation across samples, labelled as oxaliplatin (25, 50, 100) or vehicle (Veh). D. Heatmap across selected key neuronal proteins. E. Differentially expressed proteins (DEPs) between 100 uM oxaliplatin- and Vehicle-treated DRG explants using bulk proteomics. Purple dots indicate significantly regulated proteins (FDR < 0.05, LFC > 0.5). F. Correlation of relative protein abundance between our DEP dataset (from E) with previously published proteome data from *in vivo* oxaliplatin-treated DRG (Yang et al., 2022). G. Rank-rank hypergeometric overlap between our DEP dataset (in E) and DEPs of the previously published oxaliplatin-treated proteome (Yang et al., 2022). DEP, differentially expressed protein; LFC, $\log_2$ fold change.

Supplemental Figure 7. Proteomics of DRG explants from Adv^{Cre};$TurboID^{fl/fl}$ and $TurboID^{fl/fl}$ mice. A. Protein group counts across conditions. B. PCA across conditions. C. Differentially expressed proteins between Adv^{Cre};$TurboID^{fl/fl}$ and $TurboID^{fl/fl}$ explant samples, for both vehicle and oxaliplatin-treated explants. D. Numbers of enriched proteins, including both DEPs from C (Adv^{Cre};$TurboID^{fl/fl}$ vs $TurboID^{fl/fl}$), as well as proteins detected in Adv^{Cre};$TurboID^{fl/fl}$ but not $TurboID^{fl/fl}$ controls ("not in $TurboID^{fl/fl}$"), please see methods for details. LFC = $\log_2$ fold change. Ox = oxaliplatin. V = vehicle.

References

Barry, A. M., Sondermann, J. R., Sondermann, J.-H., Gomez-Varela, D., & Schmidt, M. (2018). Region-resolved quantitative proteome profiling reveals molecular dynamics associated with chronic pain in the PNS and spinal cord. *Frontiers in Molecular Neuroscience*, *11*(August), 259. https://doi.org/10.3389/fnmol.2018.00259

Barry, A. M., Zhao, N., Yang, X., Bennett, D. L., & Baskozos, G. (2023). Deep RNA-seq of male and female murine sensory neuron subtypes after nerve injury. *Pain*, *164*(10), 2196–2215. https://doi.org/10.1101/2022.11.21.516781

Bhuiyan, S. A., Xu, M., Yang, L., Semizoglou, E., Bhatia, P., Pantaleo, K. I., Tochitsky, I., Jain, A., Erdogan, B., Blair, S., Cat, V., Mwirigi, J. M., Sankaranarayanan, I., Tavares-Ferreira, D., Green, U., McIlvried, L. A., Copits, B. A., Bertels, Z., Del Rosario, J. S., ... Renthal, W. (2024). Harmonized cross-species cell atlases of trigeminal and dorsal root ganglia. *Science Advances*, *10*(25). https://doi.org/10.1126/sciadv.adj9173

Biesemann, C., Grønborg, M., Luquet, E., Wichert, S. P., Bernard, V., Bungers, S. R., Cooper, B., Varoqueaux, F., Li, L., Byrne, J. A., Urlaub, H., Jahn, O., Brose, N., & Herzog, E. (2014). Proteomic screening of glutamatergic mouse brain synaptosomes isolated by fluorescence activated sorting. *EMBO Journal*, *33*(2). https://doi.org/10.1002/embj.201386120

Bortsov, A. V., Devor, M., Kaunisto, M. A., Kalso, E., Brufsky, A., Kehlet, H., Aasvang, E., Bittner, R., Diatchenko, L., & Belfer, I. (2019). CACNG2 polymorphisms associate with chronic pain after mastectomy. *Pain*, *160*(3). https://doi.org/10.1097/j.pain.0000000000001432

Branon, T. C., Bosch, J. A., Sanchez, A. D., Udeshi, N. D., Svinkina, T., Carr, S. A., Feldman, J. L., Perrimon, N., & Ting, A. Y. (2018). Efficient proximity labeling in living cells and organisms with TurboID. *Nature Biotechnology*, *36*(9). https://doi.org/10.1038/nbt.4201

Cahill, K. M., Huo, Z., Tseng, G. C., Logan, R. W., & Seney, M. L. (2018). Improved identification of concordant and discordant gene expression signatures using an updated rank-rank hypergeometric overlap approach. *Scientific Reports*, *8*(1). https://doi.org/10.1038/s41598-018-27903-2

Cannon, M., Stevenson, J., Stahl, K., Basu, R., Coffman, A., Kiwala, S., McMichael, J. F., Kuzma, K., Morrissey, D., Cotto, K., Mardis, E. R., Griffith, O. L., Griffith, M., & Wagner, A. H. (2024). DGIdb 5.0: rebuilding the drug-gene interaction database for precision medicineãnd drug discovery platforms. *Nucleic Acids Research*, *52*(D1). https://doi.org/10.1093/nar/gkad1040

Casañas, J. J., & Montesinos, M. L. (2022). Proteomic characterization of spinal cord synaptoneurosomes from Tg-SOD1/G93A mice supports a role for MNK1 and local translation in the early stages of amyotrophic lateral sclerosis. *Molecular and Cellular Neuroscience*, *123*(June). https://doi.org/10.1016/j.mcn.2022.103792

Concordet, J. P., & Haeussler, M. (2018). CRISPOR: Intuitive guide selection for CRISPR/Cas9 genome editing experiments and screens. *Nucleic Acids Research*, *46*(W1). https://doi.org/10.1093/nar/gky354

Cooper, A. H., Barry, A. M., Chrysostomidou, P., Lolignier, R., Wang, J., Redondo Canales, M., Titterton, H. F., Bennett, D. L., & Weir, G. A. (2024). Peripheral nerve injury results in a biased loss of sensory neuron subpopulations. *Pain*. https://doi.org/10.1097/j.pain.0000000000003321

Cox, J., Hein, M. Y., Luber, C. A., Paron, I., Nagaraj, N., & Mann, M. (2014). Accurate proteome-wide label-free quantification by delayed normalization and maximal peptide ratio extraction, termed MaxLFQ. *Molecular and Cellular Proteomics*, *13*(9). https://doi.org/10.1074/mcp.M113.031591

Demichev, V., Messner, C. B., Vernardis, S. I., Lilley, K. S., & Ralser, M. (2020). DIA-NN: neural networks and interference correction enable deep proteome coverage in high throughput. *Nature Methods*, *17*(1). https://doi.org/10.1038/s41592-019-0638-x

Dingar, D., Kalkat, M., Chan, P. K., Srikumar, T., Bailey, S. D., Tu, W. B., Coyaud, E., Ponzielli, R., Kolyar, M., Jurisica, I., Huang, A., Lupien, M., Penn, L. Z., & Raught, B. (2015). BioID

identifies novel c-MYC interacting partners in cultured cells and xenograft tumors. *Journal of Proteomics*, *118*. https://doi.org/10.1016/j.jprot.2014.09.029

Doench, J. G., Fusi, N., Sullender, M., Hegde, M., Vaimberg, E. W., Donovan, K. F., Smith, I., Tothova, Z., Wilen, C., Orchard, R., Virgin, H. W., Listgarten, J., & Root, D. E. (2016). Optimized sgRNA design to maximize activity and minimize off-target effects of CRISPR-Cas9. *Nature Biotechnology*, *34*(2). https://doi.org/10.1038/nbt.3437

Doncheva, N. T., Morris, J. H., Holze, H., Kirsch, R., Nastou, K. C., Cuesta-Astroz, Y., Rattei, T., Szklarczyk, D., von Mering, C., & Jensen, L. J. (2023). Cytoscape stringApp 2.0: Analysis and Visualization of Heterogeneous Biological Networks. *Journal of Proteome Research*, *22*(2). https://doi.org/10.1021/acs.jproteome.2c00651

Dumrongprechachan, V., Salisbury, R. B., Soto, G., Kumar, M., MacDonald, M. L., & Kozorovitskiy, Y. (2021). Cell-type and subcellular compartment-specific APEX2 proximity labeling reveals activity-dependent nuclear proteome dynamics in the striatum. *Nature Communications*, *12*(1). https://doi.org/10.1038/s41467-021-25144-y

Dyring-Andersen, B., Løvendorf, M. B., Coscia, F., Santos, A., Møller, L. B. P., Colaço, A. R., Niu, L., Bzorek, M., Doll, S., Andersen, J. L., Clark, R. A., Skov, L., Teunissen, M. B. M., & Mann, M. (2020). Spatially and cell-type resolved quantitative proteomic atlas of healthy human skin. *Nature Communications*, *11*(1). https://doi.org/10.1038/s41467-020-19383-8

Farah, A., Patel, R., Poplawski, P., Wastie, B. J., Tseng, M., Barry, A. M., Daifallah, O., Dubb, A., Paul, I., Lao Cheng, H., Feroz, F., Su, Y., Chan, M., Zeilhofer, H. U., Price, T., Bennett, D. L., Bannister, K., & Dawes, J. M. (2024). A role for leucine-rich, glioma inactivated 1 in regulating pain sensitivity. *Brain*. https://doi.org/10.1093/brain/awae302/7762306

Filipski, K. K., Mathijssen, R. H., Mikkelsen, T. S., Schinkel, A. H., & Sparreboom, A. (2009). Contribution of organic cation transporter 2 (OCT2) to cisplatin-induced nephrotoxicity. *Clinical Pharmacology and Therapeutics*, *86*(4). https://doi.org/10.1038/clpt.2009.139

Fornaro, M., Sharthiya, H., & Tiwari, V. (2018). *Adult Mouse DRG Explant and Dissociated Cell Models to Investigate Neuroplasticity and Responses to Environmental Insults Including Viral Infection*. *January*, 1–8. https://doi.org/10.3791/56757

Gingras, A. C., Abe, K. T., & Raught, B. (2019). Getting to know the neighborhood: using proximity-dependent biotinylation to characterize protein complexes and map organelles. In *Current Opinion in Chemical Biology* (Vol. 48). https://doi.org/10.1016/j.cbpa.2018.10.017

Grindberg, R. V., Yee-Greenbaum, J. L., McConnell, M. J., Novotny, M., O'Shaughnessy, A. L., Lambert, G. M., Arauzo-Bravo, M. J., Lee, J., Fishman, M., Robbins, G. E., Lin, X., Venepally, P., Badger, J. H., Galbraith, D. W., Gage, F. H., & Lasken, R. S. (2013). RNA-sequencing from single nuclei. *Proceedings of the National Academy of Sciences*, *110*(49), 19802–19807. https://doi.org/10.1073/pnas.1319700110

Haeussler, M., Schönig, K., Eckert, H., Eschstruth, A., Mianné, J., Renaud, J. B., Schneider-Maunoury, S., Shkumatava, A., Teboul, L., Kent, J., Joly, J. S., & Concordet, J. P. (2016). Evaluation of off-target and on-target scoring algorithms and integration into the guide RNA selection tool CRISPOR. *Genome Biology*, *17*(1). https://doi.org/10.1186/s13059-016-1012-2

Hobson, B. D., Choi, S. J., Mosharov, E. V., Soni, R. K., Sulzer, D., & Sims, P. A. (2022). Subcellular proteomics of dopamine neurons in the mouse brain. *ELife*, *11*. https://doi.org/10.7554/eLife.70921

Huang, K. M., Leblanc, A. F., Uddin, M. E., Kim, J. Y., Chen, M., Eisenmann, E. D., Gibson, A. A., Li, Y., Hong, K. W., DiGiacomo, D., Xia, S. H., Alberti, P., Chiorazzi, A., Housley, S. N., Cope, T. C., Sprowl, J. A., Wang, J., Loprinzi, C. L., Noonan, A., … Sparreboom, A. (2020). Neuronal uptake transporters contribute to oxaliplatin neurotoxicity in mice. *Journal of Clinical Investigation*, *130*(9). https://doi.org/10.1172/JCI136796

Hughes, C. S., Moggridge, S., Müller, T., Sorensen, P. H., Morin, G. B., & Krijgsveld, J. (2019). Single-pot, solid-phase-enhanced sample preparation for proteomics experiments. *Nature Protocols*, *14*(1). https://doi.org/10.1038/s41596-018-0082-x

Hunter, D. V., Smaila, B. D., Lopes, D. M., Takatoh, J., Denk, F., & Ramer, M. S. (2018). Advillin is expressed in all adult neural crest-derived neurons. *ENeuro*, *5*(5). https://doi.org/10.1523/ENEURO.0077-18.2018

Kannan, M., Lee, S. J., Schwedhelm-Domeyer, N., Nakazawa, T., & Stegmüller, J. (2012). p250GAP Is a Novel Player in the Cdh1-APC/Smurf1 Pathway of Axon Growth Regulation. *PLoS ONE*, *7*(11). https://doi.org/10.1371/journal.pone.0050735

LaCroix-Fralish, M. L., Ledoux, J. B., & Mogil, J. S. (2007). The Pain Genes Database: An interactive web browser of pain-related transgenic knockout studies. *Pain*, *131*(1–2). https://doi.org/10.1016/j.pain.2007.04.041

Lafrenière, R. G., & Rouleau, G. A. (2011). Migraine: Role of the TRESK two-pore potassium channel. *International Journal of Biochemistry and Cell Biology*, *43*(11), 1533–1536. https://doi.org/10.1016/j.biocel.2011.08.002

Langfelder, P., & Horvath, S. (2008). WGCNA: An R package for weighted correlation network analysis. *BMC Bioinformatics*, *9*. https://doi.org/10.1186/1471-2105-9-559

Leskelä, S., Jara, C., Leandro-García, L. J., Martínez, A., García-Donas, J., Hernando, S., Hurtado, A., Vicario, J. C. C., Montero-Conde, C., Landa, I., López-Jiménez, E., Cascón, A., Milne, R. L., Robledo, M., & Rodríguez-Antona, C. (2011). Polymorphisms in cytochromes P450 2C8 and 3A5 are associated with paclitaxel neurotoxicity. *Pharmacogenomics Journal*, *11*(2). https://doi.org/10.1038/tpj.2010.13

Li, Y., Drabison, T., Nepal, M., Ho, R. H., Leblanc, A. F., Gibson, A. A., Jin, Y., Yang, W., Huang, K. M., Uddin, M. E., Chen, M., DiGiacomo, D. F., Chen, X., Razzaq, S., Tonniges, J. R., McTigue, D. M., Mims, A. S., Lustberg, M. B., Wang, Y., ... Hu, S. (2023). Targeting a xenobiotic transporter to ameliorate vincristine-induced sensory neuropathy. *JCI Insight*, *8*(14). https://doi.org/10.1172/jci.insight.164646

Litke, C., Hagenston, A. M., Kenkel, A. K., Paldy, E., Lu, J., Kuner, R., & Mauceri, D. (2022). Organic anion transporter 1 is an HDAC4-regulated mediator of nociceptive hypersensitivity in mice. *Nature Communications*, *13*(1). https://doi.org/10.1038/s41467-022-28357-x

Livni, L., Lees, J. G., Barkl-Luke, M. E., Goldstein, D., & Moalem-Taylor, G. (2019). Dorsal root ganglion explants derived from chemotherapy-treated mice have reduced neurite outgrowth in culture. *Neuroscience Letters*, *694*. https://doi.org/10.1016/j.neulet.2018.11.016

Lopes, D. M., Denk, F., & McMahon, S. B. (2017). The Molecular Fingerprint of Dorsal Root and Trigeminal Ganglion Neurons. *Frontiers in Molecular Neuroscience*. https://doi.org/10.3389/fnmol.2017.00304

Love, M. I., Huber, W., & Anders, S. (2014). Moderated estimation of fold change and dispersion for RNA-seq data with DESeq2. *Genome Biology 2014 15:12*, *15*(12), 1–21. https://doi.org/10.1186/S13059-014-0550-8

Luo, L., Ambrozkiewicz, M. C., Benseler, F., Chen, C., Dumontier, E., Falkner, S., Furlanis, E., Gomez, A. M., Hoshina, N., Huang, W. H., Hutchison, M. A., Itoh-Maruoka, Y., Lavery, L. A., Li, W., Maruo, T., Motohashi, J., Pai, E. L. L., Pelkey, K. A., Pereira, A., ... Craig, A. M. (2020). Optimizing Nervous System-Specific Gene Targeting with Cre Driver Lines: Prevalence of Germline Recombination and Influencing Factors. *Neuron*, *106*(1). https://doi.org/10.1016/j.neuron.2020.01.008

Madisen, L., Zwingman, T. A., Sunkin, S. M., Oh, S. W., Zariwala, H. A., Gu, H., Ng, L. L., Palmiter, R. D., Hawrylycz, M. J., Jones, A. R., Lein, E. S., & Zeng, H. (2010). A robust and high-throughput Cre reporting and characterization system for the whole mouse brain. *Nature Neuroscience*, *13*(1), 133–140. https://doi.org/10.1038/NN.2467

Matzinger, M., Mayer, R. L., & Mechtler, K. (2023). Label-free single cell proteomics utilizing ultrafast LC and MS instrumentation: A valuable complementary technique to multiplexing. In *Proteomics* (Vol. 23, Issues 13–14). John Wiley and Sons Inc. https://doi.org/10.1002/pmic.202200162

May, D. G., Scott, K. L., Campos, A. R., & Roux, K. J. (2020). Comparative Application of BioID

and TurboID for Protein-Proximity Biotinylation. *Cells*, *9*(5). https://doi.org/10.3390/cells9051070

Miao, Y. R., Xia, M., Luo, M., Luo, T., Yang, M., & Guo, A. Y. (2022). ImmuCellAI-mouse: a tool for comprehensive prediction of mouse immune cell abundance and immune microenvironment depiction. *Bioinformatics*, *38*(3). https://doi.org/10.1093/bioinformatics/btab711

Middleton, S. J., Barry, A. M., Comini, M., Li, Y., Ray, P. R., Shiers, S., Themistocleous, A. C., Uhelski, M. L., Yang, X., Dougherty, P. M., Price, T. J., & Bennett, D. L. (2021). Studying human nociceptors: From fundamentals to clinic. *Brain*. https://doi.org/10.1093/brain/awab048

Murata, K., Kinoshita, T., Ishikawa, T., Kuroda, K., Hoshi, M., & Fukazawa, Y. (2020). Region- and neuronal-subtype-specific expression of Na,K-ATPase alpha and beta subunit isoforms in the mouse brain. *Journal of Comparative Neurology*, *528*(16). https://doi.org/10.1002/cne.24924

Nakamura, T., Komiya, M., Sone, K., Hirose, E., Gotoh, N., Morii, H., Ohta, Y., & Mori, N. (2002). Grit, a GTPase-Activating Protein for the Rho Family, Regulates Neurite Extension through Association with the TrkA Receptor and N-Shc and CrkL/Crk Adapter Molecules. *Molecular and Cellular Biology*, *22*(24). https://doi.org/10.1128/mcb.22.24.8721-8734.2002

North, R. Y., Li, Y., Ray, P., Rhines, L. D., Tatsui, C. E., Rao, G., Johansson, C. A., Zhang, H., Kim, Y. H., Zhang, B., Dussor, G., Kim, T. H., Price, T. J., & Dougherty, P. M. (2019). Electrophysiological and transcriptomic correlates of neuropathic pain in human dorsal root ganglion neurons. *Brain : A Journal of Neurology*, *142*(5), 1215–1226. https://doi.org/10.1093/brain/awz063

Perez-Riverol, Y., Bai, J., Bandla, C., García-Seisdedos, D., Hewapathirana, S., Kamatchinathan, S., Kundu, D. J., Prakash, A., Frericks-Zipper, A., Eisenacher, M., Walzer, M., Wang, S., Brazma, A., & Vizcaíno, J. A. (2022). The PRIDE database resources in 2022: A hub for mass spectrometry-based proteomics evidences. *Nucleic Acids Research*, *50*(D1). https://doi.org/10.1093/nar/gkab1038

Qin, W., Cho, K. F., Cavanagh, P. E., & Ting, A. Y. (2021). Deciphering molecular interactions by proximity labeling. In *Nature Methods* (Vol. 18, Issue 2). https://doi.org/10.1038/s41592-020-01010-5

Rasband, M. N., Park, E. W., Vanderah, T. W., Lai, J., Porreca, F., & Trimmer, J. S. (2001). Distinct potassium channels on pain-sensing neurons. *Proceedings of the National Academy of Sciences of the United States of America*, *98*(23). https://doi.org/10.1073/pnas.231376298

Rasband, M. N., & Trimmer, J. S. (2001). Subunit composition and novel localization of K+ channels in spinal cord. *Journal of Comparative Neurology*, *429*(1). https://doi.org/10.1002/1096-9861(20000101)429:1<166::AID-CNE13>3.0.CO;2-Y

Rawat, A., Vu, D. T., Erbacher, C., Stigloher, C., Üçeyler, N., Metousis, A., Mann, M., Briese, M., & Sendtner, M. (2025). Proteomic analysis of isolated nerve terminals from NaV1.9 knockout mice reveals pathways relevant for pain perception. *Pain*, *00*(00), 1–18. https://doi.org/10.1097/j.pain.0000000000003743

Rayaprolu, S., Bitarafan, S., Santiago, J. V., Betarbet, R., Sunna, S., Cheng, L., Xiao, H., Nelson, R. S., Kumar, P., Bagchi, P., Duong, D. M., Goettemoeller, A. M., Oláh, V. J., Rowan, M., Levey, A. I., Wood, L. B., Seyfried, N. T., & Rangaraju, S. (2022). Cell type-specific biotin labeling in vivo resolves regional neuronal and astrocyte proteomic differences in mouse brain. *Nature Communications*, *13*(1). https://doi.org/10.1038/s41467-022-30623-x

Ritchie, M. E., Phipson, B., Wu, D., Hu, Y., Law, C. W., Shi, W., & Smyth, G. K. (2015). Limma powers differential expression analyses for RNA-sequencing and microarray studies. *Nucleic Acids Research*, *43*(7). https://doi.org/10.1093/nar/gkv007

Roux, K. J., Kim, D. I., Raida, M., & Burke, B. (2012). A promiscuous biotin ligase fusion protein identifies proximal and interacting proteins in mammalian cells. *Journal of Cell Biology*, *196*(6). https://doi.org/10.1083/jcb.201112098

Schmidt, D., Díaz, P., Muñoz, D., Espinoza, F., Nystrom, A., Fuentes, I., Ezquer, M., Bennett, D.

L., & Calvo, M. (2022). Characterisation of the pathophysiology of neuropathy and sensory dysfunction in a mouse model of recessive dystrophic epidermolysis bullosa. *Pain*, *163*(10). https://doi.org/10.1097/j.pain.0000000000002599

Schulte, R. R., & Ho, R. H. (2019). Organic anion transporting polypeptides: Emerging roles in cancer pharmacology. In *Molecular Pharmacology* (Vol. 95, Issue 5). https://doi.org/10.1124/mol.118.114314

Segelcke, D., van der Burgt, M., Kappert, C., Schmidt Garcia, D., Sondermann, J. R., Bigalke, S., Pradier, B., Gomez-Varela, D., Zahn, P. K., Schmidt, M., & Pogatzki-Zahn, E. M. (2023). Phenotype- and species-specific skin proteomic signatures for incision-induced pain in humans and mice. *British Journal of Anaesthesia*, *130*(3). https://doi.org/10.1016/j.bja.2022.10.040

Shannon, P., Markiel, A., Ozier, O., Baliga, N. S., Wang, J. T., Ramage, D., Amin, N., Schwikowski, B., & Ideker, T. (2003). Cytoscape: A software Environment for integrated models of biomolecular interaction networks. *Genome Research*, *13*(11). https://doi.org/10.1101/gr.1239303

Sisignano, M., Baron, R., Scholich, K., & Geisslinger, G. (2014). Mechanism-based treatment for chemotherapy-induced peripheral neuropathic pain. In *Nature Reviews Neurology* (Vol. 10, Issue 12). https://doi.org/10.1038/nrneurol.2014.211

Sprowl, J. A., Ciarimboli, G., Lancaster, C. S., Giovinazzo, H., Gibson, A. A., Du, G., Janke, L. J., Cavaletti, G., Shields, A. F., & Sparreboom, A. (2013). Oxaliplatin-induced neurotoxicity is dependent on the organic cation transporter OCT2. *Proceedings of the National Academy of Sciences of the United States of America*, *110*(27). https://doi.org/10.1073/pnas.1305321110

Su, G., Kuchinsky, A., Morris, J. H., States, D. J., & Meng, F. (2010). GLay: Community structure analysis of biological networks. *Bioinformatics*, *26*(24). https://doi.org/10.1093/bioinformatics/btq596

Sun, X., Sun, H., Han, X., Chen, P. C., Jiao, Y., Wu, Z., Zhang, X., Wang, Z., Niu, M., Yu, K., Liu, D., Dey, K. K., Mancieri, A., Fu, Y., Cho, J. H., Li, Y., Poudel, S., Branon, T. C., Ting, A. Y., & Peng, J. (2022). Deep Single-Cell-Type Proteome Profiling of Mouse Brain by Nonsurgical AAV-Mediated Proximity Labeling. *Analytical Chemistry*, *94*(13). https://doi.org/10.1021/acs.analchem.1c05212

Sunna, S., Bowen, C., Zeng, H., Rayaprolu, S., Kumar, P., Bagchi, P., Dammer, E. B., Guo, Q., Duong, D. M., Bitarafan, S., Natu, A., Wood, L., Seyfried, N. T., & Rangaraju, S. (2023). Cellular Proteomic Profiling Using Proximity Labeling by TurboID-NES in Microglial and Neuronal Cell Lines. *Molecular & Cellular Proteomics : MCP*, *22*(6). https://doi.org/10.1016/j.mcpro.2023.100546

Szklarczyk, D., Kirsch, R., Koutrouli, M., Nastou, K., Mehryary, F., Hachilif, R., Gable, A. L., Fang, T., Doncheva, N. T., Pyysalo, S., Bork, P., Jensen, L. J., & Von Mering, C. (2023). The STRING database in 2023: protein-protein association networks and functional enrichment analyses for any sequenced genome of interest. *Nucleic Acids Research*, *51*(1 D). https://doi.org/10.1093/nar/gkac1000

Tavares-Ferreira, D., Shiers, S., Ray, P. R., Wangzhou, A., Jeevakumar, V., Sankaranarayanan, I., Cervantes, A. M., Reese, J. C., Chamessian, A., Copits, B. A., Dougherty, P. M., Gereau, R. W., Burton, M. D., Dussor, G., & Price, T. J. (2022). Spatial transcriptomics of dorsal root ganglia identifies molecular signatures of human nociceptors. *Science Translational Medicine*, *14*(632), eabj8186. https://doi.org/DOI: 10.1126/scitranslmed.abj8186

Tycko, J., Wainberg, M., Marinov, G. K., Ursu, O., Hess, G. T., Ego, B. K., Aradhana, Li, A., Truong, A., Trevino, A. E., Spees, K., Yao, D., Kaplow, I. M., Greenside, P. G., Morgens, D. W., Phanstiel, D. H., Snyder, M. P., Bintu, L., Greenleaf, W. J., ... Bassik, M. C. (2019). Mitigation of off-target toxicity in CRISPR-Cas9 screens for essential non-coding elements. *Nature Communications*, *10*(1). https://doi.org/10.1038/s41467-019-11955-7

Utriainen, M., & Morris, J. H. (2023). clusterMaker2: a major update to clusterMaker, a multi-algorithm clustering app for Cytoscape. *BMC Bioinformatics*, *24*(1).

https://doi.org/10.1186/s12859-023-05225-z

Viola, D., Valerio, L., Molinaro, E., Agate, L., Bottici, V., Biagini, A., Lorusso, L., Cappagli, V., Pieruzzi, L., Giani, C., Sabini, E., Passannati, P., Puleo, L., Matrone, A., Pontillo-Contillo, B., Battaglia, V., Mazzeo, S., Vitti, P., & Elisei, R. (2016). Treatment of advanced thyroid cancer with targeted therapies: Ten years of experience. *Endocrine-Related Cancer*, *23*(4). https://doi.org/10.1530/ERC-15-0555

Wetzel, C., Pifferi, S., Picci, C., Gök, C., Hoffmann, D., Bali, K. K., Lampe, A., Lapatsina, L., Fleischer, R., Smith, E. S. J., Bégay, V., Moroni, M., Estebanez, L., Kühnemund, J., Walcher, J., Specker, E., Neuenschwander, M., Von Kries, J. P., Haucke, V., ... Lewin, G. R. (2017). Small-molecule inhibition of STOML3 oligomerization reverses pathological mechanical hypersensitivity. *Nature Neuroscience*, *20*(2). https://doi.org/10.1038/nn.4454

Wu, T., Hu, E., Xu, S., Chen, M., Guo, P., Dai, Z., Feng, T., Zhou, L., Tang, W., Zhan, L., Fu, X., Liu, S., Bo, X., & Yu, G. (2021). clusterProfiler 4.0: A universal enrichment tool for interpreting omics data. *The Innovation*, *2*(3), 100141. https://doi.org/10.1016/J.XINN.2021.100141

Xian, F., Sondermann, J. R., Varela, D. G., & Schmidt, M. (2022). Deep proteome profiling reveals signatures of age and sex differences in paw skin and sciatic nerve of naïve mice. *ELife*, *11*. https://doi.org/10.7554/eLife.81431

Yang, L., Wang, H., Lu, W., Yang, G., Lin, Z., Chen, R., & Li, H. (2022). Quantitative proteomic analysis of oxaliplatin induced peripheral neurotoxicity. *Journal of Proteomics*, *266*. https://doi.org/10.1016/j.jprot.2022.104682

Zheng, Y., Liu, P., Bai, L., Trimmer, J. S., Bean, B. P., & Ginty, D. D. (2019). Deep Sequencing of Somatosensory Neurons Reveals Molecular Determinants of Intrinsic Physiological Properties. *Neuron*, *103*(4), 598-616.e7. https://doi.org/10.1016/j.neuron.2019.05.039

Zurborg, S., Piszczek, A., Martínez, C., Hublitz, P., Al Banchaabouchi, M., Moreira, P., Perlas, E., & Heppenstall, P. A. (2011). Generation and characterization of an Advillin-Cre driver mouse line. *Molecular Pain*, *7*. https://doi.org/10.1186/1744-8069-7-66

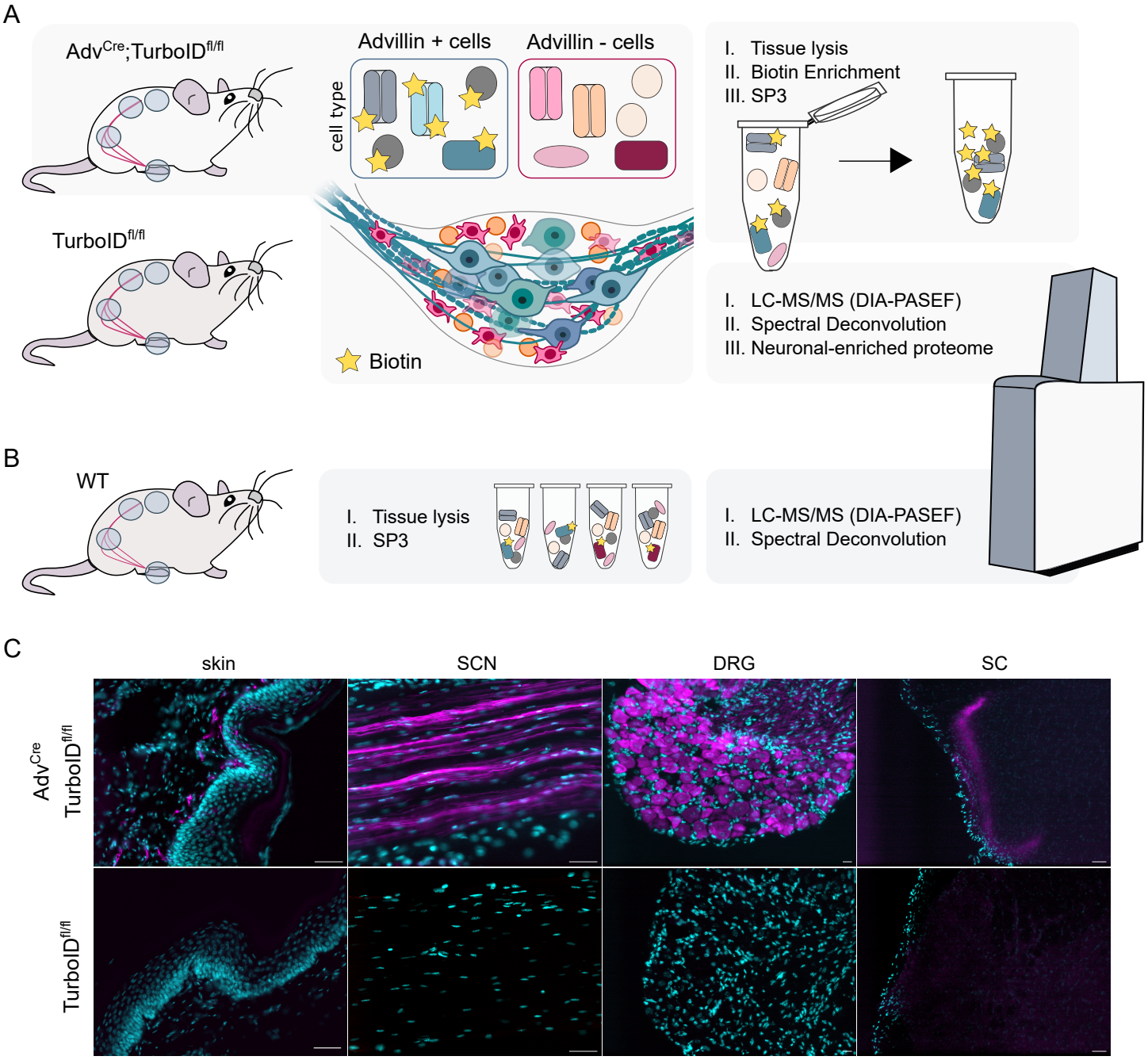
A
Adv^{Cre};TurboID$^{fl/fl}$
TurboID$^{fl/fl}$
Advillin + cells
Advillin - cells
cell type
Biotin
I. Tissue lysis
II. Biotin Enrichment
III. SP3
I. LC-MS/MS (DIA-PASEF)
II. Spectral Deconvolution
III. Neuronal-enriched proteome
B
WT
I. Tissue lysis
II. SP3
I. LC-MS/MS (DIA-PASEF)
II. Spectral Deconvolution
C
skin
SCN
DRG
SC
Adv^{Cre} TurboID$^{fl/fl}$
TurboID$^{fl/fl}$

Fig 1

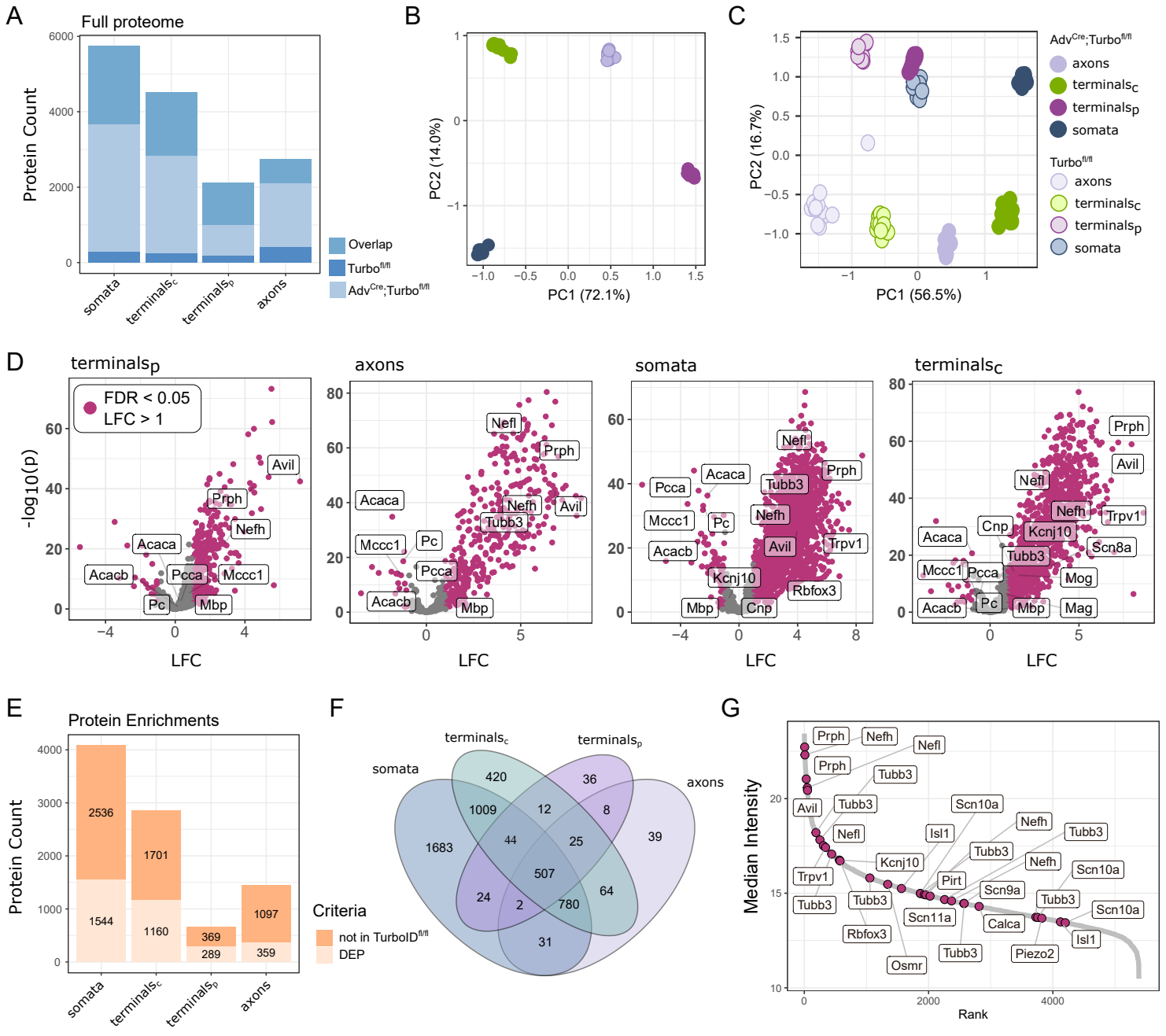
A
Full proteome
Protein Count
6000
4000
2000
0
somata
terminals$_c$
terminals$_p$
axons
Overlap
Turbo$^{fl/fl}$
Adv^{Cre};Turbo$^{fl/fl}$
B
PC2 (14.0%)
PC1 (72.1%)
C
PC2 (16.7%)
PC1 (56.5%)
Adv^{Cre};Turbo$^{fl/fl}$
axons
terminals$_c$
terminals$_p$
somata
Turbo$^{fl/fl}$
axons
terminals$_c$
terminals$_p$
somata
D
terminals$_p$
FDR < 0.05
LFC > 1
-log10(p)
LFC
Avil
Prph
Nefh
Acaca
Acacb
Pcca
Mccc1
Pc
Mbp
axons
Nefl
Prph
Avil
Nefh
Tubb3
Acaca
Mccc1
Pc
Pcca
Acacb
Mbp
somata
Nefl
Prph
Acaca
Pcca
Tubb3
Mccc1
Pc
Nefh
Acacb
Avil
Trpv1
Kcnj10
Rbfox3
Mbp
Cnp
terminals$_c$
Prph
Avil
Nefl
Nefh
Trpv1
Cnp
Kcnj10
Acaca
Scn8a
Tubb3
Mccc1
Pcca
Mog
Acacb
Pc
Mbp
Mag
E
Protein Enrichments
Protein Count
2536
1544
1701
1160
369
289
1097
359
somata
terminals$_c$
terminals$_p$
axons
F
terminals$_c$
terminals$_p$
somata
axons
420
36
1009
12
8
1683
44
25
39
507
64
24
2
780
31
Criteria
not in TurboID$^{fl/fl}$
DEP
G
Median Intensity
Rank
Prph
Nefh
Nefl
Prph
Tubb3
Avil
Tubb3
Scn10a
Nefl
Isl1
Nefh
Tubb3
Tubb3
Kcnj10
Nefh
Trpv1
Pirt
Scn10a
Scn9a
Tubb3
Tubb3
Tubb3
Scn10a
Scn11a
Calca
Rbfox3
Isl1
Tubb3
Piezo2
Osmr

Fig 2

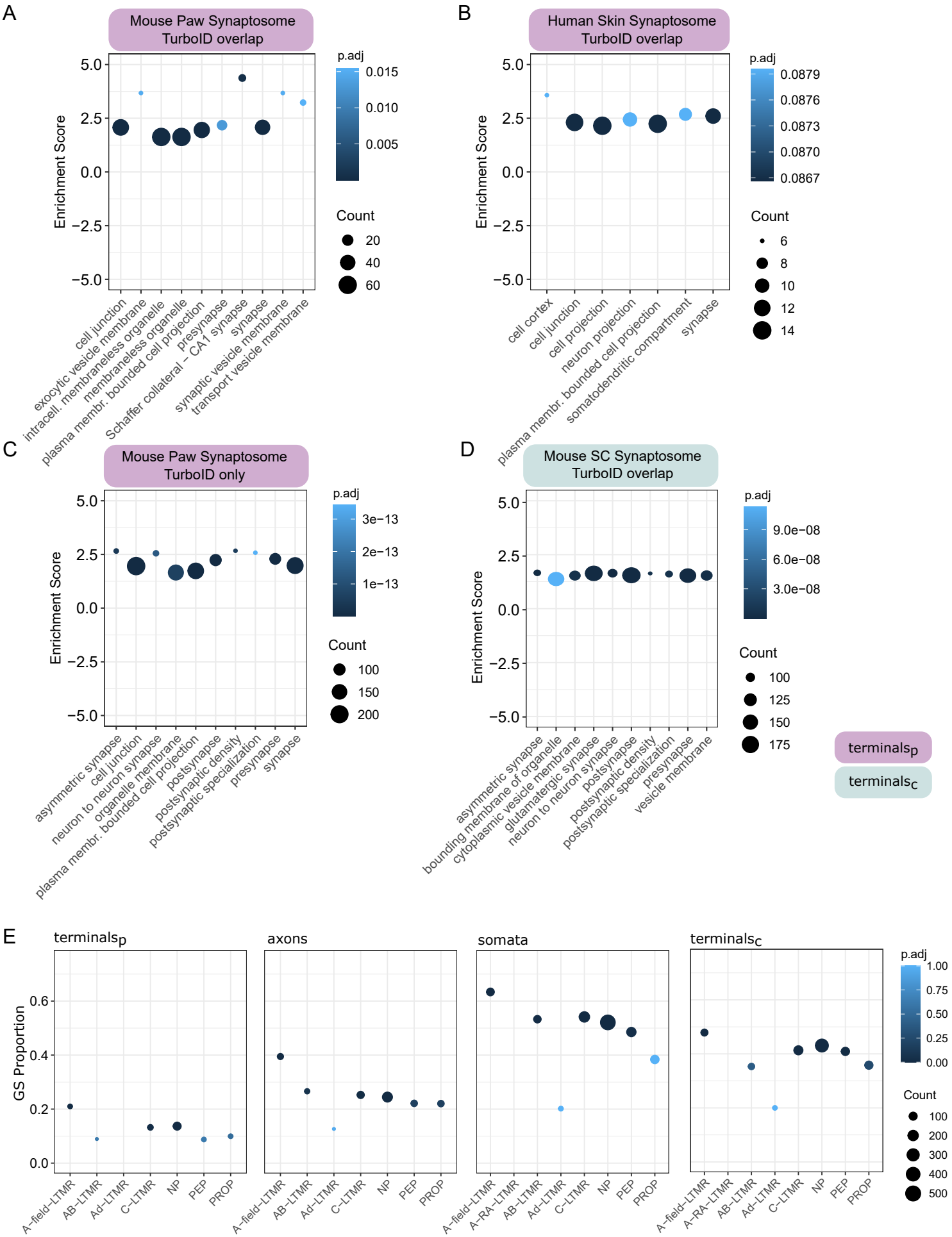
A
Mouse Paw Synaptosome TurboID overlap
Enrichment Score
5.0
2.5
0.0
−2.5
−5.0
cell junction
exocytic vesicle membrane
intracell. membraneless organelle
membraneless organelle
plasma membr. bounded cell projection
presynapse
Schaffer collateral – CA1 synapse
synapse
synaptic vesicle membrane
transport vesicle membrane
p.adj
0.015
0.010
0.005
Count
20
40
60
B
Human Skin Synaptosome TurboID overlap
Enrichment Score
cell cortex
cell junction
cell projection
neuron projection
plasma membr. bounded cell projection
somatodendritic compartment
synapse
p.adj
0.0879
0.0876
0.0873
0.0870
0.0867
Count
6
8
10
12
14
C
Mouse Paw Synaptosome TurboID only
Enrichment Score
asymmetric synapse
cell junction
neuron to neuron synapse
organelle membrane
plasma membr. bounded cell projection
postsynaptic density
postsynaptic specialization
presynapse
synapse
p.adj
3e−13
2e−13
1e−13
Count
100
150
200
D
Mouse SC Synaptosome TurboID overlap
Enrichment Score
asymmetric synapse
bounding membrane of organelle
cytoplasmic vesicle membrane
glutamatergic synapse
neuron to neuron synapse
postsynaptic density
postsynaptic specialization
presynapse
vesicle membrane
p.adj
9.0e−08
6.0e−08
3.0e−08
Count
100
125
150
175
terminals$_P$
terminals$_C$
E
terminals$_P$
axons
somata
terminals$_C$
GS Proportion
0.6
0.4
0.2
0.0
A-field-LTMR
AB-LTMR
Ad-LTMR
C-LTMR
NP
PEP
PROP
A-RA-LTMR
p.adj
1.00
0.75
0.50
0.25
0.00
Count
100
200
300
400
500

Fig 3

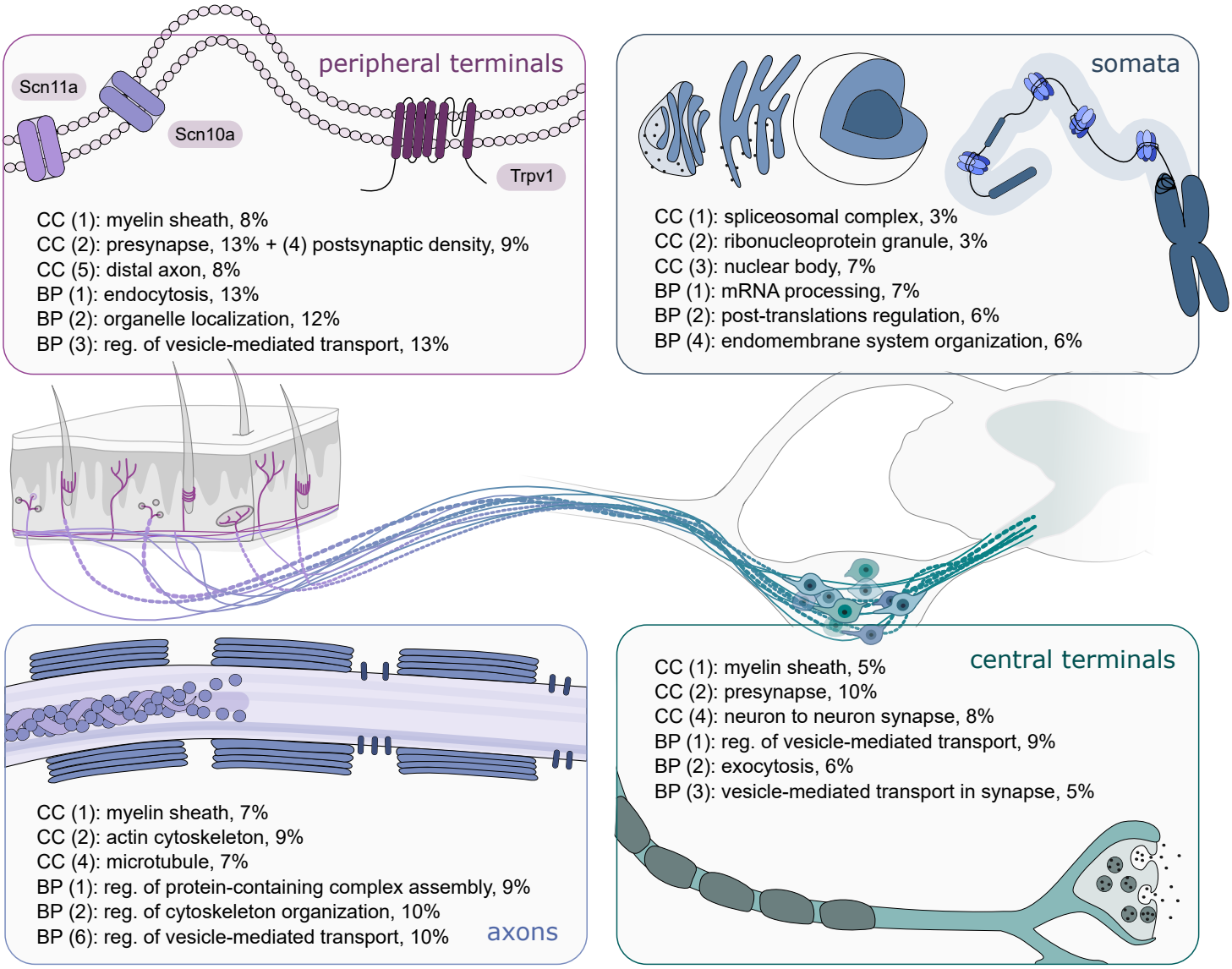
peripheral terminals
Scn11a
Scn10a
Trpv1
CC (1): myelin sheath, 8%
CC (2): presynapse, 13% + (4) postsynaptic density, 9%
CC (5): distal axon, 8%
BP (1): endocytosis, 13%
BP (2): organelle localization, 12%
BP (3): reg. of vesicle-mediated transport, 13%
somata
CC (1): spliceosomal complex, 3%
CC (2): ribonucleoprotein granule, 3%
CC (3): nuclear body, 7%
BP (1): mRNA processing, 7%
BP (2): post-translations regulation, 6%
BP (4): endomembrane system organization, 6%
CC (1): myelin sheath, 7%
CC (2): actin cytoskeleton, 9%
CC (4): microtubule, 7%
BP (1): reg. of protein-containing complex assembly, 9%
BP (2): reg. of cytoskeleton organization, 10%
BP (6): reg. of vesicle-mediated transport, 10%
axons
central terminals
CC (1): myelin sheath, 5%
CC (2): presynapse, 10%
CC (4): neuron to neuron synapse, 8%
BP (1): reg. of vesicle-mediated transport, 9%
BP (2): exocytosis, 6%
BP (3): vesicle-mediated transport in synapse, 5%

Fig 4

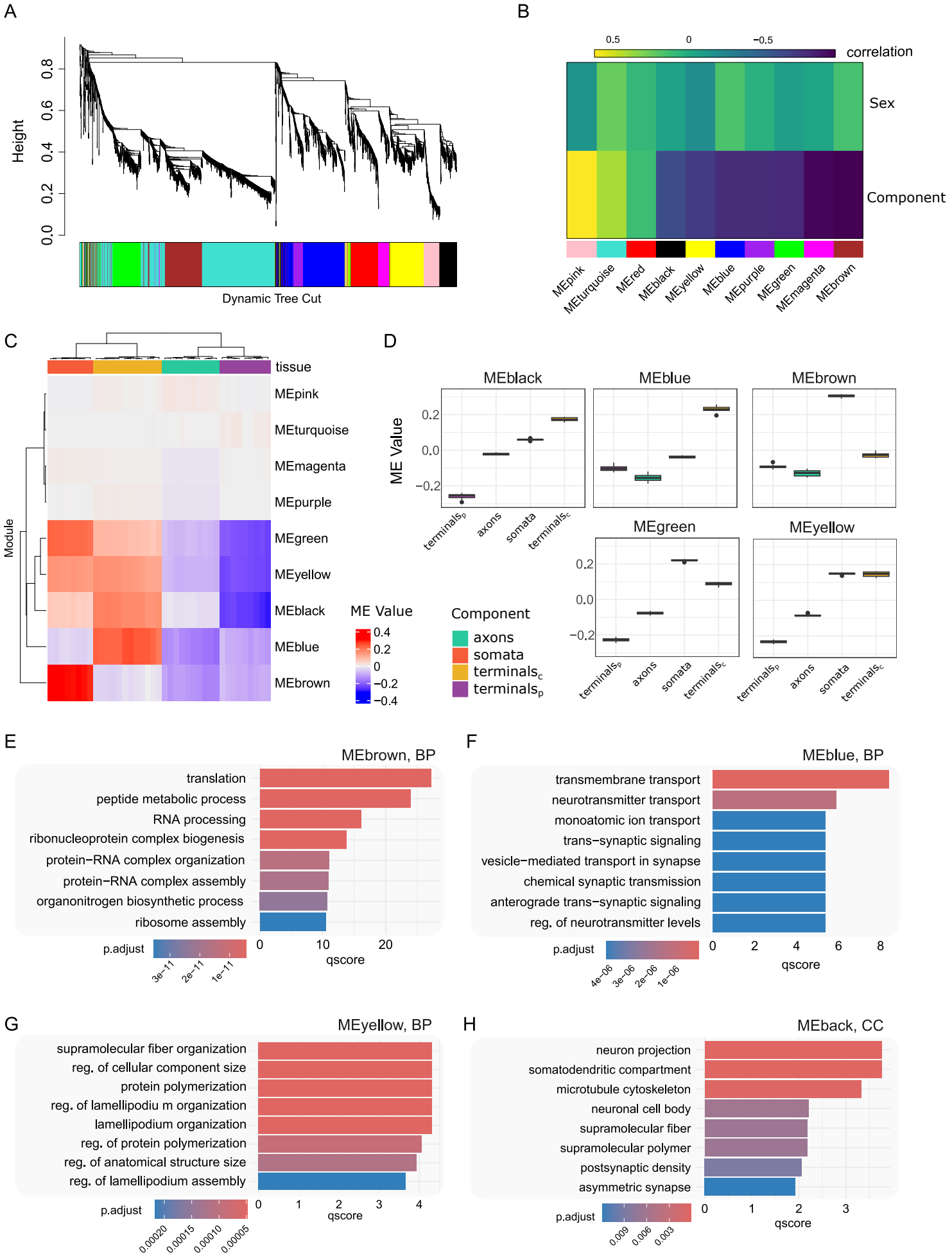
A
Height
0.0
0.2
0.4
0.6
0.8
Dynamic Tree Cut
B
0.5
0
−0.5
correlation
Sex
Component
MEpink
MEturquoise
MEred
MEblack
MEyellow
MEblue
MEpurple
MEgreen
MEmagenta
MEbrown
C
tissue
MEpink
MEturquoise
MEmagenta
MEpurple
MEgreen
MEyellow
MEblack
MEblue
MEbrown
Module
ME Value
0.4
0.2
0
−0.2
−0.4
D
MEblack
MEblue
MEbrown
MEgreen
MEyellow
ME Value
0.2
0.0
−0.2
terminals$_p$
axons
somata
terminals$_c$
Component
axons
somata
terminals$_c$
terminals$_p$
E
MEbrown, BP
translation
peptide metabolic process
RNA processing
ribonucleoprotein complex biogenesis
protein−RNA complex organization
protein−RNA complex assembly
organonitrogen biosynthetic process
ribosome assembly
p.adjust
3e−11
2e−11
1e−11
0
10
20
qscore
F
MEblue, BP
transmembrane transport
neurotransmitter transport
monoatomic ion transport
trans−synaptic signaling
vesicle−mediated transport in synapse
chemical synaptic transmission
anterograde trans−synaptic signaling
reg. of neurotransmitter levels
p.adjust
4e−06
3e−06
2e−06
1e−06
0
2
4
6
8
qscore
G
MEyellow, BP
supramolecular fiber organization
reg. of cellular component size
protein polymerization
reg. of lamellipodiu m organization
lamellipodium organization
reg. of protein polymerization
reg. of anatomical structure size
reg. of lamellipodium assembly
p.adjust
0.00020
0.00015
0.00010
0.00005
0
1
2
3
4
qscore
H
MEback, CC
neuron projection
somatodendritic compartment
microtubule cytoskeleton
neuronal cell body
supramolecular fiber
supramolecular polymer
postsynaptic density
asymmetric synapse
p.adjust
0.009
0.006
0.003
0
1
2
3
qscore

Fig 5

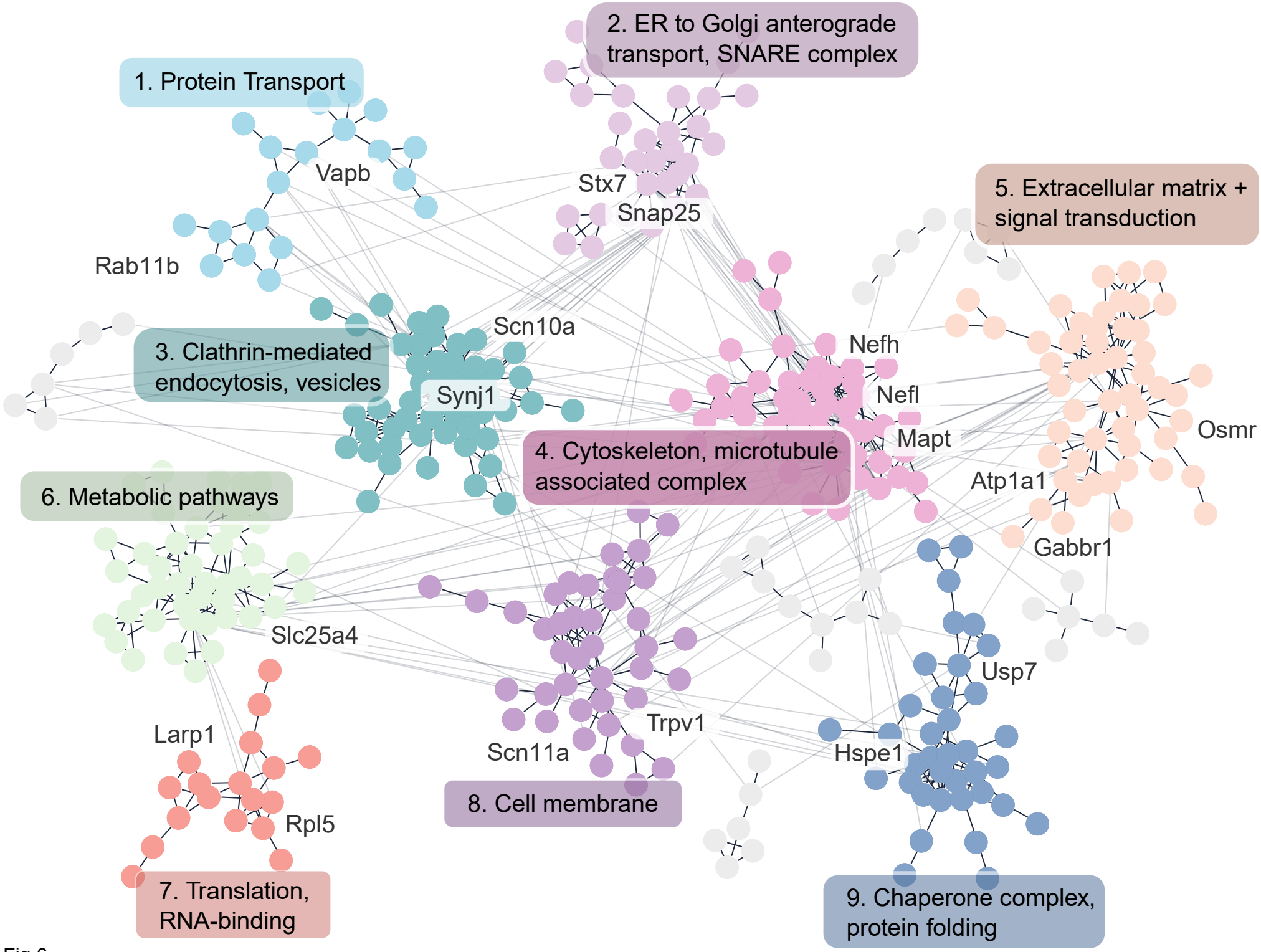
1. Protein Transport
2. ER to Golgi anterograde transport, SNARE complex
3. Clathrin-mediated endocytosis, vesicles
4. Cytoskeleton, microtubule associated complex
5. Extracellular matrix + signal transduction
6. Metabolic pathways
7. Translation, RNA-binding
8. Cell membrane
9. Chaperone complex, protein folding
Vapb
Rab11b
Stx7
Snap25
Scn10a
Synj1
Nefh
Nefl
Mapt
Osmr
Atp1a1
Gabbr1
Slc25a4
Usp7
Trpv1
Scn11a
Hspe1
Larp1
Rpl5

Fig 6

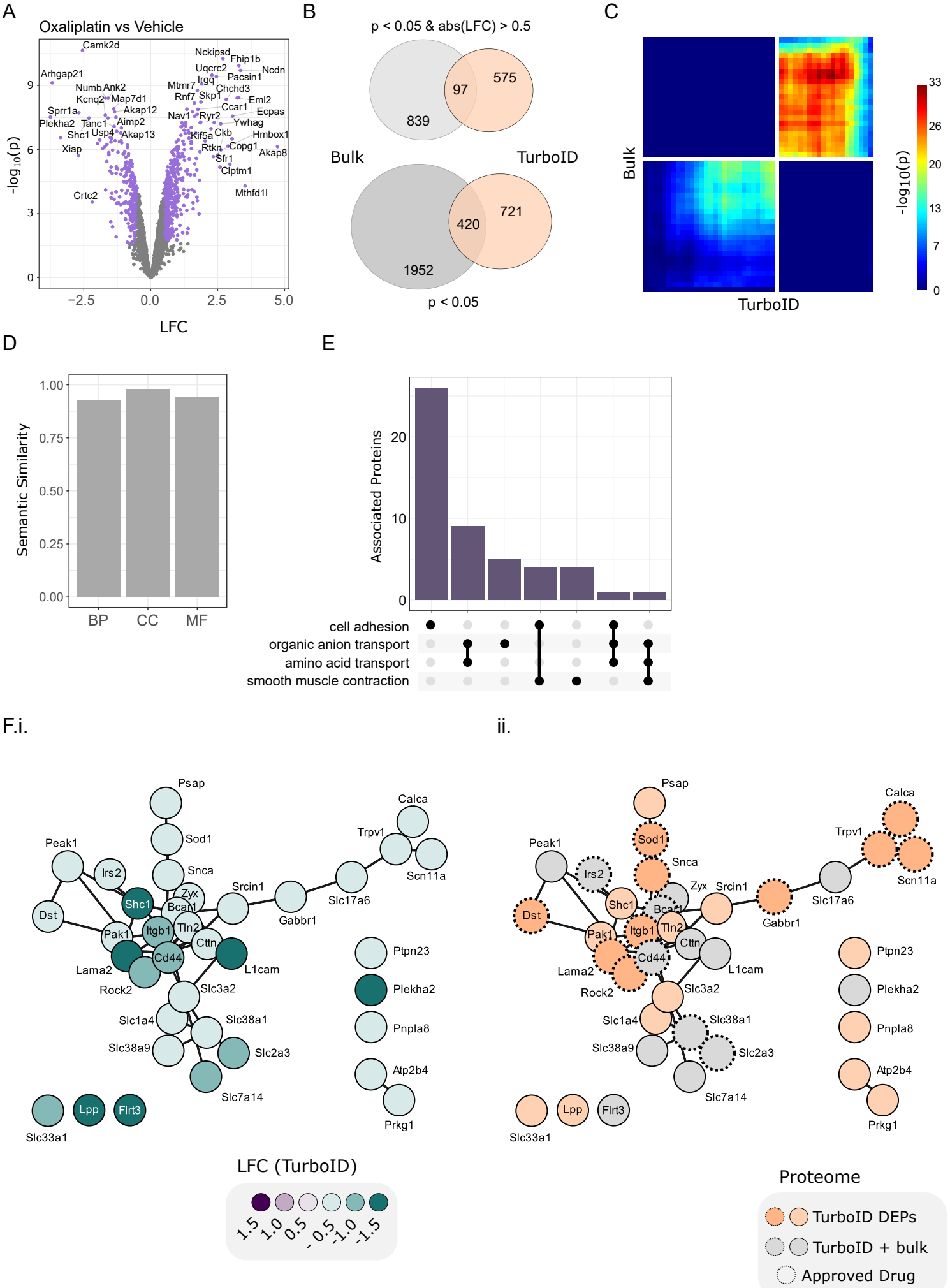
A
Oxaliplatin vs Vehicle
Camk2d
Nckipsd
Fhip1b
Uqcrc2
Ncdn
Arhgap21
Irgq
Pacsin1
Numb
Ank2
Mtmr7
Chchd3
Kcnq2
Map7d1
Rnf7
Skp1
Eml2
Sprr1a
Akap12
Ccar1
Ecpas
Plekha2
Tanc1
Aimp2
Nav1
Ryr2
Ywhag
Shc1
Usp4
Akap13
Kif5a
Ckb
Hmbox1
Xiap
Rtkn
Copg1
Akap8
Sfr1
Clptm1
Crtc2
Mthfd1l
-log10(p)
LFC
B
p < 0.05 & abs(LFC) > 0.5
97
575
839
Bulk
TurboID
420
721
1952
p < 0.05
C
Bulk
TurboID
-log10(p)
D
Semantic Similarity
BP
CC
MF
E
Associated Proteins
cell adhesion
organic anion transport
amino acid transport
smooth muscle contraction
F.i.
ii.
Psap
Calca
Sod1
Trpv1
Peak1
Irs2
Snca
Scn11a
Zyx
Srcin1
Shc1
Bcar1
Slc17a6
Dst
Gabbr1
Pak1
Itgb1
Tln2
Cttn
Cd44
L1cam
Lama2
Rock2
Slc3a2
Slc1a4
Slc38a1
Slc38a9
Slc2a3
Slc7a14
Ptpn23
Plekha2
Pnpla8
Atp2b4
Prkg1
Lpp
Flrt3
Slc33a1
LFC (TurboID)
1.5
1.0
0.5
-0.5
-1.0
-1.5
Proteome
TurboID DEPs
TurboID + bulk
Approved Drug

Fig 7

A

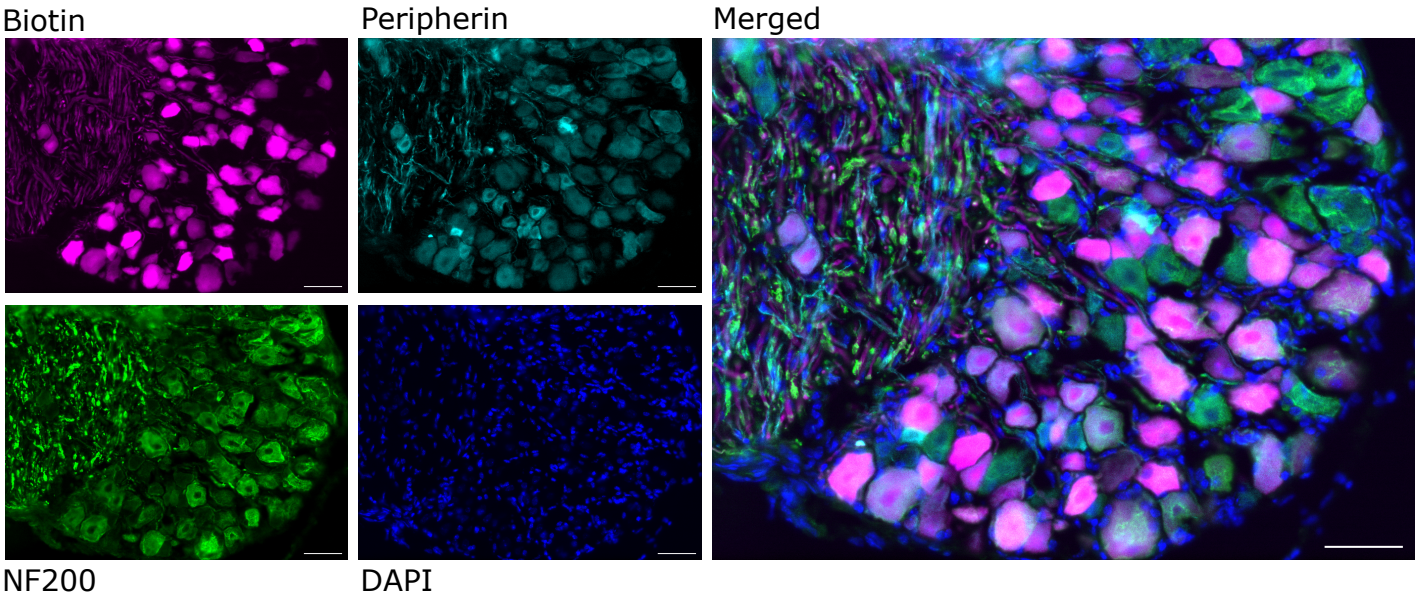
Biotin
Peripherin
Merged
NF200
DAPI

B

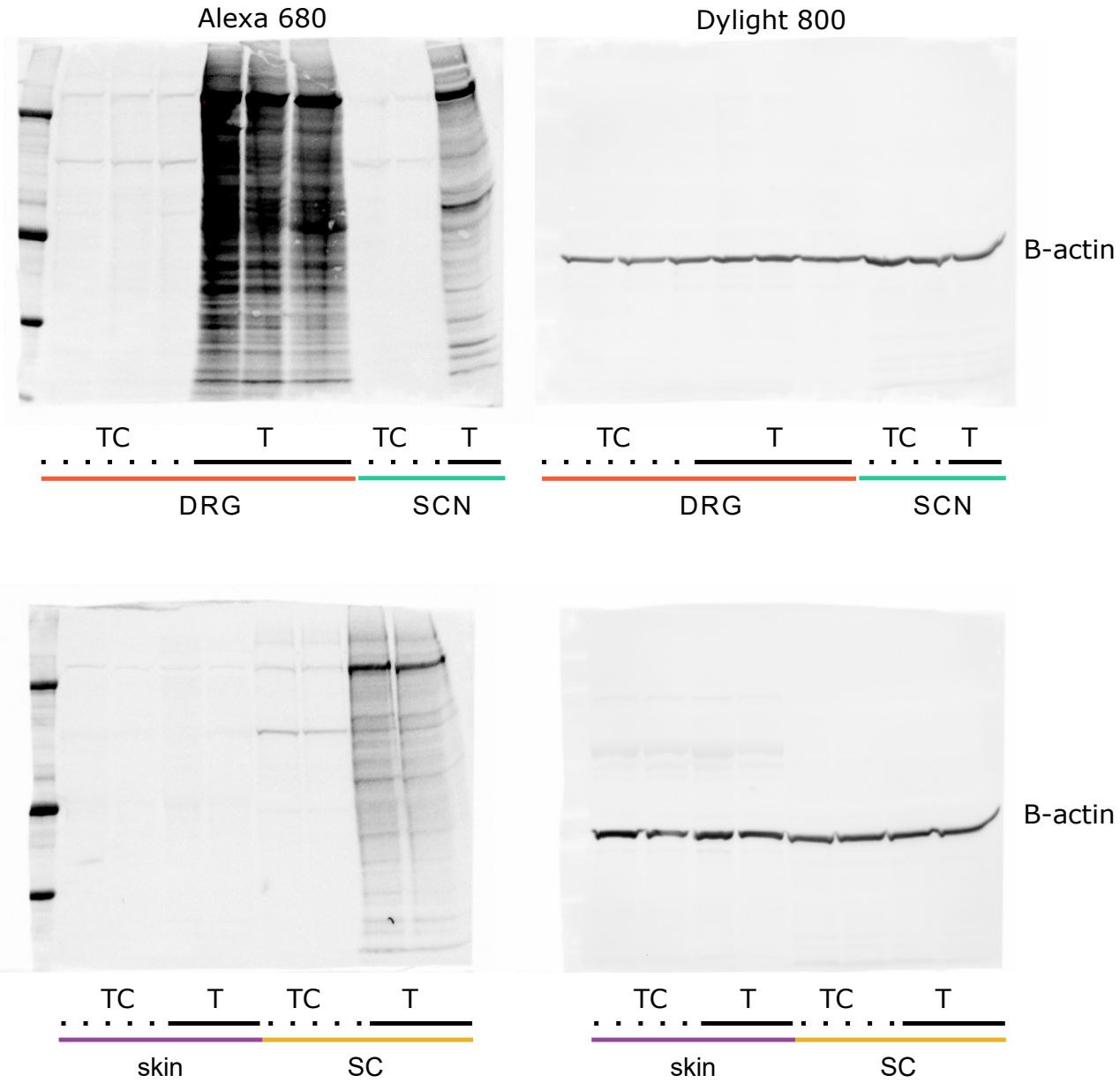
Alexa 680
Dylight 800
B-actin
TC
T
TC
T
DRG
SCN
TC
T
TC
T
DRG
SCN
B-actin
TC
T
TC
T
skin
SC
TC
T
TC
T
skin
SC

SFig 1

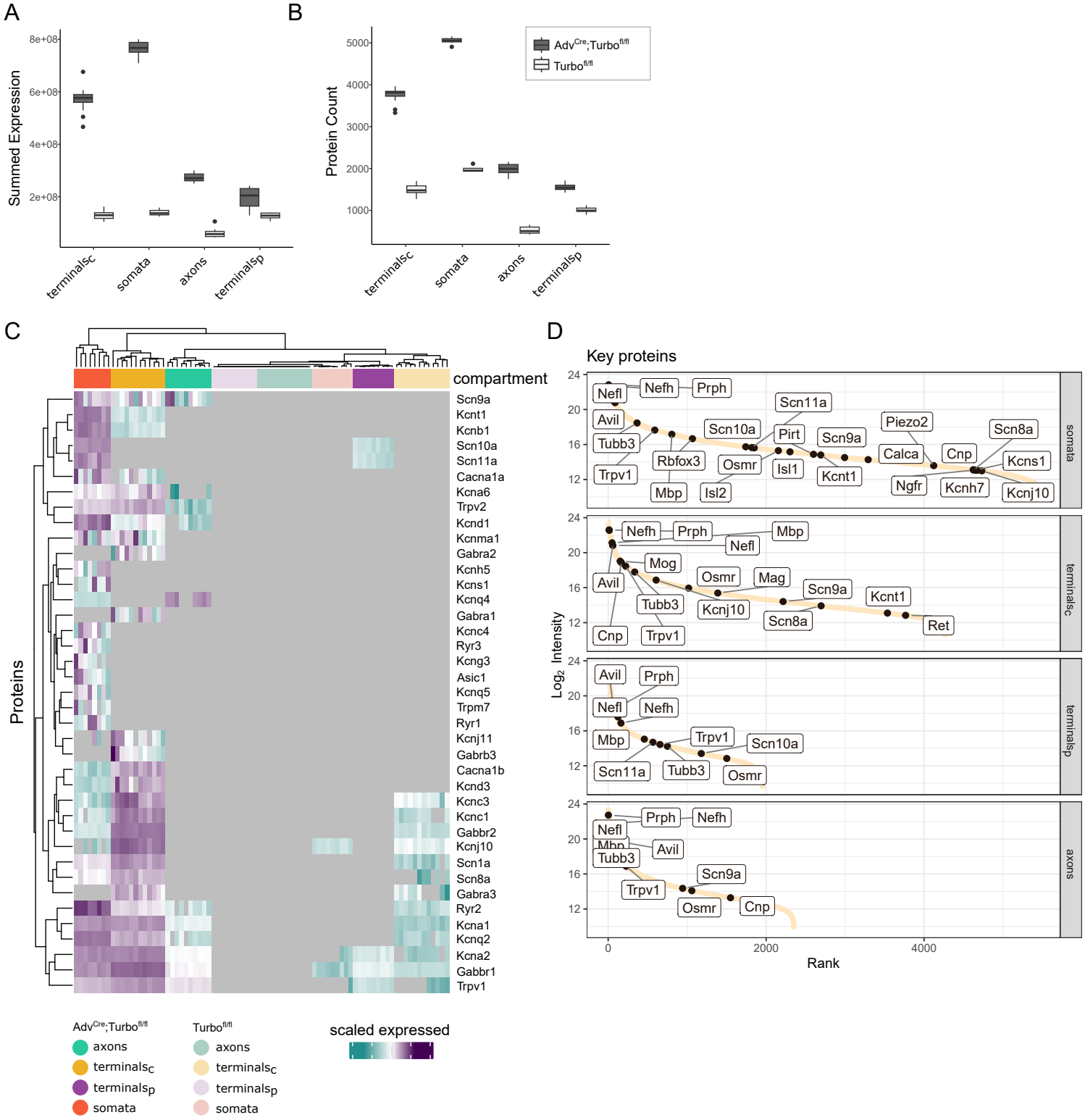
A
Summed Expression
8e+08
6e+08
4e+08
2e+08
terminalsc
somata
axons
terminalsp
B
Protein Count
5000
4000
3000
2000
1000
Adv^Cre;Turbo^fl/fl
Turbo^fl/fl
C
compartment
Proteins
Scn9a
Kcnt1
Kcnb1
Scn10a
Scn11a
Cacna1a
Kcna6
Trpv2
Kcnd1
Kcnma1
Gabra2
Kcnh5
Kcns1
Kcnq4
Gabra1
Kcnc4
Ryr3
Kcng3
Asic1
Kcnq5
Trpm7
Ryr1
Kcnj11
Gabrb3
Cacna1b
Kcnd3
Kcnc3
Kcnc1
Gabbr2
Kcnj10
Scn1a
Scn8a
Gabra3
Ryr2
Kcna1
Kcnq2
Kcna2
Gabbr1
Trpv1
Adv^Cre;Turbo^fl/fl
axons
terminalsc
terminalsp
somata
Turbo^fl/fl
axons
terminalsc
terminalsp
somata
scaled expressed
D
Key proteins
Log2 Intensity
Rank
0
2000
4000
somata
terminalsc
terminalsp
axons
Nefl
Nefh
Prph
Avil
Tubb3
Trpv1
Rbfox3
Mbp
Scn10a
Osmr
Isl2
Scn11a
Pirt
Isl1
Scn9a
Kcnt1
Piezo2
Calca
Ngfr
Cnp
Kcnh7
Scn8a
Kcns1
Kcnj10
Mog
Mag
Ret
Scn11a

SFig 2

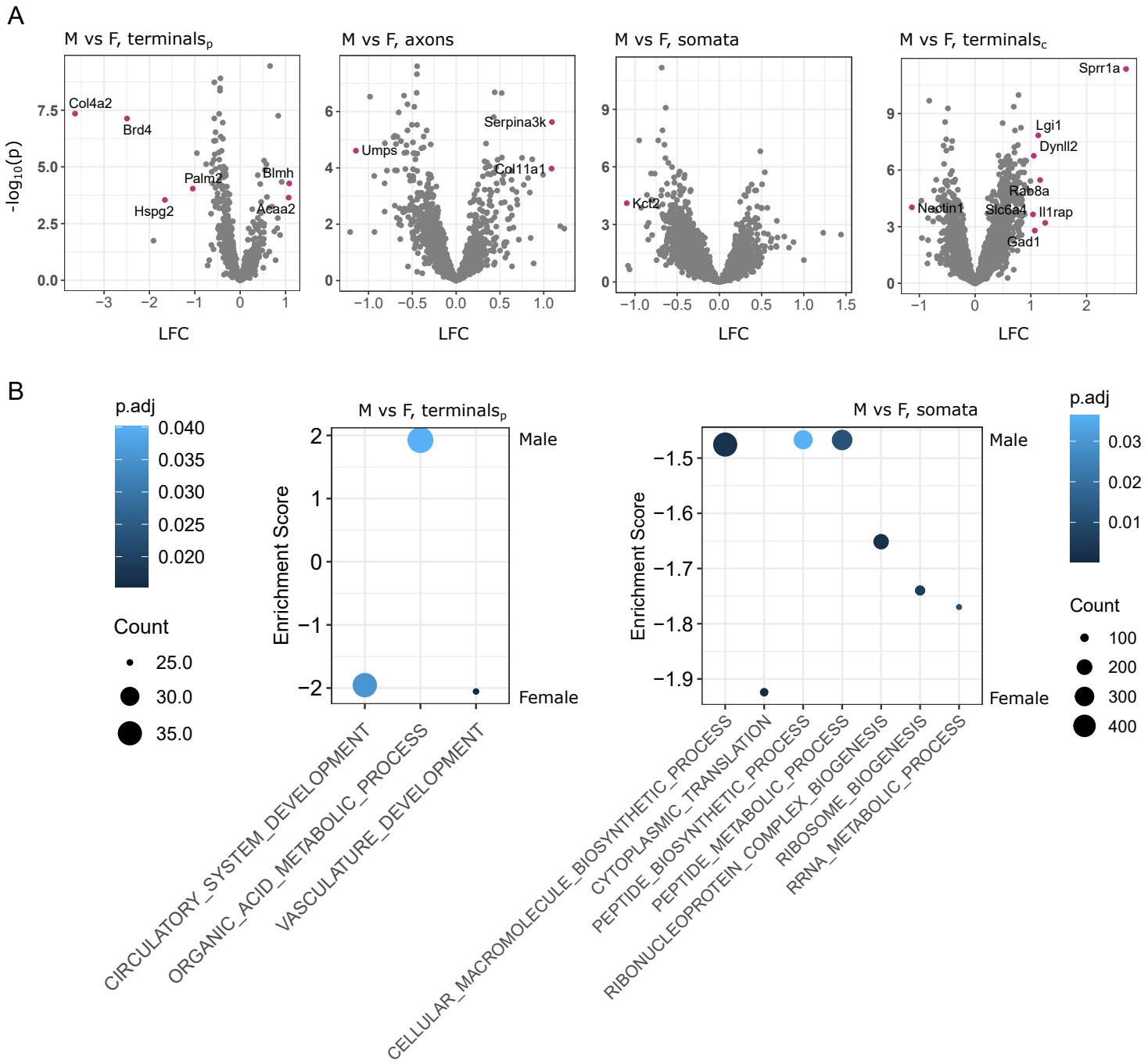
A
M vs F, terminals$_p$
M vs F, axons
M vs F, somata
M vs F, terminals$_c$
-log$_{10}$(p)
LFC
Col4a2
Brd4
Palm2
Blmh
Hspg2
Acaa2
Umps
Serpina3k
Col11a1
Kct2
Sprr1a
Lgi1
Dynll2
Rab8a
Nectin1
Slc6a4
Il1rap
Gad1
B
p.adj
0.040
0.035
0.030
0.025
0.020
Count
25.0
30.0
35.0
M vs F, terminals$_p$
M vs F, somata
Enrichment Score
Male
Female
0.03
0.02
0.01
100
200
300
400
CIRCULATORY_SYSTEM_DEVELOPMENT
ORGANIC_ACID_METABOLIC_PROCESS
VASCULATURE_DEVELOPMENT
CELLULAR_MACROMOLECULE_BIOSYNTHETIC_PROCESS
CYTOPLASMIC_TRANSLATION
PEPTIDE_BIOSYNTHETIC_PROCESS
PEPTIDE_METABOLIC_PROCESS
RIBONUCLEOPROTEIN_COMPLEX_BIOGENESIS
RIBOSOME_BIOGENESIS
RRNA_METABOLIC_PROCESS

SFig 3

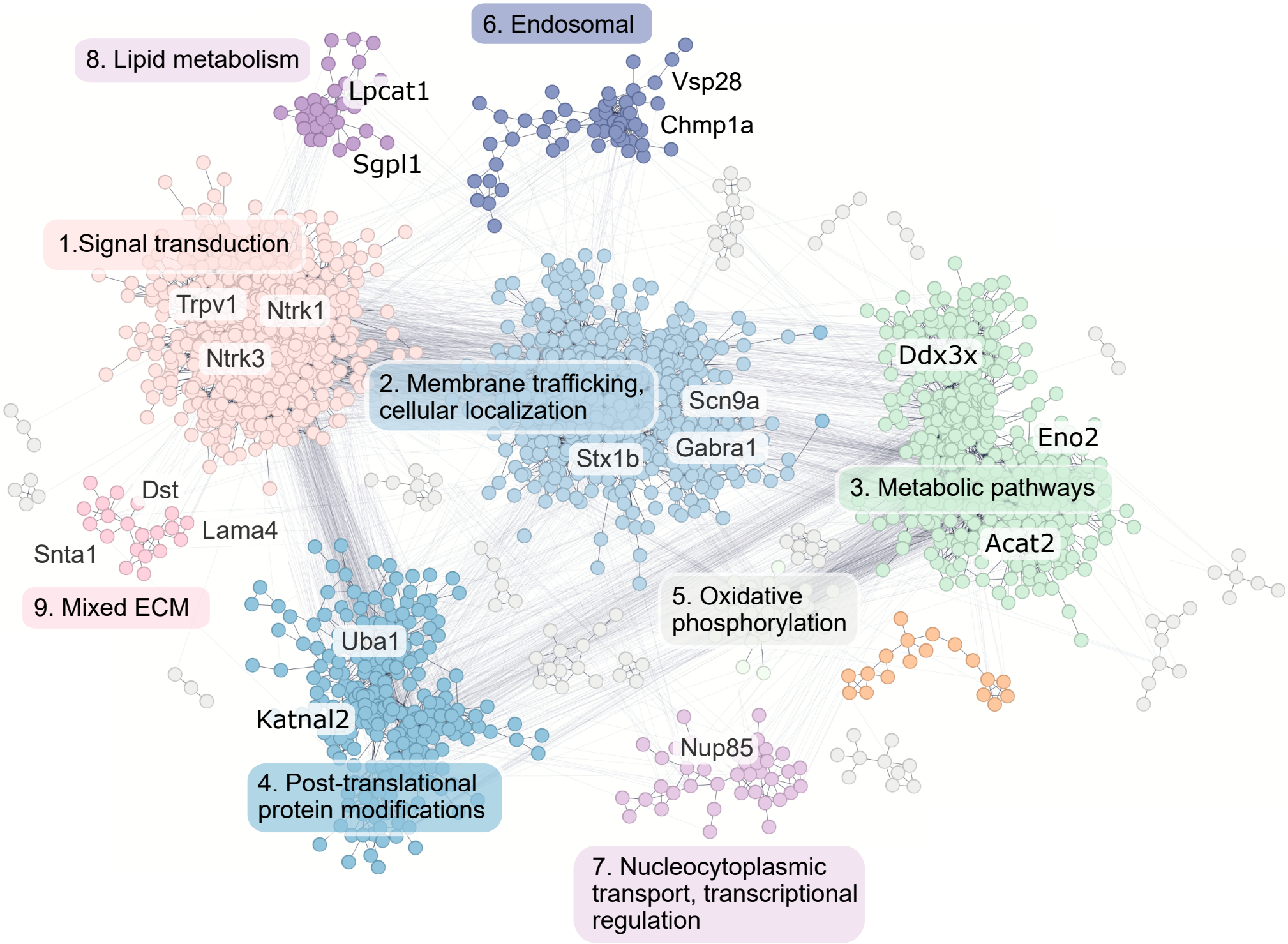
6. Endosomal
8. Lipid metabolism
Lpcat1
Vsp28
Chmp1a
Sgpl1
1.Signal transduction
Trpv1
Ntrk1
Ntrk3
2. Membrane trafficking, cellular localization
Scn9a
Ddx3x
Eno2
Gabra1
Stx1b
3. Metabolic pathways
Dst
Lama4
Snta1
Acat2
9. Mixed ECM
5. Oxidative phosphorylation
Uba1
Katnal2
Nup85
4. Post-translational protein modifications
7. Nucleocytoplasmic transport, transcriptional regulation

SFig 4

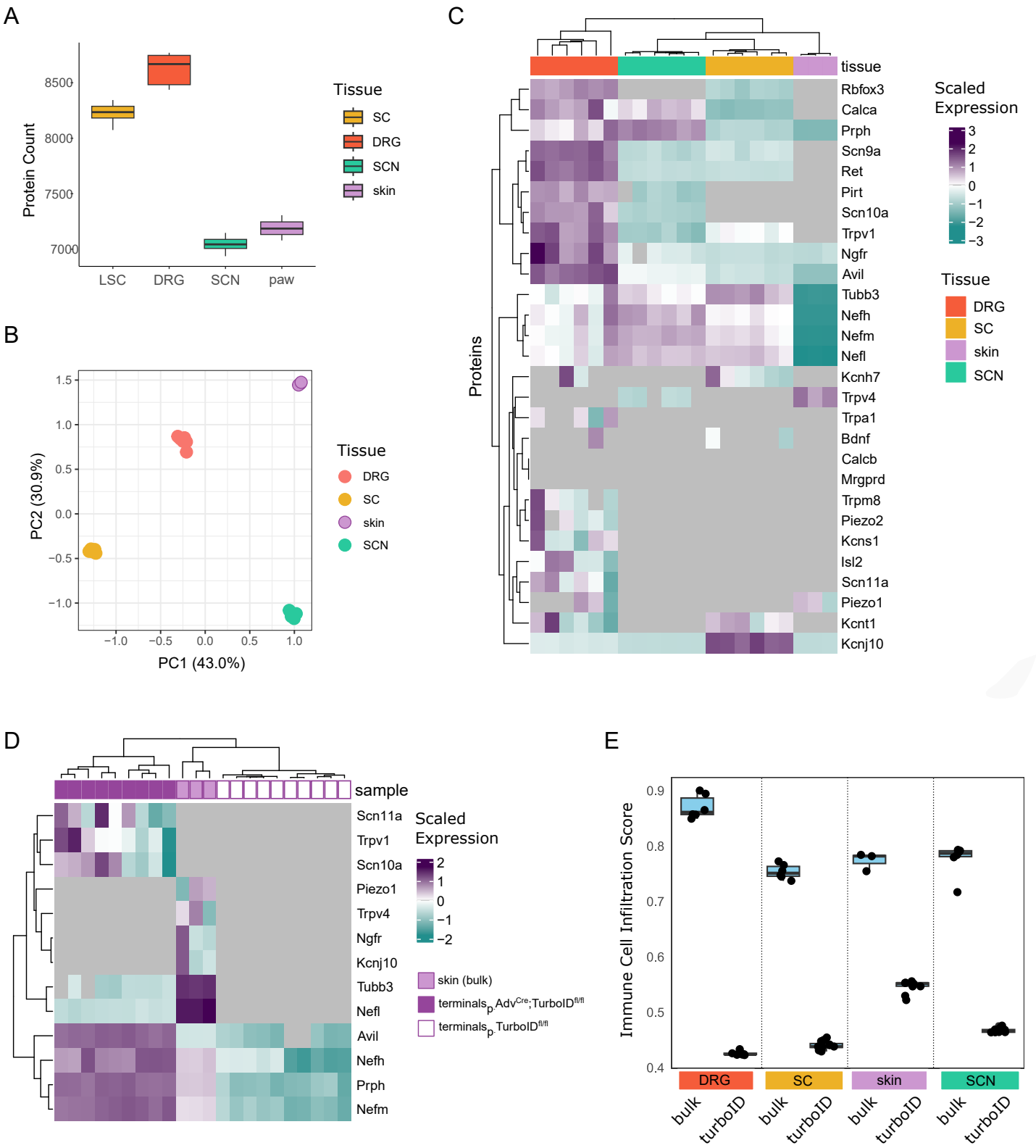
A
Protein Count
8500
8000
7500
7000
LSC
DRG
SCN
paw
Tissue
SC
DRG
SCN
skin
B
PC2 (30.9%)
PC1 (43.0%)
1.5
1.0
0.5
0.0
−0.5
−1.0
Tissue
DRG
SC
skin
SCN
C
tissue
Proteins
Rbfox3
Calca
Prph
Scn9a
Ret
Pirt
Scn10a
Trpv1
Ngfr
Avil
Tubb3
Nefh
Nefm
Nefl
Kcnh7
Trpv4
Trpa1
Bdnf
Calcb
Mrgprd
Trpm8
Piezo2
Kcns1
Isl2
Scn11a
Piezo1
Kcnt1
Kcnj10
Scaled Expression
3
2
1
0
−1
−2
−3
Tissue
DRG
SC
skin
SCN
D
sample
Scn11a
Trpv1
Scn10a
Piezo1
Trpv4
Ngfr
Kcnj10
Tubb3
Nefl
Avil
Nefh
Prph
Nefm
Scaled Expression
2
1
0
−1
−2
skin (bulk)
terminals$_p$Adv^{Cre};TurboID$^{fl/fl}$
terminals$_p$TurboID$^{fl/fl}$
E
Immune Cell Infiltration Score
0.9
0.8
0.7
0.6
0.5
0.4
DRG
SC
skin
SCN
bulk
turboID
bulk
turboID
bulk
turboID
bulk
turboID

SFig 5

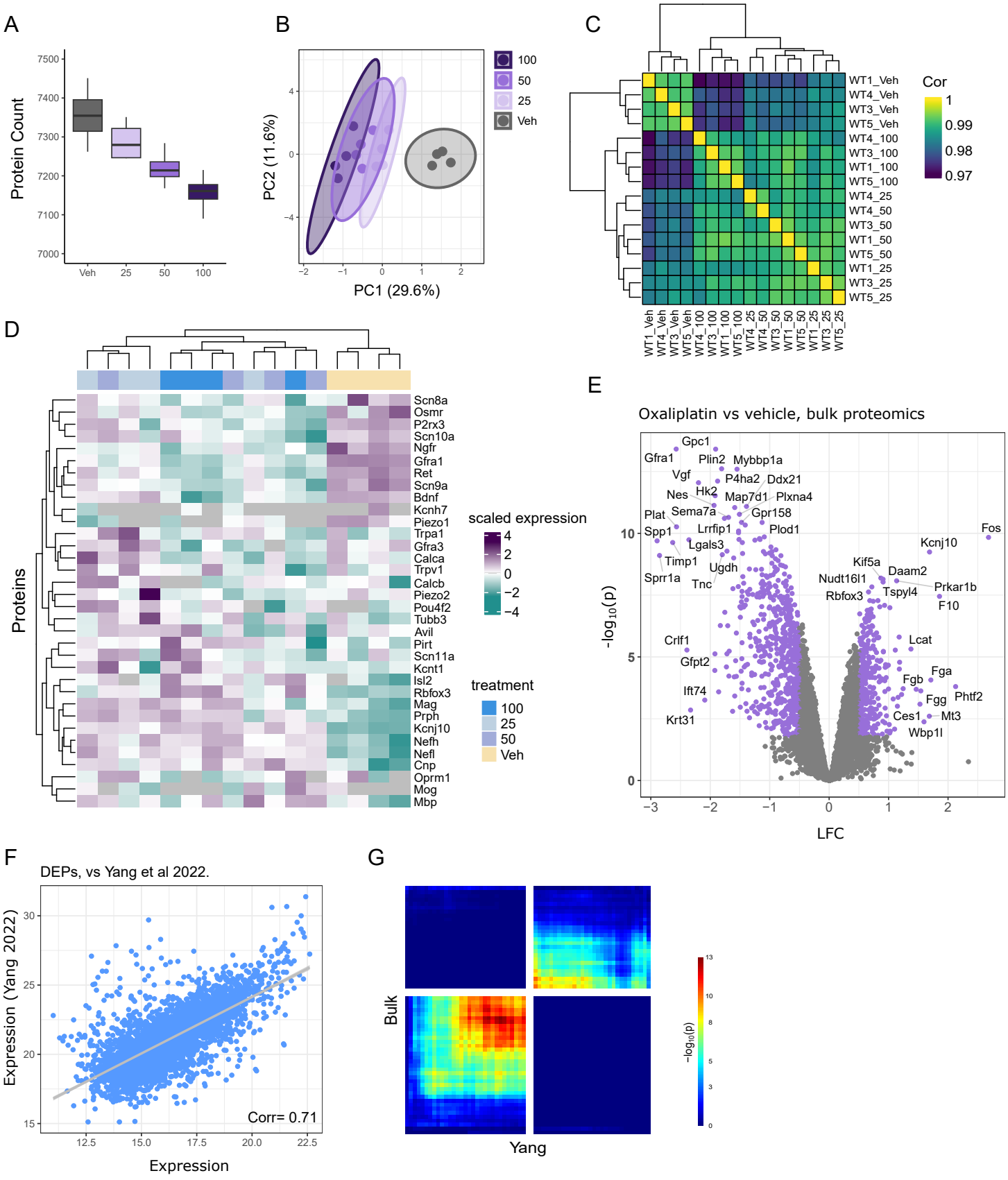
A
Protein Count
7500
7400
7300
7200
7100
7000
Veh
25
50
100
B
PC2 (11.6%)
PC1 (29.6%)
100
50
25
Veh
C
Cor
1
0.99
0.98
0.97
WT1_Veh
WT4_Veh
WT3_Veh
WT5_Veh
WT4_100
WT3_100
WT1_100
WT5_100
WT4_25
WT4_50
WT3_50
WT1_50
WT5_50
WT1_25
WT3_25
WT5_25
D
Proteins
Scn8a
Osmr
P2rx3
Scn10a
Ngfr
Gfra1
Ret
Scn9a
Bdnf
Kcnh7
Piezo1
Trpa1
Gfra3
Calca
Trpv1
Calcb
Piezo2
Pou4f2
Tubb3
Avil
Pirt
Scn11a
Kcnt1
Isl2
Rbfox3
Mag
Prph
Kcnj10
Nefh
Nefl
Cnp
Oprm1
Mog
Mbp
scaled expression
treatment
100
25
50
Veh
E
Oxaliplatin vs vehicle, bulk proteomics
-log10(p)
LFC
Gpc1
Gfra1
Plin2
Mybbp1a
Vgf
P4ha2
Ddx21
Nes
Hk2
Map7d1
Plxna4
Plat
Sema7a
Gpr158
Spp1
Lrrfip1
Plod1
Fos
Kcnj10
Lgals3
Timp1
Ugdh
Kif5a
Daam2
Sprr1a
Tnc
Nudt16l1
Prkar1b
Rbfox3
Tspyl4
F10
Crlf1
Lcat
Gfpt2
Fga
Fgb
Ift74
Phtf2
Fgg
Krt31
Ces1
Mt3
Wbp1l
F
DEPs, vs Yang et al 2022.
Expression (Yang 2022)
Expression
Corr= 0.71
G
Bulk
Yang
-log10(p)

SFig 6

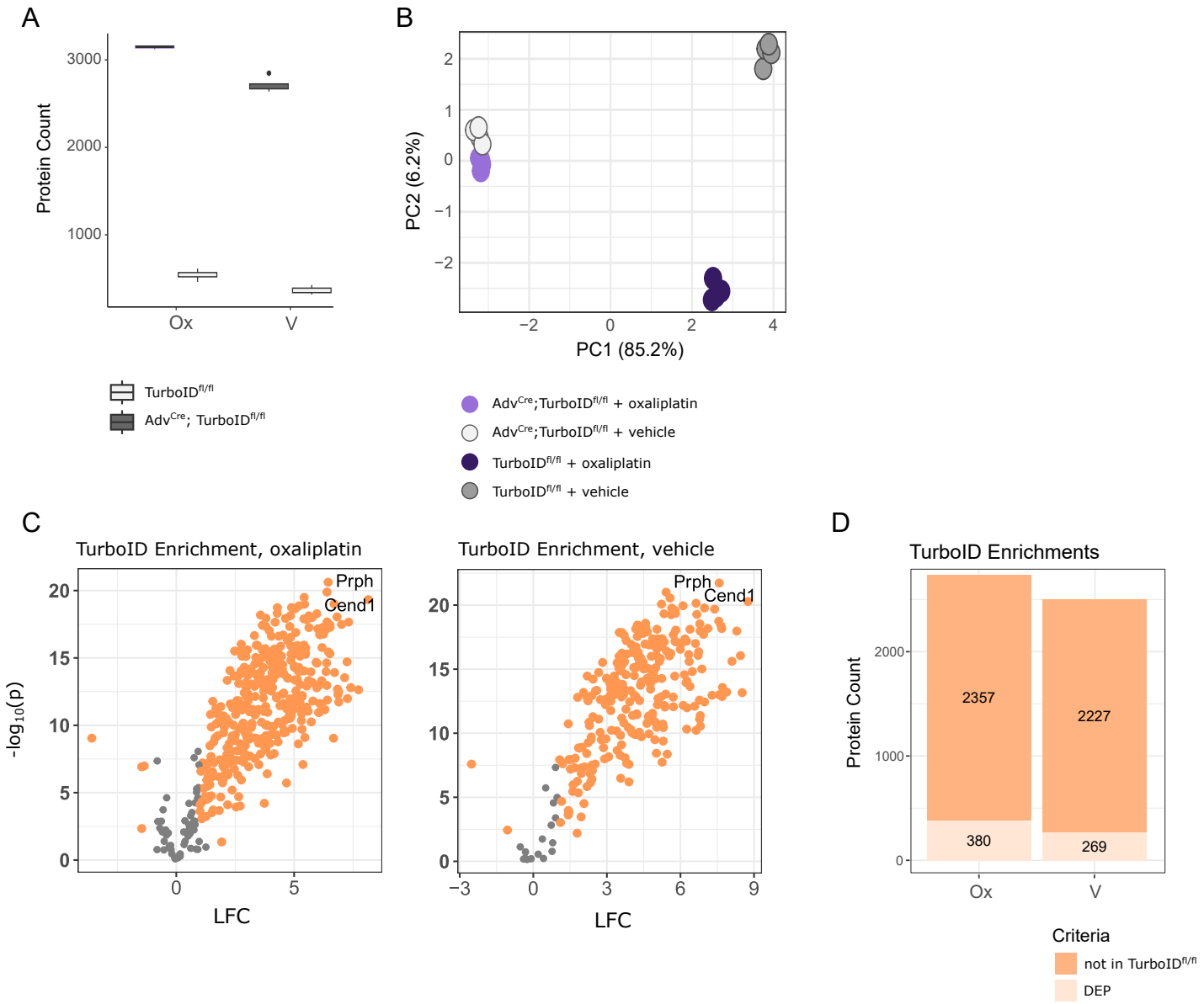
A
Protein Count
3000
2000
1000
Ox
V
TurboID$^{fl/fl}$
Adv^{Cre}; TurboID$^{fl/fl}$
B
PC2 (6.2%)
PC1 (85.2%)
Adv^{Cre};TurboID$^{fl/fl}$ + oxaliplatin
Adv^{Cre};TurboID$^{fl/fl}$ + vehicle
TurboID$^{fl/fl}$ + oxaliplatin
TurboID$^{fl/fl}$ + vehicle
C
TurboID Enrichment, oxaliplatin
TurboID Enrichment, vehicle
Prph
Cend1
-log$_{10}$(p)
LFC
D
TurboID Enrichments
Protein Count
2357
2227
380
269
Criteria
not in TurboID$^{fl/fl}$
DEP

SFig 7

Supplemental Tables + Methods: Proximity labelling reveals the compartmental proteome of murine sensory neurons

Order	*Content*
Supplemental Table 1	expression matrix, TurboID (compartments)
Supplemental Table 2	TurboID protein enrichment
Supplemental Table 3	published comparisons
Supplemental Table 4	sexual dimorphism
Supplemental Table 5	GO compartment functions
Supplemental Table 6	WGCNA functions
Supplemental Table 7	PPI peripheral terminal functions
Supplemental Table 8	PPI central terminal functions
Supplemental Table 9	expression matrix, bulk (tissues)
Supplemental Table 10	TurboID-enriched proteins
Supplemental Table 11	expression matrix, explant (bulk)
Supplemental Table 12	DEPs (bulk oxaliplatin)
Supplemental Table 13	expression matrix, explant (TurboID)
Supplemental Table 14	TurboID protein enrichment, explant
Supplemental Table 15	DEPs (TurboID oxaliplatin)
Supplemental Table 16	GO oxaliplatin treated-explant functions
Supplemental Table 17	Key resources

Supplemental Table 17. Key Resources

Type	Designation	Source	Identifiers	Additional
Mouse strain	C57BL/6J	In house bred		Wild type, male
Mouse strain	Tg(Advillin-Cre)$^{+}$	Kind gift of Prof. Dr. Klaus-Armin Nave, Max Planck Institute for Multidisciplinary Sciences, Göttingen	(Zurborg et al., 2011) Tg(Avil-cre)1Phep MGI:5292346	
Mouse strain	TurboID$^{fl/fl}$	Current study	ROSA26$^{em1(TurboID)Bros}$	
Chemical	Acetonitrile	Fisher Scientific	10001334	
Chemical	Formic Acid	Fisher Scientific	15658430	
Chemical	10x PBS	Fisher Scientific	11594516	
Chemical	Tris 1M	Accugene/Avantor	51237	

Chemical	NaCl, 5M	Accugene/Avantor	51202	
Chemical	Triton™ X-100	Fisher Scientific	10102913	
Chemical	Invitrogen™ SDS, 20% Solution, RNase-free	Fisher Scientific	AM9820	
Chemical	Biotin	Sigma-Aldrich	B4501-10G	
Chemical	Oxaliplatin	Sigma-Aldrich	O9512-5MG	
Chemical	Glycerol	Fisher Scientific	10021083	
Chemical	Dithiothreitol 1M	Sigma-Aldrich	43816	
Chemical	Acetone	Sigma-Aldrich	1000201000	
Chemical	Ethanol	Sigma-Aldrich	1117272500	
Chemical	Iodoacetamide	Sigma-Aldrich	I1149	
Chemical	Ammonium bicarbonate	Sigma-Aldrich	09830-500G	
Chemical	Water MS grade	Sigma-Aldrich	1.15333.1000	
other	Trypsin/Lys-C	Promega	V5073	
other	rhβ-Nerve Growth Factor	R&D Systems	256-GF	
other	Gibco™ DMEM/F-12, GlutaMAX™ Supplement	Fisher Scientific	31331028	
other	Sera-Mag SpeedBead beads	Cytiva	65152105050250, 45152105050250	1:1 mix
other	Sera-Mag SpeedBead Blocked Streptavidin Particles	Cytiva	21152104010150	
other	Complete protease inhibitor cocktail	Roche/ Merck	58929700001	Mix of protease inhibitors
other	Protein LoBind tube	Eppendorf	0030108116, 0030108132	Reagent tube
other	4X Bolt™ LDS sample buffer	Fisher Scientific	B0007	
other	10X Bolt™ Sample Reducing Agent	Fisher Scientific	B0009	
other	Bolt™ Bis-Tris Plus Mini Protein Gels, 4-12%, 1.0 mm	Fisher Scientific	NW04120BOX	
other	Invitrogen™ iBlot™ 2 Transfer Stacks, PVDF, mini	Fisher Scientific	IB24002	

other	SlowFade™ Glass Soft-set Antifade Mountant, with DAPI	Fisher Scientific	S36920	
other	Aurora Series UHPLC column	IonOpticks	AUR2-25075C18A-CSI	
other	Biopsy punch 4mm	Kai medical	48401	
antibody	Streptavidin-AF680	invitrogen	S21378	1:500 dilution
antibody	Mouse mc α-β-actin	Sigma-Aldrich	A1978-200UL	1:500 dilution
antibody	Streptavidin-AF555	Invitrogen	S32355	1:500 dilution
antibody	Rabbit α-NF200	Sigma-Aldrich	N4142-25UL	1:500 dilution
antibody	Chicken α-Peripherin	ABcam	AB39374	1:100 dilution
antibody	Donkey α-mouse AF790	Invitrogen	A11371	1:8000 dilution
antibody	Donkey α-rabbit 488	Invitrogen	A-21206	1:250 dilution
antibody	Donkey α-chicken 647	Invitrogen	A78952	1:250 dilution
software, algorithm	DIA-NN	https://github.com/vdemichev/DiaNN		1.8.2
software, algorithm	R	https://www.r-project.org/		4.3.2
software, algorithm	Mouse proteome	Uniprot	UP000000589	
software, algorithm	Cytoscape	https://cytoscape.org/		3.10.3

Supplemental Methods: Proximity labelling reveals the compartmental proteome of murine sensory neurons

Generation of TurboID mutant mice using CRISPR/Cas9

The conditional TurboID knock-in (cKI) mouse line was generated by site-directed CRISPR/Cas9 mutagenesis in the ROSA26 locus. Superovulated C57Bl6/J females were mated with C57Bl6/J males and fertilized eggs collected. In-house produced CRISPR reagents (hCas9_mRNA, sgRNAs, preformed Cas9_sgRNA-RNP complexes and the homology-directed repair fragment (HDR fragment)) were microinjected into the pronucleus and the cytoplasm of pronuclear-stage zygotes using an Eppendorf Femtojet. Importantly, all nucleotide-based CRISPR/Cas9 reagents (sgRNAs and hCAS9_mRNA) were used as RNA molecules and were not plasmid-encoded, reducing the probability of off-target effects due to the short lifetime of RNA-based reagents (Tycko et al., 2019; Doench et al., 2016). The TurboID-containing HDR fragment was generated by subcloning a V5-tag-TurboID sequence into the Ai14-ROSA26-based plasmid backbone (Madisen et al., 2010) and isolated as a linear DNA fragment by SacI/AgeI restriction enzyme double digestion. Two sgRNAs targeting the ROSA26 Locus were selected using the guide RNA selection tool CRISPOR (Haeussler et al, 2016; Concordet & Haeussler, 2018). The correct locus-specific insertion of the HDR fragment was confirmed by localization PCRs with primers upstream and downstream of the HDR sequence.

Breeding Strategy: The Adv^{Cre};$TurboID^{fl/fl}$ line was regularly maintained on a C57Bl/6 background. For all experiments, Adv^{Cre};$TurboID^{fl/fl}$ males were crossed to $TurboID^{fl/fl}$ females to generate Adv^{Cre};$TurboID^{fl/fl}$ experimental mice (of both sexes) as well as Adv^{Cre} - negative $TurboID^{fl/fl}$ littermate controls ($TurboID^{fl/fl}$, of both sexes). We employed a four-tier strategy to prevent and assess potential germline recombination in line with published recommendations (Luo et al., 2020): (1) All breedings were set up with Adv^{Cre} present in male but not female breeders as suggested another published Adv^{Cre} knock-in mouse line (https://www.jax.org/strain/032536); (2) Adv^{Cre} was always maintained in a heterozygous state; (3) all mice were genotyped; (4) our genotyping protocol included a primer that would detect a potential Cre-recombined allele, which has not been the case in any progeny generated. Thus, to the best of our knowledge, we did not observe germline recombination in Adv^{Cre};$TurboID^{fl/fl}$ mice.

Genotyping Strategy

For TurboID genotyping, genomic DNA (gDNA) was isolated from tail biopsies using a genomic DNA isolation kit (Nexttec, #10.924). For the location PCRs, 20 µL reactions were prepared using 1 µL clean gDNA (15-80ng), 4 µL PrimerSet (4 pmol final each), 4 µL 5X Reaction Buffer (Finnzymes #F-524), 0.4 µL PhireHot-Start II Taq DNA Polymerase (Finnzymes #F-122L), 1 µL 10 mM dNTPs (Bioline #DM-515107), 4 µL Hi-Spec Additive (Bioline #HS-014101) and 5.6 µL H2O. Thermocycler parameters location-PCR Rosa26 left arm: 98°C for 5 min, (98 °C for 45 s, 64 °C for 30 s, 72 °C for 60 s) repeated for 34 cycles, final step at 72 °C for 10 min. Thermocycler parameters-location PCR Rosa26 right arm: 98°C for 5 min, (98 °C for 45 s, 68 °C for 30 s, 72 °C for 180 s) repeated for 34 cycles, final step at 72 °C for 10 min.

For the diagnostic routine genotyping PCR, 20 µL reactions were prepared using 1 µL clean gDNA (15-80ng), 4 µL PrimerSet (4 pmol final each), 4 µL 5X Reaction Buffer (Biozym #331620XL), 0.2 µL Hot-Start Taq DNA Polymerase (Biozym #331620XL), 1 µL 50 mM MgCl2

(AGCTLab stock) and 9.8 µL H2O. Thermocycler parameters: 96°C for 3 min, (94 °C for 30 s, 62 °C for 60 s, 72 °C for 60 s) repeated for 32 cycles, final step at 72 °C for 7 min.

Rosa26 Locus sgRNAs

- Sense Rosa26 protospacer-sgRNA1 sequence: 5‘-ACTCCAGTCTTTCTAGAAGA-3‘ (PAM = TGG)
- Antisense Rosa26 protospacer-sgRNA2 sequence: 5‘-CGCCCATCTTCTAGAAAGAC-3‘ (PAM = TGG)

C57BL6J_Chrom6_Rosa26 target locus (insertion site):

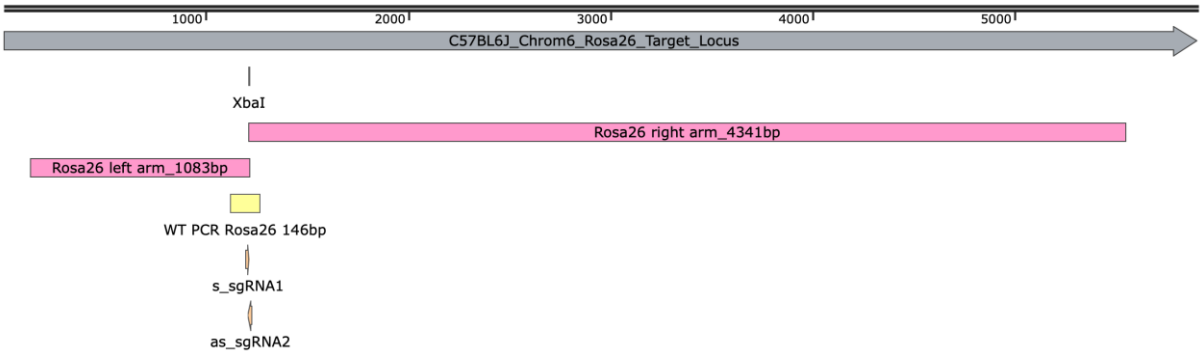

Ai14-TurboID_Rosa26 HDR fragment targeting strategy (conditional knock-in)

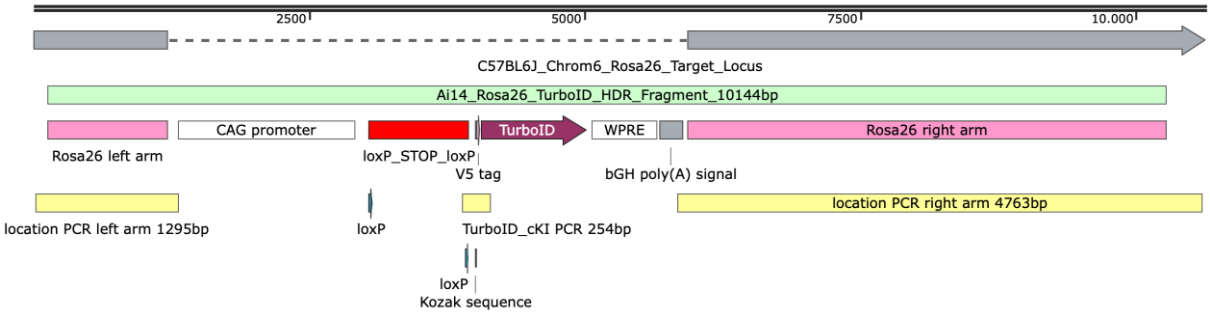

Ai14-TurboID_Rosa26 Cre recombined (knock-in)

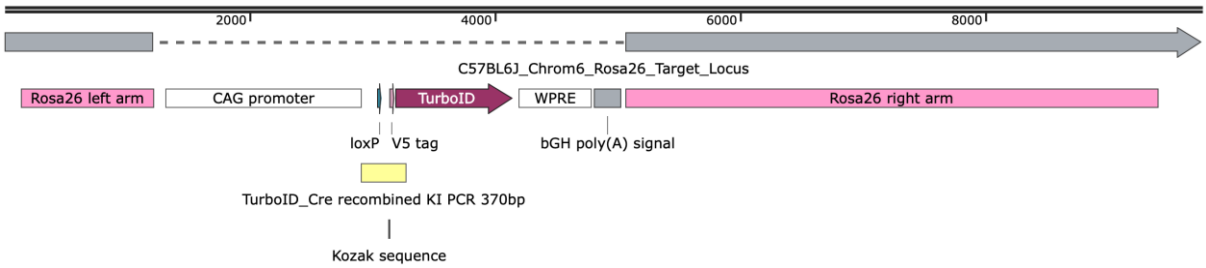

SMethods, Figure1. Schematic representation of the target locus, the targeting strategy (HDR fragment) and the Cre recombination event.

Ai14-TurboID_Rosa26 HDR fragment and sequence annotations:

Lower case letters = upstream and downstream HDR fragment ROSA26 sequences

Capital letters = HDR fragment after locus-specific insertion

Magenta = ROSA26 left- and right arm sequence

Blue = CAG-promoter

Red BOLD = loxP sites

Underlined BOLD = loxP flanked STOP cassette

Green BOLD = ATG Start- and TAA Stop codon

Brown BOLD = V5-tag

Purple BOLD = TurboID

Black BOLD = WPRE

Black underlined = bGH poly(A) signal

86

87 5'-
88 ggaggctgccggggccgcctaaagaagaggctgtgctttggggctccggctcctcagagagcctcggctaggtaggggatcgggactctggcggg
89 agggcggcttggtgcgtttgcggggatgggcggccGCGGCAGGCCCTCCGAGCGTGGTGGAGCCGTTCTGTGAGACAGC
90 CGGGTACGAGTCGTGACGCTGGAAGGGGCAAGCGGGTGGTGGGCAGGAATGCGGTCCGCCCTGCAGCAA
91 CCGGAGGGGGAGGGAGAAGGGAGCGGAAAAGTCTCCACCGGACGCGGCCATGGCTCGGGGGGGGGGG
92 GGCAGCGGAGGAGCGCTTCCGGCCGACGTCTCGTCGCTGATTGGCTTCTTTTCCTCCCGCCGTGTGTGAAA
93 ACACAAATGGCGTGTTTTGGTTGGCGTAAGGCGCCTGTCAGTTAACGGCAGCCGGAGTGCGCAGCCGCCGG
94 CAGCCTCGCTCTGCCCACTGGGTGGGGCGGGAGGTAGGTGGGGTGAGGCGAGCTGGACGTGCGGGCGC
95 GGTCGGCCTCTGGCGGGGCGGGGGAGGGGAGGGAGGGTCAGCGAAAGTAGCTCGCGCGCGAGCGGCC
96 GCCCACCCTCCCCTTCCTCTGGGGGAGTCGTTTTACCCGCCGCCGGCCGGGCCTCGTCGTCTGATTGGCT
97 CTCGGGGCCCAGAAAACTGGCCCTTGCCATTGGCTCGTGTTCGTGCAAGTTGAGTCCATCCGCCGGCCAGC
98 GGGGGCGGCGAGGAGGCGCTCCCAGGTTCCGGCCCTCCCCTCGGCCCCGCGCCGCAGAGTCTGGCCG
99 CGCGCCCCTGCGCAACGTGGCAGGAAGCGCGCGCTGGGGGCGGGGACGGGCAGTAGGGCTGAGCGGC
100 TGCGGGGCGGGTGCAAGCACGTTTCCGACTTGAGTTGCCTCAAGAGGGGCGTGCTGAGCCAGACCTCCATC
101 GCGCACTCCGGGGAGTGGAGGGAAGGAGCGAGGGCTCAGTTGGGCTGTTTTGGAGGCAGGAAGCACTTGC
102 TCTCCCAAAGTCGCTCTGAGTTGTTATCAGTAAGGGAGCTGCAGTGGAGTAGGCGGGGAGAAGGCCGCACC
103 CTTCTCCGGAGGGGGGAGGGGAGTGTTGCAATACCTTTCTGGGAGTTCTCTGCTGCCTCCTGGCTTCTGAGG
104 ACCGCCCTGGGCCTGGGAGAATCCCTTCCCCCTCTTCCCTCGTGATCTGCAACTCCAGTCTTTCTAGCCTTAA
105 TTAACCGTTTAAACAATTCTGCAGGAATCTAGTTATTAATAGTAATCAATTACGGGGTCATTAGTTCATAGCCCATA
106 TATGGAGTTCCGCGTTACATAACTTACGGTAAATGGCCCGCCTGGCTGACCGCCCAACGACCCCCGCCCATT
107 GACGTCAATAATGACGTATGTTCCCATAGTAACGCCAATAGGGACTTTCCATTGACGTCAATGGGTGGAGTATTT
108 ACGGTAAACTGCCCACTTGGCAGTACATCAAGTGTATCATATGCCAAGTACGCCCCCTATTGACGTCAATGAC
109 GGTAAATGGCCCGCCTGGCATTATGCCCAGTACATGACCTTATGGGACTTTCCTACTTGGCAGTACATCTACG
110 TATTAGTCATCGCTATTACCATGGTCGAGGTGAGCCCCACGTTCTGCTTCACTCTCCCCATCTCCCCCCCCTC
111 CCCACCCCCAATTTTGTATTTATTTATTTTTTAATTATTTTGTGCAGCGATGGGGGCGGGGGGGGGGGGGGGC
112 GCGCGCCAGGCGGGGCGGGGCGGGGCGAGGGGCGGGGCGGGGCGAGGCGGAAAGGTGCGGCGGCA
113 GCCAATCARAGCGGCGCGCTCCGAAAGTTTCCTTTTATGGCGAGGCGGCGGCGGCGGCGGCCCTATAAAAA
114 GCGAAGCGCGCGGCGGGCGGGAGTCGCTGCGCGCTGCCTTCGCCCCGTGCCCCGYTCCGCCGCCGCCT
115 CGCGCCGCCCGCCCCGGYTCTGACTGACCGCGTTACTCCCACAGGTGAGCGGGCGGGACGGCCCTTCTC
116 CTCCGGGYTGTAATTAGCGCTTGGTTTAATGACGGYTTGTTTCTTTTCTGTGGYTGCGTGAAAGCCTTGAGGGGC
117 TCCGGGAGGGCCCTTTGTGCGGGGGGAGCGGCTCGGGGGGTGCGTGCGTGTGTGTGTGCGTGGGGAGCG
118 CCGCGTGCGGCTCCGCGCTGCCCGGCGGCTGTGAGCGCTGCGGGCGCGGCGCGGGGCTTTGTGCGCTC
119 CGCAGTGTGCGCGAGGGGAGCGCGGCCGGGGGCGGTGCCCCGCGGTGCGGGGGGGGCTGCGAGGGG
120 AACAAAGGCTGCGTGCGGGGTGTGTGCGTGGGGGGGTGAGCAGGGGGTGTGGGCGCGTCGGTCGGGCTG
121 CAACCCCCCCTGCACCCCCCTCCCCGAGTTGCTGAGCACGGCCCGGCTTCGGGTGCGGGGCTCCGTACG
122 GGGCGTGGCGCGGGGCTCGCCGTGCCGGGCGGGGGGTGGCGGCAGGTGGGGGTGCCGGGCGGGGCG
123 GGGCCGCCTCGGGCCGGGGAGGGCTCGGGGGAGGGGCGCGGCGGCCCCCGGAGCGCCGGCGGCTGT
124 CGAGGCGCGGCGAGCCGCAGCCATTGCCTTTTATGGTAATCGTGCGAGAGGGCGCAGGGACTTCCTTTGTC
125 CCAAATCTGTGCGGAGCCGAAATCTGGGAGGCGCCGCCGCACCCCCTCTAGCGGGCGCGGGGCGAAGC
126 GGTGCGGCGCCGGCAGGAAGGAAATGGGCGGGGAGGGCCTTCGTGCGTCGCCGCGCCGCCGTCCCCTT
127 CTCCCTCTCCAGCCTCGGGGCTGTCCGCGGGGGGACGGCTGCCTTCGGGGGGGACGGGGCAGGGCGGG
128 GTTCGGCTTCTGGCGTGTGACCGGCGGCTCTAGAGCCTCTGCTAACCATGTTCATGCCTTCTTCTTTTTCCTAC
129 AGCTCCTGGGCAACGTGCTGGTTATTGTGCTGTCTCATCATTTTGGCAAAGAATTGATTTGATACCGCGGGCCC
130 TAAGAAGTTCCTATTCTCTAGAAAGTATAGGAACTTCGTCGACATTTAAATCATTTAAAT**ATAACTTCGTATAATGT**
131 **ATGCTATACGAAGTTATTCGCGATGAATAAATGAAAGCTTGCAGATCTGCGACTCTAGAGGATCTGCGACTC**
132 **TAGAGGATCATAATCAGCCATACCACATTTGTAGAGGTTTTACTTGCTTTAAAAAACCTCCCACACCTCCCC**
133 **CTGAACCTGAAACATAAAATGAATGCAATTGTTGTTGTTAACTTGTTTATTGCAGCTTATAATGGTTACAAATA**
134 **AAGCAATAGCATCACAAATTTCACAAATAAAGCATTTTTTTCACTGCATTCTAGTTGTGGTTTGTCCAAACTCA**
135 **TCAATGTATCTTATCATGTCTGGATCTGCGACTCTAGAGGATCATAATCAGCCATACCACATTTGTAGAGGTT**

136 **TTACTTGCTTTAAAAAACCTCCCACACCTCCCCCTGAACCTGAAACATAAAATGAATGCAATTGTTGTTGTTA**
137 **ACTTGTTTATTGCAGCTTATAATGGTTACAAATAAAGCAATAGCATCACAAATTTCACAAATAAAGCATTTTTTT**
138 **CACTGCATTCTAGTTGTGGTTTGTCCAAACTCATCAATGTATCTTATCATGTCTGGATCTGCGACTCTAGAGG**
139 **ATCATAATCAGCCATACCACATTTGTAGAGGTTTTACTTGCTTTAAAAAACCTCCCACACCTCCCCCTGAAC**
140 **CTGAAACATAAAATGAATGCAATTGTTGTTGTTAACTTGTTTATTGCAGCTTATAATGGTTACAAATAAAGCAAT**
141 **AGCATCACAAATTTCACAAATAAAGCATTTTTTTCACTGCATTCTAGTTGTGGTTTGTCCAAACTCATCAATGT**
142 **ATCTTATCATGTCTGGATCCCCATCAAGCTGATCCGGAACCCTTAATATAACTTCGTATAATGTATGCTATAC**
143 **GAAGTTAT**TAGGTCCCTCGACCTGCAGCCCAAGCTAGATCGAATTCGGCCGGCCTTGTACGCGTGCCACC**A**
144 **TGGGCAAGCCCATCCCCAACCCCCTGCTGGGCCTGGACAGCACC**GCTAGC**AAAGACAATACTGTGCCT**
145 **CTGAAGCTGATCGCTCTCCTGGCTAATGGCGAGTTCCATAGTGGCGAACAGCTGGGAGAAACCCTGGGC**
146 **ATGTCCAGGGCCGCTATCAACAAGCACATTCAGACTCTGCGCGACTGGGGCGTGGACGTGTTCACCGTG**
147 **CCCGGAAAGGGCTACTCTCTGCCCGAGCCTATCCCGCTGCTGAACGCTAAACAGATTCTGGGACAGCTG**
148 **GACGGCGGGAGCGTGGCAGTCCTGCCTGTGGTCGACTCCACCAATCAGTACCTGCTGGATCGAATCGGC**
149 **GAGCTGAAGAGTGGGGATGCTTGCATTGCAGAATATCAGCAGGCAGGGAGAGGAAGCAGAGGGAGGAAA**
150 **TGGTTCTCTCCTTTTGGAGCTAACCTGTACCTGAGTATGTTTTGGCGCCTGAAGCGGGGACCAGCAGCAAT**
151 **CGGCCTGGGCCCGGTCATCGGAATTGTCATGGCAGAAGCGCTGCGAAAGCTGGGAGCAGACAAGGTGC**
152 **GAGTCAAATGGCCCAATGACCTGTATCTGCAGGATAGAAAGCTGGCAGGCATCCTGGTGGAGCTGGCCG**
153 **GAATAACAGGCGATGCTGCACAGATCGTCATTGGCGCCGGGATTAACGTGGCTATGAGGCGCGTGGAGG**
154 **AAAGCGTGGTCAATCAGGGCTGGATCACACTGCAGGAAGCAGGGATTAACCTGGACAGGAATACTCTGG**
155 **CCGCTACGCTGATCCGAGAGCTGCGGGCAGCCCTGGAACTGTTCGAGCAGGAAGGCCTGGCTCCATAT**
156 **CTGCCACGGTGGGAGAAGCTGGATAACTTCATCAATAGACCCGTGAAGCTGATCATTGGGGACAAAGAGA**
157 **TTTTCGGGATTAGCCGGGGGATTGATAAACAGGGAGCCCTGCTGCTGGAACAGGACGGAGTTATCAAACC**
158 **CTGGATGGGCGGAGAAATCAGTCTGCGGTCTGCCGAAAAG**TAAACGCGTACAAGGCCGGCCCTGCAGGA
159 ATTCGATATCAAGCTTATCGAT**AATCAACCTCTGGATTACAAAATTTGTGAAAGATTGACTGGTATTCTTAACTA**
160 **TGTTGCTCCTTTTACGCTATGTGGATACGCTGCTTTAATGCCTTTGTATCATGCTATTGCTTCCCGTATGGCTT**
161 **TCATTTTCTCCTCCTTGTATAAATCCTGGTTGCTGTCTCTTTATGAGGAGTTGTGGCCCGTTGTCAGGCAACG**
162 **TGGCGTGGTGTGCACTGTGTTTGCTGACGCAACCCCCACTGGTTGGGGCATTGCCACCACCTGTCAGCTC**
163 **CTTTCCGGGACTTTCGCTTTCCCCCTCCCTATTGCCACGGCGGAACTCATCGCCGCCTGCCTTGCCCGCT**
164 **GCTGGACAGGGGCTCGGCTGTTGGGCACTGACAATTCCGTGGTGTTGTCGGGGAAATCATCGTCCTTTCC**
165 **TTGGCTGCTCGCCTGTGTTGCCACCTGGATTCTGCGCGGGACGTCCTTCTGCTACGTCCCTTCGGCCCTC**
166 **AATCCAGCGGACCTTCCTTCCCGCGGCCTGCTGCCGGCTCTGCGGCCTCTTCCGCGTCTTCGCCTTCGC**
167 **CCTCAGACGAGTCGGATCTCCCTTTGGGCCGCCTCCCCGC**ATCGATACCGTCGACCTCGACCTCGACTGT
168 GCCTTCTAGTTGCCAGCCATCTGTTGTTTGCCCCTCCCCCGTGCCTTCCTTGACCCTGGAAGGTGCCACTCC
169 CACTGTCCTTTCCTAATAAAATGAGGAAATTGCATCGCATTGTCTGAGTAGGTGTCATTCTATTCTGGGGGGTGG
170 GGTGGGGCAGGACAGCAAGGGGGAGGATTGGGAAGACAATGGCAGGCATGCTGGGGAACTAGTGGTGCCA
171 GGGCGTGCCCTTGGGCTCCCCGGCGCGCCGGCTAGAAGATGGGCGGGAGTCTTCTGGGCAGGCTTAAAG
172 GCTAACCTGGTGTGTGGGCGTTGTCCTGCAGGGGAATTGAACAGGTGTAAAATTGGAGGGACAAGACTTCCC
173 ACAGATTTTCGGTTTTGTCGGGAAGTTTTTTAATAGGGGCAAATAAGGAAAATGGGAGGATAGGTAGTCATCTGG
174 GGTTTTATGCAGCAAAACTACAGGTTATTATTGCTTGTGATCCGCCTCGGAGTATTTTCCATCGAGGTAGATTAAA
175 GACATGCTCACCCGAGTTTTATACTCTCCTGCTTGAGATCCTTACTACAGTATGAAATTACAGTGTCGCGAGTTA
176 GACTATGTAAGCAGAATTTTAATCATTTTTAAAGAGCCCAGTACTTCATATCCATTTCTCCCGCTCCTTCTGCAGC
177 CTTATCAAAAGGTATTTTAGAACACTCATTTTAGCCCCATTTTCATTTATTATACTGGCTTATCCAACCCCTAGACA
178 GAGCATTGGCATTTTCCCTTTCCTGATCTTAGAAGTCTGATGACTCATGAAACCAGACAGATTAGTTACATACAC
179 CACAAATCGAGGCTGTAGCTGGGGCCTCAACACTGCAGTTCTTTTATAACTCCTTAGTACACTTTTTGTTGATCC
180 TTTGCCTTGATCCTTAATTTTCAGTGTCTATCACCTCTCCCGTCAGGTGGTGTTCCACATTTGGGCCTATTCTCAG
181 TCCAGGGAGTTTTACAACAATAGATGTATTGAGAATCCAACCTAAAGCTTAACTTTCCACTCCCATGAATGCCTC
182 TCTCCTTTTTCTCCATTTATAAACTGAGCTATTAACCATTAATGGTTTCCAGGTGGATGTCTCCTCCCCCAATATTA
183 CCTGATGTATCTTACATATTGCCAGGCTGATATTTTAAGACATTAAAAGGTATATTTCATTATTGAGCCACATGGTA
184 TTGATTACTGCTTACTAAAATTTTGTCATTGTACACATCTGTAAAAGGTGGTTCCTTTTGGAATGCAAAGTTCAGGT
185 GTTTGTTGTCTTTCCTGACCTAAGGTCTTGTGAGCTTGTATTTTTTCTATTTAAGCAGTGCTTTCTCTTGGACTGGCT

186 TGACTCATGGCATTCTACACGTTATTGCTGGTCTAAATGTGATTTTGCCAAGCTTCTTCAGGACCTATAATTTTGC
187 TTGACTTGTAGCCAAACACAAGTAAAATGATTAAGCAACAAATGTATTTGTGAAGCTTGGTTTTTAGGTTGTTGTGT
188 TGTGTGTGCTTGTGCTCTATAATAATACTATCCAGGGGCTGGAGAGGTGGCTCGGAGTTCAAGAGCACAGACT
189 GCTCTTCCAGAAGTCCTGAGTTCAATTCCCAGCAACCACATGGTGGCTCACAACCATCTGTAATGGGATCTGA
190 TGCCCTCTTCTGGTGTGTCTGAAGACCACAAGTGTATTCACATTAAATAAATAAATCCTCCTTCTTCTTTTTTTT
191 TTTTTTAAAGAGAATACTGTCTCCAGTAGAATTTACTGAAGTAATGAAATACTTTGTGTTTGTTCCAATATGGTAGCC
192 AATAATCAAATTACTCTTTAAGCACTGGAAATGTTACCAAGGAACTAATTTTTATTTGAAGTGTAACTGTGGACAGA
193 GGAGCCATAACTGCAGACTTGTGGGATACAGAAGACCAATGCAGACTTTAATGTCTTTTCTCTTACACTAAGCA
194 ATAAAGAAATAAAAATTGAACTTCTAGTATCCTATTTGTTTAAACTGCTAGCTTTACTTAACTTTTGTGCTTCATCTAT
195 ACAAAGCTGAAAGCTAAGTCTGCAGCCATTACTAAACATGAAAGCAAGTAATGATAATTTTGGATTTCAAAAATGT
196 AGGGCCAGAGTTTAGCCAGCCAGTGGTGGTGCTTGCCTTTATGCCTTTAATCCCAGCACTCTGGAGGCAGAG
197 ACAGGCAGATCTCTGAGTTTGAGCCCAGCCTGGTCTACACATCAAGTTCTATCTAGGATAGCCAGGAATACAC
198 ACAGAAACCCTGTTGGGGAGGGGGGCTCTGAGATTTCATAAAATTATAATTGAAGCATTCCCTAATGAGCCACT
199 ATGGATGTGGCTAAATCCGTCTACCTTTCTGATGAGATTTGGGTATTATTTTTTCTGTCTCTGCTGTTGGTTGGGTC
200 TTTTGACACTGTGGGCTTTCTTTAAAGCCTCCTTCCTGCCATGTGGTCTCTTGTTTGCTACTAACTTCCCATGGCT
201 TAAATGGCATGGCTTTTTGCCTTCTAAGGGCAGCTGCTGAGATTTGCAGCCTGATTTCCAGGGTGGGGTTGGG
202 AAATCTTTCAAACACTAAAATTGTCCTTTAATTTTTTTTTTAAAAAATGGGTTATATAATAAACCTCATAAAATAGTTAT
203 GAGGAGTGAGGTGGACTAATATTAAATGAGTCCCTCCCCTATAAAAGAGCTATTAAGGCTTTTTGTCTTATACTTA
204 ACTTTTTTTTTAAATGTGGTATCTTTAGAACCAAGGGTCTTAGAGTTTTAGTATACAGAAACTGTTGCATCGCTTAAT
205 CAGATTTTCTAGTTTCAAATCCAGAGAATCCAAATTCTTCACAGCCAAAGTCAAATTAAGAATTTCTGACTTTTAAT
206 GTTAATTTGCTTACTGTGAATATAAAAATGATAGCTTTTCCTGAGGCAGGGTCTCACTATGTATCTCTGCCTGATC
207 TGCAACAAGATATGTAGACTAAAGTTCTGCCTGCTTTTGTCTCCTGAATACTAAGGTTAAAATGTAGTAATACTTTT
208 GGAACTTGCAGGTCAGATTCTTTTATAGGGGACACACTAAGGGAGCTTGGGTGATAGTTGGTAAAATGTGTTTCA
209 AGTGATGAAAACTTGAATTATTATCACCGCAACCTACTTTTTAAAAAAAAAAGCCAGGCCTGTTAGAGCATGCTTA
210 AGGGATCCCTAGGACTTGCTGAGCACACAAGAGTAGTTACTTGGCAGGCTCCTGGTGAGAGCATATTTCAAAA
211 AACAAGGCAGACAACCAAGAAACTACAGTTAAGGTTACCTGTCTTTAAACCATCTGCATATACACAGGGATATT
212 AAAATATTCCAAATAATATTTCATTCAAGTTTTCCCCCATCAAATTGGGACATGGATTTCTCCGGTGAATAGGCAG
213 AGTTGGAAACTAAACAAATGTTGGTTTTGTGATTTGTGAAATTGTTTTCAAGTGATAGTTAAAGCCCATGAGATACA
214 GAACAAAGCTGCTATTTCGAGGTCTCTTGGTTTATACTCAGAAGCACTTCTTTGGGTTTCCCTGCACTATCCTGA
215 TCATGTGCTAGGCCTACCTTAGGCTGATTGTTGTTCAAATAAACTTAAGTTTCCTGTCAGGTGATGTCATATGATTT
216 CATATATCAAGGCAAAACATGTTATATATGTTAAACATTTGTACTTAATGTGAAAGTTAGGTCTTTGTGGGTTTGATT
217 TTTAATTTTCAAAACCTGAGCTAAATAAGTCATTTTTACATGTCTTACATTTGGTGGAATTGTATAATTGTGGTTTGCA
218 GGCAAGACTCTCTGACCTAGTAACCCTACCTATAGAGCACTTTGCTGGGTCACAAGTCTAGGAGTCAAGCATT
219 TCACCTTGAAGTTGAGACGTTTTGTTAGTGTATACTAGTTTATATGTTGGAGGACATGTTTATCCAGAAGATATTCA
220 GGACTATTTTTGACTGGGCTAAGGAATTGATTCTGATTAGCACTGTTAGTGAGCATTGAGTGGCCTTTAGGCTTG
221 AATTGGAGTCACTTGTATATCTCAAATAATGCTGGCCTTTTTTAAAAAGCCCTTGTTCTTTATCACCCTGTTTTCTA
222 CATAATTTTTGTTCAAAGAAATACTTGTTTGGATCTCCTTTTGACAACAATAGCATGTTTTCAAGCCATATTTTTTTTC
223 CTTTTTTTTTTTTTTTTTGGTTTTTCGAGACAGGGTTTCTCTGTATAGCCCTGGCTGTCCTGGAACTCACTTTGTAGA
224 CCAGGCTGGCCTCGAACTCAGAAATCCGCCTGCCTCTGCCTCCTGAGTGCCGGGATTAAAGGCGTGCACCA
225 CCACGCCTGGCTAAGTTGGATATTTTGTTATATAACTATAACCAATACTAACTCCACTGGGTGGATTTTTAATTCA
226 GTCAGTAGTCTTAAGTGGTCTTTATTGGCCCTTCATTAAAATCTACTGTTCACTCTAACAGAGGCTGTTGGTACTA
227 GTGGCACTTAAGCAACTTCCTACGGATATACTAGCAGATTAAGGGTCAGGGATAGAAACTAGTCTAGCGTTTTG
228 TATACCTACCAGCTTTATACTACCTTGTTCTGATAGAAATATTTCAGGACATCTAGagtgtactataaggttgatggtaagctt
229 ataaggaacttgaaagtggagtaactactccatttctctgaggggagaattaaaatttttgaccaagtgttgttgagccactgagaatggtctcagaa
230 cataacttcttaaggaaccttcccagattgccctcaacactgcaccacatttggtcctgcttgaacattgccatggctcttaaagtcttaattaagaa
231 tattaattgtgtaattattgtttttcctcctttagatcattccttgaggacaggacagtgcttgtttaaggctatatttctgctgtctgagcagcaacaggtc
232 ttcgagatcaacatgatgttcat-3’

233

234 **SMethods, Sequence.** Ai14-TurboID_Rosa26 HDR fragment and sequence annotations.

SMethods, Table. Primer sequence and fragment size information

Name	ID	Sequence (5' → 3')	mer	Orientation	Target Region	Fragment Size
Rosa26 Left Arm	29194	CGCCTAAAGAAGAGGCTGTG	20	Sense	Upstream ROSA26 left-arm	1295 bp
	7604	CGCGGAACTCCATATATGGGCT	22	Anti-sense	5'-End-CAG-promoter	
Rosa26 Right Arm	2736	GCAGGACAGCAAGGGGGAGGAT	22	Sense	bGH poly(A) signal	4736 bp
	36502	GACCTGTTGCTGCTCAGACAGC	22	Anti-sense	Downstream Rosa26 right arm	
Diagnostic Routine Genotyping PCR	14025	CTCTGCTGCCTCCTGGCTTCT	21	Sense	ROSA26 upstream insertion site	146 bp
	24229	CGCCCACACACCAGGTTAG	19	Anti-sense	ROSA26 downstream insertion site	
	30545	AAGCTGATCCGGAACCCTTAA	21	Sense	Upstream loxP2	254 bp (WT) 370 bp (Cre)
	26512	CTACAGCTCCTGGGCAACG	19	Sense	upstream loxP1 (3'-End CAG promoter)	
	38281	CCAGGGTTTCTCCCAGCTGT	20	Anti-sense	TurboID	